ANALYTIC 3D SCATTER CORRECTION IN PET USING THE KLEIN-NISHINA EQUATION

ANALYTIC 3D SCATTER CORRECTION IN POSITRON TOMOGRAPHY USING THE KLEIN-NISHINA EQUATION

by:

CHRISTOPHER VAN BOWEN, B.Sc.

A Thesis
Submitted to the School of Graduate Studies
in Partial Fulfilment of the Requirements
for the Degree
Master of Science

McMaster University

MASTER OF SCIENCE (1994)　　McMASTER UNIVERSITY
(Physics)　　Hamilton, Ontario

TITLE: Analytic 3D Scatter Correction in Positron Tomography Using the Klein-Nishina Equation

AUTHOR: Christopher Van Bowen, B.Sc. (Saint Francis Xavier University)

SUPERVISOR: Dr. C. Nahmias

NUMBER OF PAGES: x, 139

ABSTRACT

In order to perform quantitative 3D positron tomography, it is essential that an accurate means of correcting for the effects of Compton scattered photons be developed. The two main approaches to compensate for scattered radiation rely on energy considerations or on filtering operations. Energy based scatter correction methods exploit the reduced energy of scattered photons to differentiate them from unscattered photons. Filtered scatter correction methods require the measurement of scatter point spread functions to be used for convolution with the acquired emission data set. Neither approach has demonstrated sufficient accuracy to be applied in a clinical environment.

In this thesis, I have developed the theoretical framework for generating the scatter point spread functions for the general case of any source position within any non-uniform attenuation object. This calculation is based on a first principles approach using the Klein-Nishina differential cross section for Compton scattering to describe the angular distribution of scatter annihilation photons. The attenuation correction factors from transmission scans are included within the theory as inputs describing the distribution of matter in the object being imaged.

The theory has been tested by comparison with experimental scatter profiles of point sources which are either centered, or off-center in water-filled cylinders. Monte Carlo simulations have been used to identify the detector energy threshold where the single scatter assumption employed by the theory is most satisfied. The validity of a mean scatter position assumption, used in the development of the theory, is tested using analytic calculations of a non-uniform attenuation phantom. The physical effects most responsible for determining the shape of the scatter profiles, as well as the assumptions employed by several common scatter correction methods, are revealed using the analytic scatter correction theory.

ACKNOWLEDGEMENTS

I would like to extend my greatest appreciation to my supervisor, Dr. Claude Nahmias, for the insight he contributed to this project and for the attention he directed towards the preparation of the text. In particular, his virtue of patience will not be forgotten. The *Geant* Monte Carlo code, provided by Dr. Christian Michel, was instrumental to this thesis and is also greatly appreciated.

I'm very thankful for the assistance of all my fellow inhabitants of the Mind lab. Particular thanks is extended to Rob deKemp and Ben Yu for their numerous discussions regarding the project and for their nocturnal discussions regarding everything else. The technical assistance provided by Bev Kenyon, Anita Sheiffel and Joe Thomas was greatly appreciated for its speeding the progress of this thesis and slowing the recession of my hairline. I would like to extend thanks to Vanessa Cheng for her help in proof-reading portions of the text and my apologies to Antonella Scarponi for my monopolization of her computer (or attempts to).

I'm most thankful for the support and encouragement provided by my girlfriend, Sandra, over the course of preparing this thesis. In particular, her virtue of patience will not be forgotten.

To the owners and the players association of the NHL and MLB, I would like to extend my most sincere gratitude. Without your efforts to institute a strike/lockout situation this thesis might never have been completed. Finally, I would like to thank the Fragile Porcelain Mice, the Soft Angora Sweater Wearing Debutantes, the Screaming Bunny Slippers and the Headless Chickens as well as the gang at Fat Tuesdays and the players of Club Mac for making the past two years an experience I will never forget.

TABLE OF CONTENTS

INTRODUCTION

CONCLUSIONS

LIST OF TABLES

LIST OF ILLUSTRATIONS

INTRODUCTION

Positron Tomography

The measurement of metabolic processes in vivo is accomplished in positron tomography by labelling trace amounts of biologically active molecules with positron emitting isotopes before administering them to the body. Compounds are labelled by attaching positron isotopes generated in a particle accelerating cyclotron to biological compounds of interest. Some of the important metabolic measurements in the body include brain blood perfusion as well as glucose and dopamine utilization.

By measuring the regional distribution of cerebral blood flow using ^{15}O labelled water, activation studies, which quantify differences in the distribution of brain blood perfusion, may be undertaken to locate regions of the brain responsible for specific mental or physical tasks. Fluoro-deoxy-glucose (FDG), ^{18}F labelled deoxy-glucose, is administered to measure regional cerebral metabolic rate and is useful for diagnosing diseases such as Huntington's Chorea. Studies involving the injection of fluoro-L-dopa, ^{18}F labelled L-dopa, can reveal the presence of Parkinson's disease. The diagnosis of other conditions including Alzheimer's disease and schizophrenia can also be investigated using PET techniques. Accurate quantitative measurements of regional distributions are essential to perform such disease diagnosis.

Quantitative Accuracy

Images of radiopharmaceutical distribution are formed by reconstruction of projection data, typically through filtered backprojection techniques. Image resolution for modern positron tomography systems employing Bismuth Germanate (BGO) block detectors is approximately 5 mm in the axial and transaxial directions. The main factor determining spatial resolution is the size of the crystal detectors (6.22 mm x 6.75 mm). The positron's range before annihilation and the slight non-collinearity of the two annihilation photons have a lesser impact on spatial resolution.

Quantitative accuracy is also diminished when Compton scattering of one or both of the annihilation photons occurs within the patient. Deviation of either photon from the collinear path either causes a different detector to be struck than had the photon remained unscattered or perhaps even causes the photon to be scattered completely out of the detector array. Compton scattering of either photon in the patient to a direction outside of the detector array produces a loss of detected annihilation events with the greatest effect being in the center of the patient. Attenuation correction must be performed to correct for such events lost to Compton scattering, as well as those lost to photoelectric absorption, thus restoring count rates in the interior of objects. Scatter correction is required to remove those counts involving a scattered photon striking a different detector than had the photon remained unscattered. Such unwanted counts which contribute false position information must be removed prior to attenuation correction.

At present, no scatter correction technique of sufficient accuracy has been developed to remove scattered from unscattered coincidences. In the past, the problem of Compton scattered events has been minimized by placing collimating interplane tungsten septa between each of the detector rings. The septa, though, do not affect those events caused by photons which scatter and remain within the same tomographic plane. The interplane septa limit the fraction of data contaminated by scatter to below 15%. Recent interest in performing 3D acquisitions, which allow coincident events to be recorded between detectors of any ring, has necessitated the removal of the septa thus resulting in scatter fractions greater than 40%. The benefits of increased count rate desired for 3D acquisitions cannot be realized until an accurate means of removing the large component of scatter can be developed.

Project Scope

Removal of the scatter counts from 3D acquisitions in septa-free positron tomographs is required before the benefits of newly developed 3D reconstruction algorithms can be realized. One approach to solving this problem involves the functional characterization of point source profiles in a variety of positions within different non-uniform attenuation objects. A method of scatter estimation called convolution subtraction may then be implemented if the scatter point spread functions (PSF's) for the object being scanned could be deduced. In the past, much effort has been expended upon measurements of PSF's for various locations within water cylinders in the hope that such functions would be comparable to those encountered in realistic imaging situations involving non-uniform attenuation conditions of the body. In this work, the theoretical framework for estimating scatter point spread functions under non-uniform attenuation conditions is developed using the Klein-Nishina (K-N) differential cross section as well as the attenuation correction factors from a transmission scan. The K-N equation evaluates scatter angle distributions while the attenuation correction factors act as input describing the attenuating media within the object. The theory is tested for some simple cylindrical water filled phantoms. The physics responsible for determining the shape of scatter profiles is also discussed.

CHAPTER I

Principles of Positron Tomography

Positron tomography relies on the fact that many chemical substances in the human body can be labelled with positron emitting radioisotopes to trace their path so that studies of chemical reactions can be made. To understand how radiopharmaceuticals are traced and displayed as images, the physics of positron annihilation with atomic electrons and the subsequent production and tracking of 511 keV photons must be described. To record the annihilation photons, a detector array of Bismuth Germanate (BGO) block detectors is used complete with coincidence electronics to record the pair of 511 keV photons originating from the same annihilation event. The organization of the data into projections stored in sinogram matrices is described along with the technique usually employed to reconstruct the projection data into images. The data correction techniques required to account for detector function, coincidence processing and annihilation photon scatter are finally described so that the principles of positron tomography may be understood.

Physics Processes of PET

The detection of photons originating from positron annihilation with atomic electrons is essential to positron tomography. The production of two 511 keV photons travelling in opposite directions is revealed through an examination of the physics processes involved in positron annihilation. The possible interactions of 511 keV photons are then described so that their detection by BGO detectors may be understood and the corrections required for attenuation and scatter may become clear.

Positron Emission and Annihilation

Nuclei that are rich in protons or deficient in neutrons may become stable either through positron emission or electron capture. In positron emission, a proton is converted to a neutron by ejecting a positive electron through the nuclear reaction:

$$ {}^{A}_{Z}X \rightarrow {}^{A}_{Z-1}Y + \beta^{+} + \nu \qquad (1.1)$$

where in addition to the positron, a neutrino is ejected (Sorenson and Phelps, 1980). The minimum transition energy required for positron emission is 1.022 MeV ($2m_ec^2$) to account for the atom's loss of a positron as well as an orbital electron, ejected to preserve charge neutrality. Any excess energy of reaction becomes shared kinetic energy between the positron (β^+) and the neutrino (ν). The ratio of kinetic energy shared by each particle is different for each reaction so that the distribution of positron kinetic energies is a continuous beta spectrum with a maximum endpoint energy of:

$$E_{\beta^+} = [M(x) - M(y) - 2m_e]\,c^2 \tag{1.2}$$

The competing process for stabilizing proton rich nuclei is electron capture when an orbital electron is "captured" by the nucleus and combines with a proton to form a neutron according to the equation:

$$p^+ + e^- \rightarrow n + \overline{\nu} \tag{1.3}$$

The electrons closest to the nucleus, in the K shell, have the greatest chance of capture as their wavefunctions exhibit the greatest overlap with the nucleus. Electron capture is more prevalent for heavy nuclei whose large nuclear charge draws the inner electrons closer to the nucleus. This effect can be seen in table 1 (deKemp, 1992) since the proportion of positron decay diminishes for heavier isotopes such as ^{64}Cu through increased incidence of electron capture. It is evident that positron emission is the predominant process for the most frequently used PET radioisotopes.

TABLE 1

PROPERTIES OF COMMON POSITRON EMITTING ISOTOPES

Isotopes	Percent β^+ Decay	Half-Life	Max Energy [MeV]	Mean Energy [MeV]	Mean Range [mm]
^{11}C	99.8	20.3 min	0.97	0.394	1.24
^{13}N	100	10.0 min	1.2	0.488	1.67
^{15}O	100	124 sec	1.74	0.721	2.62
^{18}F	97	109 min	0.635	0.250	0.623
^{64}Cu	19	12.8 hrs	0.656	0.258	0.656

The fast positrons emitted in positron decay slow to thermal energies predominantly through three processes: ionization, excitation and bremsstrahlung radiation. Most of the energy loss is due to the collisional losses of ionization, where electrons are scattered out of atoms, and excitation, where atomic electrons are excited to higher energy levels. The specific energy loss due to electron collisions is described by the Bethe equation (Knoll, 1989). Positrons may undergo radiative losses when passing near atomic nuclei since accelerated charges emit electromagnetic radiation according to classical theory. The amount of energy lost to this bremsstrahlung radiation is a small fraction of the energy lost to collisional processes as the ratio is approximately:

$$\frac{(dE/dx)_r}{(dE/dx)_c} \approx \frac{EZ}{700} \qquad \textbf{(1.4)}$$

where E is in MeV (Knoll, 1989).

When the positron energy has been reduced to below the ionization energy of the atoms of the surrounding material, the ore gap region is entered. In the ore gap, any inelastic collisions are likely to form positronium where a positron and electron orbit each other (Stewart and Roellig, 1967). If positronium is not formed, the positrons will undergo elastic collisions with atomic electrons until thermalized. At thermal energies below 10eV, annihilation of the positron with an atomic electron becomes highly probable and two 511 keV photons will be released at nearly 180° from each other. Conservation of energy dictates that the photons have a total energy of $2m_ec^2 = 2 \times 511$ keV, while conservation of momentum forces the photons to have opposing direction. The residual kinetic energy possessed by the positron while annihilating causes the photons energy to deviate slightly from 511 keV and the angle between photons to have a deviation of 0.4° from the mean of 180° (Stewart and Roellig, 1967).

When entering the ore gap, positrons form positronium 36% of the time in water (Ache, 1979). Positronium may form either triplet ortho-positronium, with parallel spins, or singlet para-positronium, with anti-parallel spins, typically in a 3:1 ratio. Para-positronium undergoes two photon self annihilation very quickly ($\tau=1.25\text{x}10^{-10}$s), while ortho-positronium undergoes three photon annihilation much more slowly ($\tau=1.4\text{x}10^{-7}$s) (Stewart and Roellig, 1967). More often the ortho-positronium will either suffer pickoff annihilation by two photon annihilating with an electron from another atom ($\tau=1.8\text{x}10^{-9}$s), or be converted to para-positronium after colliding and exchanging electrons with a surrounding atom. The end result is that 2 photon annihilation is the most likely product of a positron's existence after travelling a short distance or range from the initial emission position (Table 1).

Before thermalizing and annihilating, the positrons undergo many elastic and inelastic collisions changing their direction so that the actual range travelled by a positron is much less than the path length followed. Since positrons lose most of their energy in inelastic collisions with atomic electrons, the positron range is proportional to the medium's electron density:

$$Range \;\alpha\; \rho N_A (Z/A) \tag{1.5}$$

where N_A is Avogadro's constant and ρ is the medium density (Knoll, 1989). Since Z/A is nearly constant for all elements, the range is roughly proportional to the medium's density and the positron range in different materials can be estimated from the measured range in water, as well as from the particular specific gravity of the material involved.

Gamma Ray Interactions

The main result of positron annihilation is to produce two 511 keV photons travelling in opposite directions. Gamma rays may undergo three types of interactions with matter: absorption; scattering or pair production, with the dominant process being determined by both the energy of the photon, as well as the material in which interactions may occur.

Pair production occurs when a photon is converted to a positron and electron after striking either a nucleus or an electron. The spectator nucleus or electron is required for conservation of momentum and energy. Pair production is energetically impossible for the 511 keV annihilation photons since a reaction energy threshold of 1.022 MeV is required to produce the two particles of electron mass ($2m_ec^2 = 1.022$ MeV).

Gamma rays may be absorbed by the photoelectric effect when the incident photon strikes an atomic electron causing it to be ejected with a kinetic energy equal to the photon energy less the electron's binding energy. The threshold energy of photoelectric absorption is merely the binding energy of the electron interacting with the photon ($E <$ 100 keV) so that the 511 keV photons are well above threshold (Lederer et al, 1968). K shell electrons are the most likely candidates for the photoelectric effect, with greater than 80% of ionized electrons coming from this shell. Characteristic x-rays or Auger electrons are emitted after the photoelectric effect occurs as the excited atom de-excites.

From a quantum mechanical calculation that assumes no nuclear screening and non-relativistic energies (Bransden and Joachain, 1983), the cross-section for the photoelectric effect is estimated to be:

$$\sigma_{PE} = \frac{16\sqrt{2}\pi}{3}\alpha^8 Z^5 [\frac{mc^2}{E_\gamma}]^{7/2} a_o^2 \tag{1.6}$$

where a_o = 52.9 pM is the first Bohr radius of hydrogen, Z is the target molecule's nuclear charge and $\alpha \approx 1/137$ is the fine structure constant. The cross-section increases rapidly by Z^5 as the nuclear charge of the interacting medium increases, while also decreasing quite rapidly by $E_\gamma^{-3.5}$ as the incident photon energy increases.

Unlike the photoelectric effect, which completely absorbs the incident photon dissipating its energy by releasing a high energy short range electron, the scattering process produces an equal or lower energy photon which may propagate a great distance after scattering through some angle. The dominant scattering process for 511 keV photons is Compton scattering, where the incident gamma ray strikes an atomic electron producing atomic ionization. The incident photon will scatter through an angle β determined by the Klein-Nishina differential cross section equation:

$$\frac{d\sigma_c}{d\Omega} = Zr_o^2 (\frac{1}{1+\alpha(1-\cos\beta)})^2 (\frac{1+\cos^2\beta}{2}) (1+\frac{\alpha^2(1-\cos\beta)^2}{(1+\cos^2\beta)[1+\alpha(1-\cos\beta)]}) \tag{1.7}$$

where r_o = 2.818 fM is the classical electron radius, Z is the nuclear charge of the target molecule and $\alpha = E_\gamma/m_ec^2$ (Knoll, 1989). The energy of the resulting scattered photon (E_γ') is determined by the scattering angle and incident photon energy (E_γ) according to the equation:

$$E'_\gamma = \frac{E_\gamma}{1 + E_\gamma / m_e c^2 (1 - \cos\beta)} \tag{1.8}$$

For 511 keV annihilation photons, $\alpha = 1$ and the K-N equation and scattered photon energy reduce to:

$$\frac{d\sigma_c}{d\Omega} = \frac{Z r_o^2}{2} \left(\frac{3 - 3\cos\beta + 3\cos^2\beta - \cos^3\beta}{(2 - \cos\beta)^3} \right)$$

$$E'_\gamma = \frac{E_\gamma}{2 - \cos\beta} \tag{1.9}$$

Compton scattered photons become more forward scattered as the incident energy increases exhibiting some forward scattering for 511 keV photons (Knoll, 1989). The angular distribution of the scattered photons is material independent being a function of energy alone as the Z of the material serves only to indicate the probability of scatter through any angle. The Compton cross-section increases linearly with Z, unlike the photoelectric cross-section which increases as Z^5, causing Compton scattering to be the most likely process for low Z materials.

Rayleigh scattering occurs when a gamma ray strikes an atomic electron briefly exciting it to a higher energy level before de-exciting back to the initial energy level. A photon of the same energy as the incident photon is released through some angle in this process. Rayleigh scattering occurs with a very low probability relative to Compton scattering for 511 keV photons.

Image Formation

In order to produce images of the positron isotope distribution, the collinear 511 keV annihilation photons must be detected efficiently. Images may then be reconstructed since the coincident detection of two 511 keV photons travelling in opposing directions will produce a line of response (LOR) between the two detectors along which the positron annihilation event must have occurred (fig 1). The array of BGO detectors, the processing of the output pulses from the photomultiplier tubes (PMT's), the organization of line of response data into projections and the image reconstruction from projection data are described below to explain image formation for PET.

Detection of Gamma Rays

To obtain line of response data indicating the line along which the positron annihilation event occurred, the positions, energies and times of arrival of the two annihilation photons must be recorded. In the ECAT-953 scanner, photons are detected using two adjacent 76 cm diameter rings of bismuth germanate detectors ($Bi_4Ge_3O_{12}$). Each ring of BGO detectors consists of 48 blocks of bismuth germanate, each 5.0 cm x 5.4 cm across and 3 cm deep (fig 2a). The BGO block detectors are partially sliced with variable depth grooves to produce an 8x8 matrix of crystal elements each 6.22 mm x 6.75 mm across (fig 2b). Four photomultiplier tubes arranged in a square formation are coupled to the back of each BGO block to collect the 505 nm scintillation photons

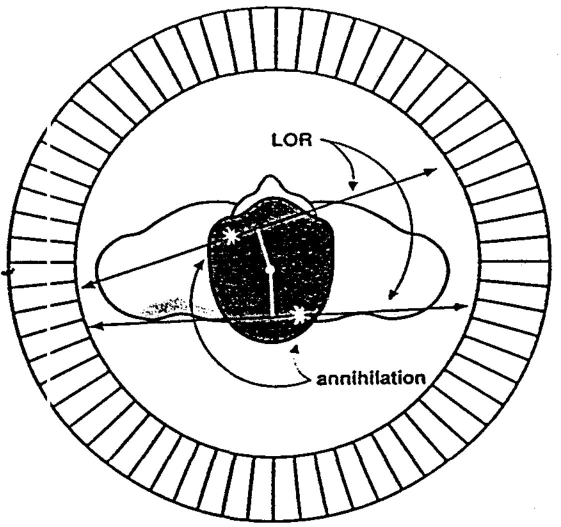

Figure 1: Positron annihilation event creating 2 photons which define a line of response.

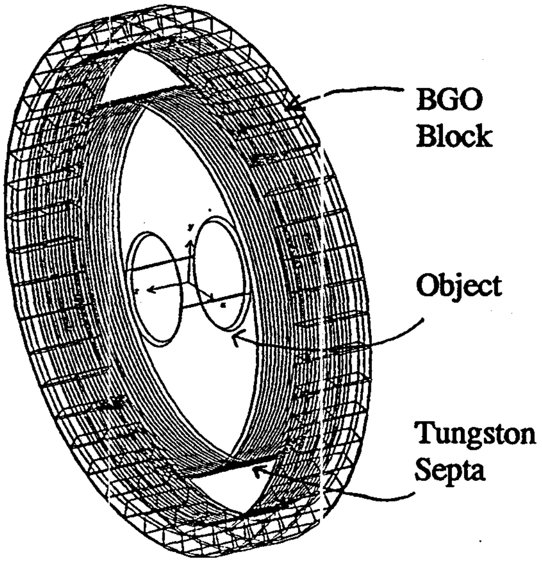

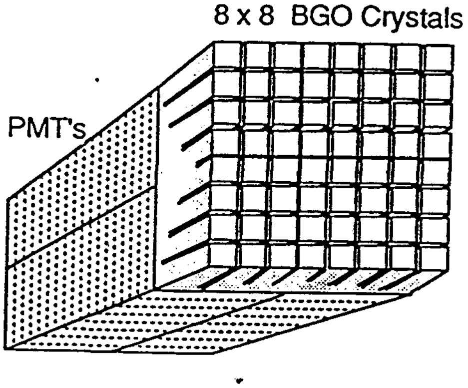

Figure 2(a): Detector array with 2 rings of 48 BGO blocks each.

Figure 2(b): A BGO block sliced into an 8 x 8 grid of crystal detectors with 4 PMT's coupled to each block.

produced when the gamma rays deposit energy in the crystal through photoelectric or Compton interactions. Since BGO exhibits a linear response in that the number of scintillation photons produced is proportional to the energy deposited in the crystal, the summed output signal from the four PMT's will be a measure of the total energy deposited in the crystal. The particular crystal element which absorbed the photon energy can be determined from the relative pulse height for each of the four PMT's since the variable depth grooves sliced into the BGO blocks act as light pipes producing a characteristic light pattern, and hence a different PMT output signal ratio for each of the 64 crystal elements.

BGO crystal detectors are the scintillator material of choice for performing positron tomography because the relatively high energy 511 keV annihilation photons require a high Z material to maximize photoelectric absorption and hence, detector efficiency. The bismuth ($Z=83$) in BGO is largely responsible for causing BGO to have the largest probability per unit volume for gamma ray photoelectric absorption of any commonly available scintillation material. Although most 511 keV photons will still undergo more than one interaction before absorption (56% in BGO based on Compton to total interaction cross sections), this is still a significant improvement over BGO's main alternative scintillator, thallium doped sodium iodide [NaI(Tl)], which experiences multiple interactions 82% of the time (Thompson, 1993).

The main difficulties created by Compton scattering within the BGO block detectors is to diminish the accuracy of gamma position determination and to record inaccurately the gamma ray energy. The Compton interaction could result in energy being deposited in two distant portions of the BGO block, interfering with the selection of the crystal element where the gamma initially interacted. Energy deposition is very localized for the photoelectric effect due to the short range of the energetic electron, unlike the much longer range exhibited by a Compton scattered photon. If this Compton scattered photon were to escape the BGO block entirely before experiencing a terminating photoelectric interaction, the photon's energy deposition would be incomplete and the summed output from the 4 PMT's would indicate a lower energy than possessed by the incident photon.

BGO is superior to NaI(Tl) for its photoelectric effect interaction fraction as well as for its higher stopping power improving detector efficiency, however BGO does suffer some deficiencies. The conversion efficiency of BGO is only about 20% that of NaI(Tl), resulting in fewer scintillation photons being produced for the same photon energy deposited (Knoll, 1989). The conversion efficiency is the major determinant of the detector's energy resolution since the number of photons produced follows Poisson statistics, introducing a statistical variation in the recorded energy. Energy resolution is defined as:

$$R = \frac{FWHM}{H_o} \tag{1.10}$$

where H_o is the mean pulse height for a given photon energy and FWHM is the observed FWHM of the pulse height distribution. The energy resolution for BGO is approximately 25% while that of NaI(Tl) is better than 10%.

Coincidence Counting

Since the result of positron annihilation is two 511 keV photons moving in opposite directions, PET collects its line of response data by measuring those annihilation photons arriving at two detectors within some timing coincidence window. To determine the coincidently detected annihilation photons, the time of arrival of each photon must be deduced from the pulse signal output from the PMT's. The time of arrival is determined by when the pulse rises above a threshold voltage called a trigger. Timing information is most accurately determined by systems with large amplitude, low noise signals having a fast and consistent rise time. Noisy signals create a statistical uncertainty in the timing estimate called time jitter. If the signal amplitude varies for the same shape pulse, as may happen for different amounts of energy deposited in the BGO crystal, amplitude walk occurs and a shift to early triggering results for larger pulses. Inconsistent rise times for same amplitude signals may cause shifts to early triggering for fast rising pulses, creating rise time walk.

Amplitude walk, rise time walk and time jitter have noticeable effects on a coincident detection system. These effects can be observed when 2 photons simultaneously strike separate detectors, as happens when a positron emitter is placed equidistant between the two detectors. Instead of the time difference between each detected photon being a delta function at t=0, a distribution of time differences about t=0 is observed where the FWHM of this function is defined as the timing resolution (τ) of the detection system. The timing resolution of scintillator - PMT systems is largely determined by the properties of the scintillator being used. For instance, BGO has a slower rise time and a poorer light yield than NaI(Tl) so that its smaller amplitude, inconsistently rising pulses produce a timing resolution approximately twice as bad as that of NaI(Tl) (Knoll, 1989).

Coincident events in the ECAT-953 are recorded when a second photon strikes one of the 5 opposing buckets (160 crystal detectors) directly across the field of view from a crystal detector initially struck by a photon with a time difference less than some timing coincident window, τ_c (fig 3). The two factors largely responsible for determining the selection of τ_c are the timing resolution of the detectors (τ) and the expected time of arrival difference for two photons emitted from a positron at the extreme edge of the field of view. The maximum possible time of arrival difference for annihilation photons of the 76 cm diameter ECAT-953 is 2.5 ns, taking into consideration the speed of light. A coincident window of 12 ns is used by the ECAT-953, considering both timing resolution and time of flight effects.

Although τ_c must be large enough to accept all true coincidences resulting from positron annihilation photon detection, τ_c must be kept as small as possible to avoid the effect of multiple coincidences where more than two photons strike detectors within τ_c. This occurs when having more than one positron decay within τ_c obtains significant probability. Multiple coincidences do not enter the line of response data set; however they do reduce signal by losing true coincidences which might have been recorded using a smaller τ_c.

More troublesome than multiple coincidences are random coincidences where a

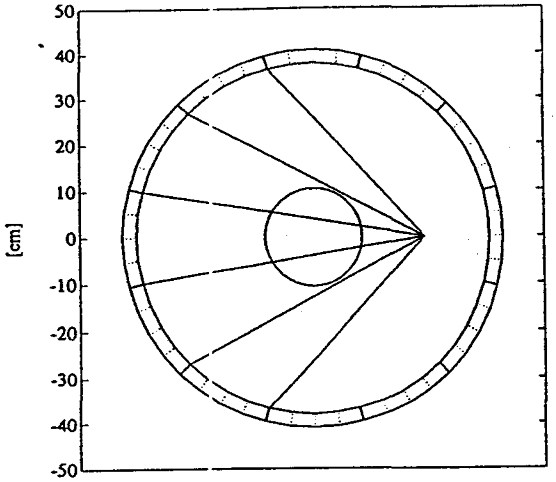

Figure 3a - There are 12 buckets in one ring of the McMaster PET scanner (SIEMENS/CTI ECAT 953).

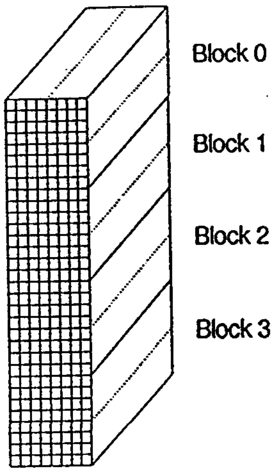

3b - Blocks and detectors in one bucket.

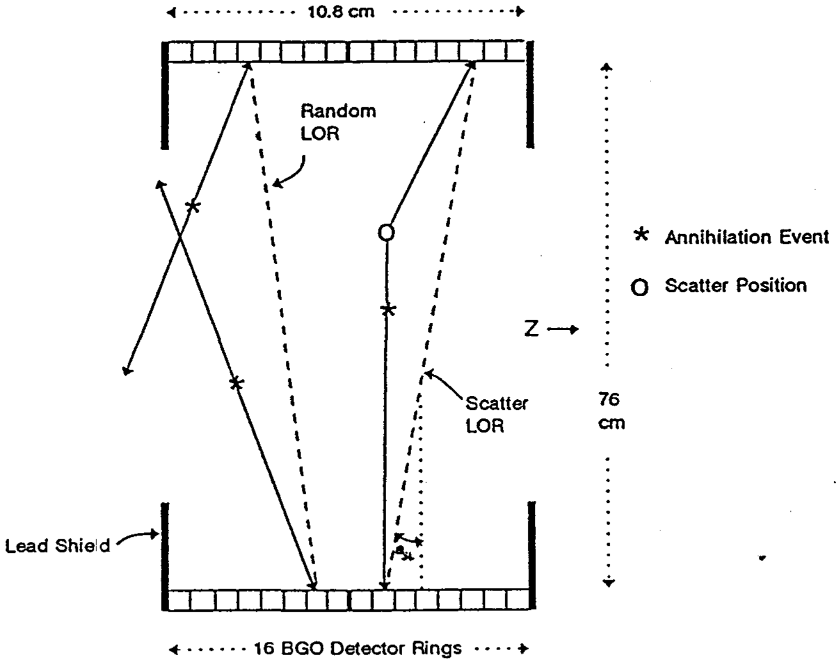

Figure 4: Random and scatter LOR's (coincidences).

single photon from each of two separate positron annihilation events strike detectors within τ_c, thus entering the line of response (LOR) data set (fig 4). Random coincidence events incorrectly assume an annihilation event occurred along a particular LOR producing additional noise in the data. The random count rate could be estimated by the equation:

$$R_{12} = \tau_c r_1 r_2 \qquad (1.11)$$

where r_1 and r_2 are singles count rates for two detectors and τ_c is the coincident timing window (Knoll, 1989).

A second source of noise in the acquired LOR data set occurs when one or both of the annihilation photons from an annihilated positron Compton scatters, thus changing direction and striking a different detector than had the photons remained unscattered (fig 4). This causes a "false" LOR to be recorded as the annihilation event becomes mispositioned. Only unscattered photons arising from a single annihilation event are true representatives of the positron isotopes spatial distribution. The problem of correcting for random and scatter coincidences in the data set is described in more detail in the data corrections section below.

Sinograms

When a pair of photons strike a pair of detectors in coincidence, it is assumed that a positron annihilated somewhere along the line joining the two detectors. This line is referred to as a line of response (LOR). In the ECAT-953, there are two adjacent rings of 48 BGO block detectors so that effectively 16 rings of crystal element detectors exist with 384 crystal detectors per ring. Such a large array of detectors produces many LOR's to be sampled which must be organized in some fashion to collect the data. Since the number of counts along each LOR is a measure of the line integral through the positron isotope distribution connecting the detectors, the LOR's are in effect projections through the isotope distribution. The LOR's are thus organized into parallel projections where all parallel LOR's for detectors within a crystal plane form a projection along a certain angle, θ.

PET's coincidence processor allows each detector to be in coincidence with the 160 opposing detectors across the field of view. Such a coincidence processor allows 160 parallel LOR's for each projection angle, θ, where 192 distinct projection angles are possible. Each LOR can thus be described by its radial distance from the center of the FOV, r, and by the angle of the LOR, θ (fig 5a). The projection data, $p(r,\theta)$, is stored in a matrix 192 elements high by 160 elements wide where each element corresponds to a particular detector pair. The LOR data is referred to as a sinogram because a point source off-center in the FOV traces a sine curve in the data matrix (fig 5b). A centered point source produces a horizontally centered thin vertical line in the sinogram.

Both 2D and 3D acquisition modes are available for PET. In 3D mode, coincidences may occur between detectors of any of the 16 crystal detector rings, so that 16 x 16 = 256 coincidence planes exist, each requiring a separate sinogram to record its projection data. In 2D mode, coincidences are only recorded for detector pairs within three crystal rings of each other ($\Delta sl \leq 3$) (fig 6). 16 direct planes are formed from

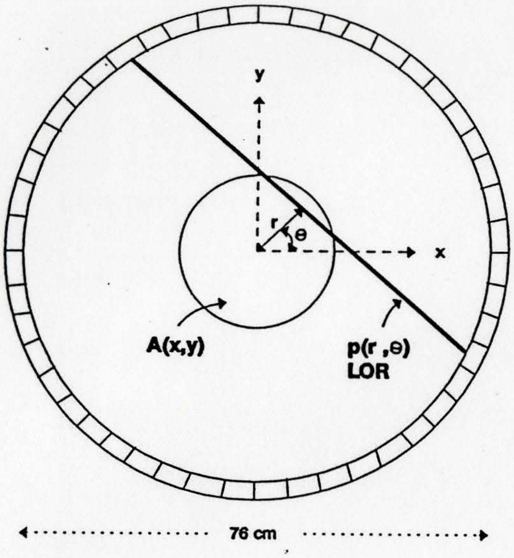

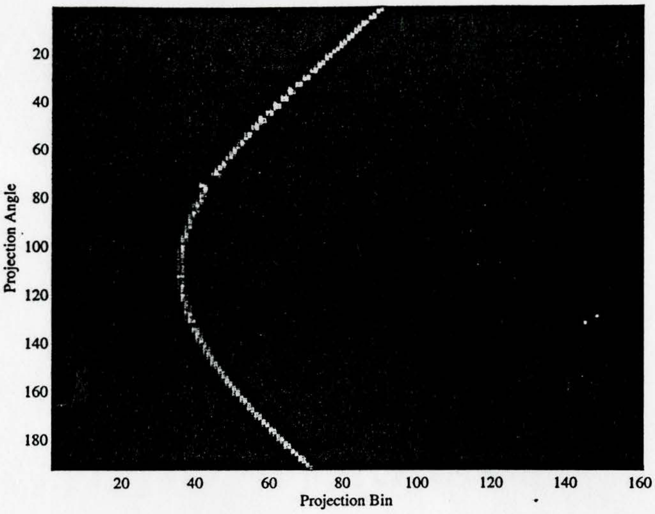

Figure 5(a): Line of response definition.

Figure 5(b): Sinogram of a point source in air, 15 cm off center.

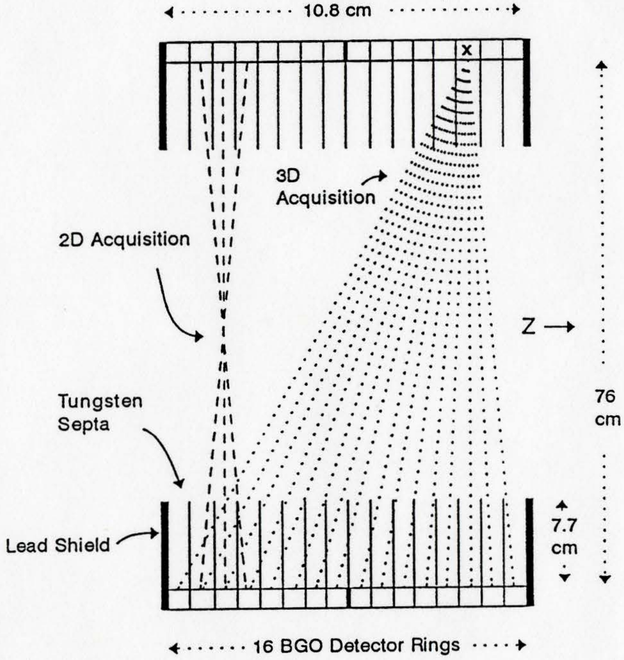

Figure 6: 2D acquisition vs 3D acquisition. The 3rd ring direct plane for the 2D acquisition as well as the coincidence pattern of detector x for the 3D acquisition is shown. The collimating effect of septa is apparent.

coincidences within the same ring (Δsl = 0) or two rings apart (Δsl = 2), while 15 cross planes are formed between the direct planes from coincidences with slice offsets of one or three (Δsl = 1 or Δsl = 3). 31 coincident planes or sinograms are thus required to record a 2D acquisition. 2D sinograms contain projection data approximately describing the isotope distribution at a particular axial position, z, so that the 31 sinograms can be reconstructed as images of an object in axial slices.

Image Reconstruction

Image reconstruction is achieved using projection data, p(r,θ), which has been measured and stored in the sinogram matrices. Projection data is equivalent to a line integral through the isotope distribution given by:

$$p(r,\theta) = \int A(x,y)\, ds \qquad (1.12)$$

where A(x,y) is the spatial distribution of the isotope density and s is the line of response (LOR) between two coincident detectors (fig 5a). In PET, the coincident count rate for each LOR is proportional to the line integral through the isotope distribution along that line.

Two types of methods for reconstructing the image matrix A(x,y) from the projection data p(r,θ) exist; analytic and iterative reconstruction (Brooks and DiChiro, 1976). In simple, unfiltered, backprojection, the isotope distribution image A(x,y) is calculated by summing the counts in a given projection to all pixels along the projection line according to the equation:

$$A(x,y) \propto \int p(r,\theta)\, d\theta \qquad (1.13)$$

or for discrete projections in PET:

$$A(x,y) \propto \sum_{LOR's} p(xCOS\theta + ySIN\theta, \theta) \qquad (1.14)$$

where the summation occurs over all lines of response. Simple backprojection is inaccurate however, since backprojection is not the inverse of projection (Webb, 1988). That is, the counts in a projection LOR do not originate from positron annihilations occuring with equal probability from all points on the line but instead have a particular distribution along the line of response.

A filtered backprojection technique improves upon this by first convolving the projections with a filter function before backprojecting. By relating projection and image data using Fourier Transforms, a ramp convolution filter proves appropriate when variables are changed from rectangular to polar coordinates within the Fourier Transform (Herman, 1979). The rectangular window used to bound the ramp function may produce ringing artifacts, however a variety of other windows have been employed to reduce this effect.

The second means of reconstructing images is through an iterative reconstruction technique. Iterative reconstruction functions by first making an initial estimate of the image distribution. Projection data is then calculated by forward projecting (computing line integrals) through the image and comparing the measured projection data with the projection data obtained from forward projection. An iteration rule is then applied to the calculated projections and a new image distribution created by backprojection of a correction factor. This process continues in a loop until the measured and calculated projections agree within some tolerance level determined by the stopping rule. The effectiveness of the iteration rule modifying the calculated projections and the choice of stopping rule greatly determines the rate of convergence and the number of iteration cycles required (Brooks and DiChiro, 1976).

Filtered backprojection is the most frequently employed reconstruction method since it is fast and produces sufficiently accurate images when good projection data with fine sampling is available. Additional computational resources needed to perform iterative reconstruction have not improved image quality enough to popularize it.

Image reconstruction algorithms can be applied either in two or three dimensions. 3D image reconstruction uses a cubic grid, A(x,y,z), rather than a square grid, A(x,y), and requires backprojection through the entire volume, greatly increasing computation time. However, 3D image reconstruction is an attractive method since projections between crystal rings with slice offsets greater than three may contribute to the reconstruction process, enhancing the quality of the images by reducing statistical noise. With faster reconstruction algorithms and improved computer resources, 3D image reconstruction has just recently approached feasibility.

Data Correction

If not corrected for, projection data, which has been acquired and stored in sinograms, would suffer from a variety of systematic errors that would produce qualitative and quantitative inaccuracies in reconstructed images. Limitations in detector performance require certain corrections such as dead time and normalization correction. Finite recovery times needed by detectors struck by a photon result in some counts being lost if a second photon strikes the detector while it is still recovering. Dead time correction rectifies this problem. The differing sensitivities of each BGO detector results in a different sensitivity for each pair of detectors which must be accommodated for by normalization.

The coincidence detection method requires a separate correction to eliminate those pairs of photons striking detectors which come from different annihilation events occurring within the timing coincidence window, τ_c, of the tomograph. A real time correction using a delayed coincidence window achieves this. The final source of inaccuracy results from interactions of the annihilation photons within the object itself. Photoelectric absorption and Compton scattering remove counts from LOR's which otherwise would have registered had the object not attenuated one or both of the annihilation photons. Attenuation correction schemes restore LOR count rates to their appropriate levels by measuring or calculating the amount of attenuation along each line of response. Scatter correction schemes remove those counts in LOR's which resulted from one or both annihilation photons Compton scattering causing a mispositioned event in a false LOR.

Dead Time

A minimum amount of time called dead time must pass before an activated detector is capable of recording a second event. This limiting time for the detection system to become active again, after an event, may be determined by the physical processes within the BGO crystal itself or by the PMT's and their associated electronics. For PMT-scintillator systems, the time for the scintillation photons to completely flush out of the crystal into the PMT's is the major cause of dead time. BGO has a 300 ns decay constant responsible for much of the dead time in the tomograph.

Two models for estimating dead time are the non-paralyzable and paralyzable models. Both models assume any events occurring within a dead time, τ, after an initial detected event will be lost. However, the paralyzable model differs from the non-paralyzable one in that the dead time of the detectors will be extended by a period τ after any subsequent events strike the detector while dead. Events striking detectors which are dead have no effect in the non-paralyzable model. The equations used to describe each model are as follows:

$$\begin{aligned} m &= n\,e^{-n\tau} && \textit{PARALYZABLE} \\ n &= \frac{m}{1-m\tau} && \textit{NON-PARALYZABLE} \end{aligned} \qquad (1.15)$$

where m is the measured count rate, n is the true count rate and τ is the dead time.

For high count rates, the non-paralyzable model predicts a maximum measured count rate of $1/\tau$ while the paralyzable model actually has a reduced measured count rate as the event rate increases beyond τ. The detector becomes "paralysed" by the high count rate and never survives its dead period without subsequent events occurring, thus preventing its becoming live again.

In reality, neither model perfectly describes a detection system as elements of both models are observed. BGO-PMT systems exhibit predominantly paralyzable characteristics as a result of BGO's 300 ns decay constant for flushing out scintillation photons, extending the time before the pulse returns below the trigger voltage. Any events occurring before the BGO flushes out its photons will result in more scintillation photons being created, extending the deadtime by τ from this moment. Pulse pile-up may occur if two events strike a detector close together in time causing the pulse amplitudes to sum and the energy to be falsely recorded as being large. Pulse pile-up affects the observed spectrum of detectors.

Normalization

Each BGO crystal detector has a slightly different sensitivity for detecting 511 keV gamma rays that may be accounted for by using a normalization procedure. For the ECAT-953 PET scanner, normalization is achieved by scanning a uniform activity, cylindrical phantom (Siemens PET Hardware Manual, 1991). First the photomultiplier tube gains for each BGO block detector are adjusted until consistent amplification is achieved. Plane efficiency scans are then acquired to compute the plane efficiency of the

31 planes (2D mode) or 256 planes (3D mode). Normalization scans then measure the sensitivity for each of the BGO crystal element detectors and finally, normalization factors are calculated for each pair of detectors based on their individual sensitivities. The normalization factors for each line of response are stored in normalization sinogram matrices which pre-multiply all acquired emission sinograms during reconstruction to perform the normalization correction. The measurements required to complete the normalization procedure may take 8-10 hours to perform.

Randoms

Random coincidences arise when a photon from two separate annihilation events strike detectors within the timing coincidence window, τ_c, thus entering the LOR data set. Such coincidences cause the false assumption that an annihilation event occurred between the two activated detectors thus affecting the reconstructed image. One means of estimating the random count rate could be from detector singles rates according to equation 1.11, however the ECAT-953 scanner uses a delayed coincidence window method instead.

The delayed coincidence method works by activating the coincidence circuit, after some time delay, for the 5 opposing buckets of a triggered detector across the field of view. This time delay must be larger than the maximum time difference of detection possible for two photons released by an annihilation event. Any "delayed coincidences" recorded must then be a result of separate annihilation events and hence, an estimate of the random coincidence rate. The randoms correction is implemented by subtracting counts from the sinogram in those LOR's which recorded delayed coincidences.

Attenuation

When one or both of the annihilation photons undergoes either a photoelectric or a Compton interaction in the object, a coincidence count is lost from the line of response which otherwise would have registered had the photons continued unimpeded along their paths to detectors. Attenuation correction methods attempt to restore the LOR count rates to their appropriate levels by estimating the amount of attenuation along each line of response. The equation describing attenuation of annihilation photons is given as:

$$M = T[e^{-\mu(x)x_1} \cdot e^{-\mu(x)x_2}] = T[e^{-\mu(x)(x_1+x_2)}] \qquad (1.16)$$

where M is the measured count rate for a particular LOR, T is the true number of annihilation photons initially travelling along the LOR, $\mu(x)$ is the position dependent attenuation coefficient and x_1, x_2 are the distances to the edge of the object from the annihilation position for each photon. The attenuation correction factor for each LOR is thus (deKemp, 1992):

$$ACF = \frac{T}{M} = e^{\mu(x)(x_1+x_2)} \qquad (1.17)$$

The annihilation position along the LOR is unimportant for attenuation correction since the x_1, x_2 terms sum in the exponent. This fact is utilized by measured attenuation correction methods which employ a rotating rod source of positron emitter circling the object around the FOV. Blank and transmission coincidence sinograms are then acquired without and with the object being scanned in place. The ratio of the blank to the transmission sinogram estimates the ACF's for each LOR so that attenuation correction is applied by scaling the emission sinogram by the ACF values for each LOR. Measured attenuation correction suffers from Poisson noise problems, since short transmission scans are desirable to minimize patient scanning times.

Recent efforts at measured attenuation correction using singles count rates greatly reduce ACF noise by increasing LOR count rates (deKemp, 1992). Singles attenuation works by creating a LOR from a singles count by projecting a line from the detector recording the singles count back through the known position of the rotating rod source to a detector which is assumed to be the detector which would have been in coincidence with the singles detector.

Calculated attenuation correction may also be employed by estimating the shape of an object from an emission image and forward projecting along each LOR through the fitted shape to obtain the ACF's. It is assumed the object has uniform attenuation with the same attenuation coefficient as water (μ = 0.096 cm^{-1}). Although calculated ACF's have no Poisson noise, the assumption of uniform attenuation equivalent to water is dubious, particularly for scans involving the chest. Even the selection of object boundaries may be inaccurate since the isotope need not exist throughout the object to define its edges.

Attempts to utilize the strengths of both measured and calculated attenuation methods are called hybrid methods. Hybrid methods involve reconstructing a measured attenuation map which contains Poisson noise and computer fitting several attenuation regions from this map to represent bone, soft tissue and air regions (Tomitani, 1987). Forward projection through this fitted shape produces noise free ACF's without the assumption of uniform attenuation being as rigid. The procedure is laborious however, leaving singles attenuation correction the most attractive method currently being explored.

Scatter

Scatter coincidences are recorded when one or both 511 keV annihilation photons are Compton scattered in the object and recorded in a different line of response than had the photons travelled unimpeded towards the detectors. These mispositioned events result in a loss of image contrast since the annihilations in high activity (hot) regions are mispositioned to regions of lower concentration (cold) making the observed levels in these regions appear more alike. Quantitative accuracy in the images is thus also compromised.

The two properties of Compton scattered photons are that they have changed direction and are at a lower energy than when initially released. These properties are the basis for scatter exclusion techniques, which prevent scatter coincidences from entering sinograms during acquisition, as well as scatter correction techniques, which estimate the amount of scatter in each LOR that failed to be excluded and so must be subtracted.

Scatter exclusion by detector energy discrimination is done by only allowing coincidences to be recorded when both detectors record energies within some energy range, typically 250 keV to 850 keV. This allows the unscattered 511 keV photons to enter the data set while hopefully excluding some of the lower energy scattered photons which fall below the lower level discriminator energy (250 keV). The 25% energy resolution of BGO causes the observed spectrum for 511 keV photons to be half of the peak value for energies as low as 380 keV. This prevents the use of a lower level discriminator much greater than 380 keV without experiencing significant signal loss. Unfortunately, 511 keV photons exhibit little energy loss for large angle scattering, making their exclusion by energy discrimination ineffective. For example, using equation 1.9, a photon scattered through 45° still has an energy of almost 400 keV. If the location of such a scatter were the center of the tomograph's field of view, the coincidence would be mispositioned nearly 15 cm from the location of the annihilation event. Energy discrimination only proves effective for excluding coincidences that have multiply scattered photons which exhibit significant energy loss.

For 2D acquisitions (see page 21), scatter exclusion is performed by placing 15 annuli of tungsten, called septa, to collimate each of the 16 crystal detector rings of the ECAT-953 (fig 6). The tungsten collimators are each 1 mm thick and extend 7.7 cm from the surface of the detectors towards the center of the field of view. Septa help exclude scatter coincidences whose scatter angles have a component along the axial direction, z, since such photons must pass through the tungsten to reach a detector. Scatter occurring through an angle within a trans-axial plane need not pass through the septa to reach a detector and so such scattered photons are not excluded.

2D acquisitions with septa and a lower level discrimination (LLD) setting of 250 keV often experience scatter fractions (percent of data containing scatter coincidences) of 10-20%, depending on object size and source distribution. This scatter fraction is considered acceptable and so reconstructed images of 2D acquisitions experience limited contrast loss and quantitative inaccuracy. 3D acquisitions, which include all possible LOR's between detectors of any of the 16 crystal rings, cannot use septa so the observed scatter fraction may be as high as 50% with a LLD of 250 keV. Recent improvements in 3D reconstruction techniques have made this mode of operation more attractive; however in order to realize the benefits of 3D reconstruction (page 25), a means of correcting for scatter coincidences must be developed. The scatter correction methods explored to date involve either energy considerations, using the property that scattered photons are at lower energies, or measurements of point spread functions (PSF's), using the property that scattered photons change direction. The main scatter correction techniques derived from these two properties are further explored in Chapter II.

CHAPTER II

Scatter Correction Techniques

Scatter correction techniques typically employed in PET are categorized either as energy based scatter correction techniques or as filtered scatter correction techniques. Energy based scatter correction techniques rely on the fact that Compton scattered photons are at a lower energy than unscattered photons at 511 keV. Several methods utilizing this principle are described. Filtered scatter correction techniques require the evaluation of scatter point spread functions (PSF's) at any location within any non-uniform object being scanned. The mathematical convolutions required to evaluate scatter profiles from PSF's are described along with the means employed to obtain realistic PSF's. Other scatter correction schemes not representative of either correction category are also described for completeness.

Introduction

Scatter correction techniques were first developed for single photon emission computed tomography (SPECT) systems in the late 1970's before PET systems became widely available. Since SPECT systems were and are more numerous than PET systems, much work was done in developing SPECT scatter correction techniques. PET scatter correction techniques have, to a large extent, been developed by paralleling the techniques derived for SPECT.

The danger of developing a PET scatter correction method based on a previously successful SPECT scatter correction scheme is that scatter possesses different properties in the two imaging systems. A SPECT system is essentially a gamma camera which rotates around the object being imaged to acquire multiple angle projections (Jaszczak et al, 1980). Gamma cameras have lead collimators in front of their NaI(Tl) scintillation detectors so that only photons travelling normal to the face of the camera will be detected. Scatter events are therefore entirely contained within the boundaries of the object since no material exists outside of the object to scatter photons such that they are normal to the gamma camera face. The two photon nature of PET coincidences allows scatter events to exist in lines of response which do not pass through the object.

A second difference in scatter profiles occurs as a result of the lower energy photons emitted by isotopes used for SPECT systems. SPECT isotopes typically emit photons from 80-140 keV while PET photons are at 511 keV so that the PET photons will be somewhat more forward scattered than those of SPECT (see eqn 1.7). For instance, the Klein-Nishina equation (eqn 1.7) predicts the probability of a 511 keV photon scattered through a 45° angle to be 47% that of a photon scattered at a 0° angle. The corresponding ratio for 80 keV photons is 69%. Any assumptions used for SPECT scatter correction which involve an isotropic scatter distribution will thus be less successful for PET. Finally, the 25% energy resolution of BGO detectors, often used in PET, perhaps diminishes the effectiveness of energy spectrum based scatter correction techniques developed for the 10% energy resolution NaI(Tl) detectors which are common in SPECT. Such differences between PET and SPECT scatter distributions must be considered before attempting to modify a SPECT scatter correction technique for use in PET.

The original and simplest means of correcting for scatter is called the reduced μ method of scatter correction (Yanch et al, 1990). The technique is applied during attenuation correction by using a value for the linear attenuation coefficient, μ, which is lower than the true value. Using the full value of μ predicts how many photons will be removed from a narrow beam of radiation due to absorption and scatter; however it ignores the number of photons scattered into the path from other directions. The broad beam conditions of SPECT and PET systems cause the center of a uniform activity object to appear hotter than the edges if the proper μ is used. The justification for undercorrecting attenuation with a reduced value of μ is that a portion of the attenuated primary photons are replaced with the same number of scattered photons (Yanch et al, 1990). Although image quality is enhanced by the reduced μ technique, improvements in image quantification are only minimal since the method assumes all locations in the image are affected by scatter to the same extent. This is not the case for non-homogeneous source distributions. More sophisticated means of performing scatter correction should compare their improvements to images reconstructed using a reduced μ rather than images employing no scatter correction technique at all since the reduced μ method is fast and easy to implement.

Two dominant types of scatter correction techniques emerged from the work on SPECT systems: energy based correction methods and filtering correction methods (Jaszczak, 1985). Energy based scatter correction uses the property that scattered photons are lower in energy and so may be separated from unscattered photons in some way. The superior energy resolution of NaI(Tl) detectors (10%) relative to BGO detectors (25%) have made exploration of these methods more common in SPECT instruments using NaI(Tl) detectors, however some energy based methods have been attempted for PET instruments equipped with BGO detectors. Deconvolution and convolution subtraction methods attempt to estimate the scatter point spread function (PSF) for a point source of activity in the object being scanned. The scatter PSF is the scatter profile observed from a point source in all image planes from all projection angles. Since a radioisotope distribution acts as a collection of point sources, filtering methods such as deconvolution or convolution subtraction may estimate scatter profiles for distributed sources if accurate PSF's can be determined.

Energy Based Scatter Correction

Energy based scatter correction uses the property that scattered photons are at somewhat lower energies than unscattered photons facilitating their removal from the data set. Five energy based methods for reducing scatter are described in the following section. The first two methods are scatter suppression or exclusion techniques which attempt to reduce the amount of scatter counts entering the data set during acquisition while the other three methods attempt true scatter correction by estimating the amount of scatter which entered the data set and subtracting it after acquisition. All methods were originally developed for SPECT, and only one of these correction techniques, the dual energy window method, has been attempted for PET.

Asymmetric Windows Around Photopeak

Normally in SPECT, lower and upper energy discrimination levels are set to be symmetric about the photopeak energy of the isotope being used, with a pulse width typically of about 20%. The asymmetric windows method performs scatter suppression by raising the 20% pulse width energy levels until the count rate is reduced to 80% for a point source in air (Koral et al, 1986). The idea is that the Compton photons, being of lower energy than the unscattered photons, will be removed with greater frequency producing a reduced scatter fraction in the data.

The problem with this method is that it reduces signal count rates thus producing noisier images while failing to remove a large portion of Compton scattered photons, as these may possess energies as high as the photopeak energy. In fact the Klein-Nishina equation (eqn 1.7) predicts that 0° angle scatter at the photopeak energy has the largest cross section, particularly as photon energy increases. For PET, this method is essentially equivalent to raising the lower level discriminator to remove greater amounts of Compton scatter while sacrificing signal to a greater extent. However, the poorer resolution detectors of PET cause the discrimination to be less effective than for SPECT. The method has proven effective for SPECT only for quantification of very high activity lesions in low background levels where Compton scatter fractions are low (Koral et al, 1986).

Energy Weighted Acquisition

Energy weighted acquisition (DeVito et al, 1989) attempts to account for the fact that photons measured at a particular energy result from either unscattered photons recorded at a lower energy due to energy resolution effects, or from scattered photons which truly are at a lower energy. The probability of a photon being scattered rather than unscattered increases in a continuous way as the detected energy of the event decreases. For this reason, energy weighted acquisition assigns a weighted count to the data set, with higher energy detected photons having a greater weight. This is a more sophisticated means of acquisition than windowed acquisition, where all events recorded above the lower level discriminator (LLD) are assumed to be unscattered photons and all detected events below the LLD are assumed to be scatter events.

A difficulty with energy weighted acquisition is selecting the appropriate weighting functions to estimate the probability of a recorded count being from an unscattered photon. Also, the technique is merely a scatter suppression technique and not a correction technique since scattered photons still enter the data set but with a lower probability than when using windowing. Cold spheres in hot backgrounds displayed a drop in scatter levels from 40% to 27% (DeVito et al, 1989). This sizable remaining scatter level requires further scatter correction by some other technique. Energy weighted acquisition has not been attempted for PET. However, it is likely the poorer energy resolution of BGO would further reduce the effectiveness of the technique.

Split Photopeak

The split photopeak scatter correction method functions by acquiring data in two adjacent non-overlapping energy windows of equal size on either side of the photopeak energy (King et al, 1992). The idea is that the proportion of Compton scattered photons will be greater in the lower energy window than in the higher energy window. This is unlike the unscattered counts which will be equally distributed in both windows. King et al used a regression relation of the form:

$$SF = A \cdot R_s^B + C \tag{2.1}$$

to estimate the total scatter in the photopeak (SF • total photopeak counts) where A, B and C are calibration coefficients and R_s is the ratio of scatter counts in the lower window over those in the higher window.

A similar type of approach using split photopeak acquisition windows was attempted where the four governing equations were given as:

$$\begin{aligned} U_L + S_L &= T_L \\ U_H + S_H &= T_H \\ U_L / U_H &= K_1 \\ S_L / S_H &= K_2 \end{aligned} \tag{2.2}$$

where U are unscattered count rates, S are scatter count rates and T are total count rates in the lower (L) and upper (H) windows while K_1 and K_2 are measured coefficients (Pretorius et al, 1993). K_1 is measured with a source in air and should be equal to one if the detectors are correctly calibrated for energy. K_2 is assumed to be a constant for all bins, independent of source or object distribution, in the hope that scatter spectra shape will remain reasonably constant in the 0° angle scatter region around the photopeak. Solving the four equations gives the total photopeak count ratio of:

$$U_L + U_H = \frac{(K_1 + 1)\,(K_2 T_H - T_L)}{K_2 - K_1} \tag{2.3}$$

The unscattered count rate can thus be derived from the total count rates in each window.

The problem with the method is the assumption of a constant ratio of scatter counts in each window since such a ratio is object dependent. Bins located on the periphery or exterior to the object experience a larger shift to lower energies because of the larger angle scatter events which are mispositioned away from the object. Even slight differences are greatly magnified by the presence of the $(K_2\text{-}K_1)$ term in the denominator. Difficulties in keeping the instrument precisely calibrated so that $K_1 \approx 1$

are also a problem. The method has obtained some success for simple phantom studies in SPECT (King et al, 1992) however extrapolation to PET would be more difficult as a result of the poorer energy resolution of BGO.

Multiple Windows

Multiple window scatter correction techniques require the acquisition of data in a number, usually 32, of contiguous energy windows extending over the energy spectrum from the backscatter peak to above the photopeak (Koral et al, 1988). The observed spectrum will be a combination of the unscattered and the scattered spectra according to the equation:

$$T_i = U_i + S_i \tag{2.4}$$

where T_i is the total observed spectrum, and S_i and U_i are the scattered and unscattered components in energy bin i, for a particular line of response. Assuming that the unscattered spectrum will be a scaler of a point source in air, and that the scattered spectrum can be fit by a 3rd order polynomial, the following equations can be derived:

$$\begin{aligned} S_i &= a_o + a_1 i + a_2 i^2 + a_3 i^3 \\ U_i &= K f_i \end{aligned} \tag{2.5}$$

where K is the scaler, and a_o, a_1, a_2 and a_3 are the fitting parameters with f_i being the spectrum of a point source in air. The measured spectrum for a line of response, M_i, is compared with the estimated total spectrum, T_i, to fit the five parameters using matrix fitting operations through the minimization of $| M_i - T_i |$.

A more sophisticated solution to the above equations was later applied by Gagnon using data matrices with co-variance statistics techniques (Gagnon et al, 1989). Only 10-15 energy windows were used to preserve sufficient statistics in each of the windows.

The special hardware required to acquire the multiple projections at various energies is a drawback of the technique. The process of performing the matrix minimization to fit the parameters is time consuming, even with the use of a coarse data set, permitted because of the smooth nature of the scatter profiles. Although the procedure is sound theoretically, the difficulties in implementing such a procedure have no doubt inhibited its application to PET systems.

Dual Energy Windows

The dual energy window (DEW) scatter correction method acquires data in two non-overlapping energy windows. In addition to the photopeak window containing the isotope's photon emission energy, a second lower energy Compton window is acquired to estimate the distribution of Compton scattered photons recorded at below photopeak energies. The idea was first introduced for SPECT by Jaszczak and is governed by the equation:

$$U(x,y) = T(x,y) - K \cdot C(x,y) \qquad (2.6)$$

where U(x,y) is the scatter corrected image, T(x,y) is the measured image, C(x,y) is the Compton image reconstructed from the lower energy window data and K is a scaling constant equal to the ratio of Compton events in the photopeak window over those in the scatter window (Jaszczak et al, 1984). The DEW technique can be applied either in image space, as described above, or in projection space, by appropriately subtracting sinogram data acquired in each window.

There are three assumptions of the DEW technique. The first is that all counts in the Compton window originate from Compton scattered photons alone. Secondly, the profile of Compton scattered events in the Compton window are similar to those in the photopeak window, exhibiting similar scatter line spread functions. Finally, the scaling constant, K, obtained by measurements on simple phantoms, will be constant for all object and source distributions for given energy window settings. The above assumptions were verified for SPECT by Monte Carlo simulations of simple phantoms (Floyd et al, 1985). DEW was demonstrated to have some success in cardiac imaging, particularly for ^{201}Tl, whose low energy photons (72 keV) most closely approximated isotropic scattering, hence satisfying the second DEW assumption (Galt et al, 1992).

The DEW technique was modified for use in PET, with an improvement to eliminate the first assumption that all counts in the Compton window be from scattered photons (Grootoonk et al, 1993). This was accomplished using the following governing equations:

$$\begin{aligned} P_T &= P_S + P_U \\ C_T &= C_S + C_U \\ R_S &= C_S / P_S \\ R_U &= C_U / P_U \end{aligned} \tag{2.7}$$

where P is the photopeak window, C is the Compton window and T, S and U are the total, scattered and unscattered count rates respectively. R_S and R_U are ratios of scattered and unscattered count rates of the Compton window over the photopeak window. These are assumed to be constant for given energy settings for all objects and source distributions. This modified DEW technique only requires that each window have different ratios of scattered and unscattered events rather than scatter events exclusively in the Compton window. Solving these four equations (eqn 2.7) for unscattered events in the photopeak yields:

$$P_U = \left(\frac{R_S}{R_S - R_U}\right) P_T - \left(\frac{1}{R_S - R_U}\right) C_T \qquad \textbf{(2.8)}$$

The energy windows were set at 200-380 keV for the Compton window and 380-850 keV for the photopeak window, while the ratios were calculated at these energies for line sources centered in water phantoms (R_S) and in air (R_U).

Although moderate success was reported for brains scans, the technique suffers when imaging non-uniform attenuation objects as in cardiac imaging. Attempts to generalize the DEW technique for spatially varying media in SPECT may alleviate this problem, however the solution is so complex as to destroy the strength of DEW, which is its simplicity of application (Smith and Jaszczak, 1994). The higher energy photons of PET are inherently more forward scattered than low energy SPECT photons resulting in a degradation of the second assumption (Thompson, 1993). This problem is further discussed in Chapter IV with the assistance of some Monte Carlo simulations.

Filtered Scatter Correction

Post-acquisition scatter correction techniques are another predominant means of correcting for scatter in PET and SPECT systems. Such techniques, applied to the projection data before reconstruction, require the use of point spread functions (PSF's) to estimate the response of a point source of radioactivity at any position within the object being scanned. Since images are equivalent to a superposition of many independent point sources, performing either convolution subtraction or deconvolution on the acquired projection data allows an estimate of the scatter profiles in each plane and projection angle to be established.

To perform accurate scatter estimation, point spread functions which vary according to the object mass distribution and source position within the object are required. Attempts to develop such position and object dependent PSF's are further described in the section on PSF determination below (page 53) and are the subject of this thesis.

Filtering Operations

Convolution techniques for performing scatter correction consider the measured projections, T, to be the sum of an unscattered component, U, and a scattered component, S. Two methods for modelling the scatter component exist: Deconvolution and convolution subtraction.

The deconvolution method was initially proposed for SPECT (Floyd et al, 1985) but has more recently been applied to PET as well (McKee et al, 1992). In deconvolution, the scatter component is modelled as a convolution of the unscattered projections, $U_\phi(r,z)$, with some scatter point spread function, $K(r-r',z-z')$. The parameter r refers to a particular bin in a projection at a particular angle, ϕ, stored in a single sinogram. The parameter z refers to the mean axial position of line of responses located in different projection planes and stored in different sinograms. The equation describing this convolution with unscattered projections is given as:

$$\begin{aligned} S_\phi(r,z) &= U_\phi(r,z) * K(r-r',z-z') \\ &= \sum_{r'}\sum_{z'} U_\phi(r',z') \cdot K(r-r',z-z') \end{aligned} \qquad \textbf{(2.9)}$$

where the summation is over all bins of all projections for a projection angle of ϕ. The above equation, modelling scatter, and the equation describing measured projections (T=U+S) combine to give:

$$\begin{aligned} T_\phi(r,z) &= U_\phi(r,z) + S_\phi(r,z) \\ &= U_\phi(r,z) + U_\phi(r,z) * K(r-r',z-z') \\ &= U_\phi(r,z) * [\delta(r-r',z-z') + K(r-r',z-z')] \end{aligned} \qquad \textbf{(2.10)}$$

where $\delta(r-r',z-z')$ is the Dirac delta function. Taking the Fourier transform of each side of the equation:

$$FT(T) = FT(U) \cdot FT(\delta + K) \qquad \textbf{(2.11)}$$

where FT is the Fourier transform operator. Re-arranging to solve for the desired unscattered projections produces the equation:

$$U = FT^{-1}\left[\frac{FT(T)}{FT(\delta + K)}\right] \qquad \textbf{(2.12)}$$

The weakness of the method is the need to use a position independent point spread function, K(r-r′,z-z′), with no functional dependence on r or z alone. Taking the Fourier transform of K is only possible if the function is position independent, contrary to the observation that the PSF is object density and source position dependent (Jaszczak, 1985). The strength of the deconvolution method is its speed because using filtered Fourier backprojection reconstruction (see page 24), as is most common, allows the deconvolution to be done in Fourier space. The technique can then be implemented as a simple modification of the filter used in Fourier backprojection.

Convolution subtraction was first proposed for PET (Bergstom et al, 1983) and later for SPECT (Axelsson et al, 1984). It works by modelling the scatter component, S, as a convolution of the measured projections, T, with a point spread function, K, according to the equation:

$$\begin{aligned} S_\phi(r,z) &= T_\phi(r,z) * K(r-r',z-z',r',z') \\ &= \sum_{r'}\sum_{z'} T_\phi(r',z') \cdot K(r-r',z-z',r',z') \end{aligned} \qquad \textbf{(2.13)}$$

The unscattered projections could be estimated by performing the above convolution to estimate the scatter profiles, then subtracting the scattered component from the measured projections to give:

$$U_\phi(r,z) = T_\phi(r,z) - S_\phi(r,z) \qquad \textbf{(2.14)}$$

Reconstruction of the unscattered projections can then be done to produce a scatter free image.

The strength of convolution subtraction is its ability to use a flexible point spread function, K(r-r′,z-z′,r′,z′). It is mathematically permissible to use a position dependent PSF since no Fourier transform is required. Such methods are referred to as spatially varying convolution methods, as opposed to the spatially invariant methods of deconvolution techniques, because the observed PSF variations due to object density or source position differences can be incorporated into the technique. The problem with convolution subtraction is speed since a convolution to estimate scatter profiles and their subsequent subtraction from the observed projections must be done prior to reconstruction. The use of the total observed profile, T, instead of only the unscattered profiles, U, for convolution with the PSF's is less accurate and leads to an overestimation of scatter (Msaki et al, 1993).

To account for the problem of convolving with T, an iterative equation to estimate the scatter profiles using an estimate of the unscattered profile was suggested as follows (Shao and Karp, 1991):

$$S_{\phi}^{n}(r,z) = [T_{\phi}(r,z) - k \cdot S_{\phi}^{n-1}(r,z)] * K(r-r', z-z', r', z') \qquad (2.15)$$

where n is the iteration number and k is a relaxation parameter (0 < k < 1) used to avoid oscillation towards convergence between iterations. The estimate for the unscattered projections is shown within the square brackets in the above equation. The initial estimate for the unscattered projections is the total measured projections, T, scaled down by some factor to crudely account for scatter. Iterative scatter estimation is the most accurate means of performing scatter correction since position dependent PSF's are permitted and convolution with unscattered distributions may be employed.

Iterative convolution subtraction allows the PSF to vary for each bin of each projection at any angle in any image plane, however projection methods do not allow the PSF to vary for different source positions along a particular line of response (bin). The method available to permit this last PSF variability is called an image to projection method (Barney et al, 1993). For this method, the iterative convolution is done in image space using a reconstructed emission image, f(a,b,c), which is convolved with a real space point spread function, $K_\phi(r',z',a,b,c)$. K is the PSF in the ϕ projection direction for a point source at (a,b,c). The iterative equation resembles the projection space iterative equation above (eqn 2.15) and is given as:

$$S_\phi^n(r,z) = \sum_x \sum_y \sum_z f^{n-1}(a,b,c) \cdot K_\phi(r',z',a,b,c) \quad \textbf{(2.16)}$$

where the summation is over all image pixels defined by (a,b,c). The line of response represented by the variables r′ and z′ passes through the source at the image point (a,b,c) parallel to the LOR where scatter is being estimated at r,z. The iteration procedure is the same as for projection convolution subtraction except a new image, $f^n(a,b,c)$, must be reconstructed after each iteration, n, using the scatter subtracted projections, U_ϕ^n, from the last scatter estimation, S_ϕ^n. The initial estimate of f^0 is obtained by scaling down the measured projections, T_ϕ, to crudely account for scatter.

Image to projection methods represent the most sophisticated and theoretically accurate means of estimating scatter distributions since the point spread functions may vary with position along a LOR as well as from one LOR to another. However, the added sophistication does not produce sufficiently superior scatter estimates relative to iterative convolution subtraction of projections to warrant its routine use (Barney et al, 1993).

Iterative convolution subtraction of projections has become the technique of choice offering the best compromise between accuracy and speed of computation. For the ECAT-953 operated in 3D acquisition mode, double convolution to estimate scatter (eqn 2.15) over the 160 bins within a projection at angle, ϕ, and over the 256 sinograms at different axial positions and angles can be computationally demanding. To shorten the time to perform this convolution, the 3D dataset containing 256 sinograms is re-formatted into the 31 axial slices characteristic of a 2D dataset. The assumption is that scatter distributions do not vary with the angle of the sinogram plane from the axis of the tomograph and depend only on the bin, r, and the mean axial position of the sinogram plane, z (Bailey and Meikle, 1994). Convolution, then, need only occur over 31 sinograms rather than 256, which greatly enhances computing efficiency. After completion of the convolution, the scatter component in each of the 256 planes is extracted from the 31 planes by selecting the 2D plane with the same axial position as the 3D sinogram's mean axial position.

Another means of decreasing convolution time is to compress the data set by re-binning the sinograms into 96 angles with 80 bins rather than 192 angles with 160 bins (Wienhard and Lercher, 1994). This is permissible because of the smooth broad scatter distributions observed in PET, which vary little over adjacent bins. Using both data reduction methods contracts the size of the data set by a factor of 33.

Point Spread Function Determination

In order to have accurate scatter profile estimation using a convolution correction technique, point spread functions which are accurate for all source positions within objects of any material distribution are required. The first attempts to characterize the PSF's were by Bergstrom for PET (Bergstrom et al, 1983) and by Axelsson for SPECT (Axelsson et al, 1994). In both cases, PSF's were modelled by single exponentials according to an equation of the form:

$$K(r) = Ae^{-Br} \tag{2.17}$$

where r is the bin offset from the projection bin containing the point source and the parameters A and B are assumed constants for all source positions in all objects. The choice of a single exponential function to model the scatter profiles stems from the observation of linear profiles for line sources in water filled cylindrical phantoms when plotted on a semi-log graph (fig 7). Initially, line sources were used because only 1D convolution within a single projection at a particular angle was done to produce 2D reconstructed images. This corresponds to using equation 2.15 with convolution over r alone and no axial scatter considered. Such a simplified convolution is most effective only when little axial variation in isotope distribution exists. The actual values of A and B were determined by averaging the parameters measured for several source positions at a variety of radial offsets from the center of the water filled cylinder.

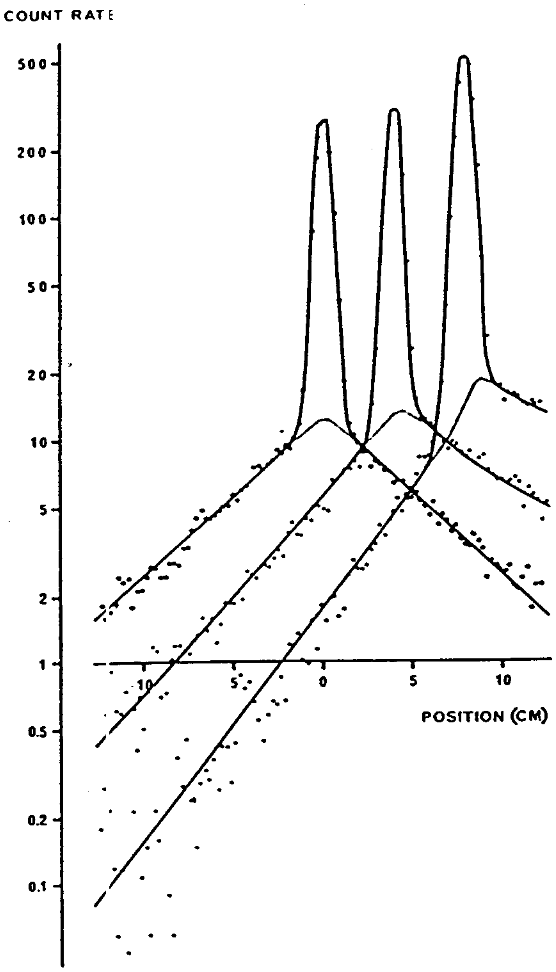

Figure 7: Projections plotted for a line source in a 20 cm water filled cylinder for three radial offsets (0 cm, 4 cm and 8 cm). The solid lines extending under the peaks are an exponential fit to the data points from PET experiments. Taken from Bergstrom et al, 1983.

Advancement to 2D convolution over r and z was suggested by Msaki for SPECT (Msaki et al, 1987) and later by Shao for PET (Shao and Karp, 1991). The use of such a double convolution greatly increases calculation time; however the scatter estimation will not suffer from axially varying isotope distributions as for 1D convolution. The choice of equation to fit the point spread function is much like for 1D convolution (eqn 2.17) however an axial exponential is included as in the following equation:

$$K(r,z) = Ae^{-Br}e^{-Bz} \qquad (2.18)$$

Isotropic point spread functions were assumed so that the exponential constant, B, is the same for axial as well as transaxial variations. Measurement of the parameters was made using point sources in water cylinders rather than line sources, as was done for 1D convolution PSF's. Shao observed that the 1D convolution using line sources predicts the same scatter fraction in all planes, causing an overestimate of scatter in planes containing radioactivity and an underestimate of scatter in activity free planes.

An accurate means of measuring 2D convolution PSF's was implemented by Bailey using measurements of line sources in air and within water cylinders (Bailey and Meikle, 1994). The scatter profiles could then be measured by performing a calculated attenuation on the source in air acquisition using the narrow beam attenuation correction factors for the water cylinder. The difference between the source in water profiles from the attenuated source in air profiles would then produce an accurate estimate of the scatter profiles. The scatter profiles were modelled using equation 2.18 where the PSF was assumed to be isotropic with the measured exponential decay constant in the radial direction assumed to be the same as the value for the axial direction.

The first attempt to characterize the variations of the point spread function on position within the object was made by Hoverath (Hoverath et al, 1993). Hoverath observed that point spread functions had different slopes on either side of the source projection bin when the source position was off center in a water cylinder. These slopes were parameterized using a number of measurements for several source positions. The position dependent PSF's were tested by estimating scatter profiles for water cylinders with a variety of source distributions using 2D iterative convolution subtraction in projection space. Projection space convolutions, according to equation 2.15, were permissible because of Hoverath's observation of little PSF variation as a source was moved to different positions along a particular line of response. This is no doubt the reason little improvement was observed by Barney when using image to projection methods as per equation 2.16 (Barney et al, 1993).

The first attempts to characterize point spread functions as something other than simple exponentials was made by Wienhard (Wienhard and Lercher, 1994). He observed the PSF's to have a Gaussian shape that could be described by the equation:

$$K(r,z) = Ae^{-4\ln 2[(\frac{r'-r+s}{FWHM_r})^2+(\frac{z'-z}{FWHM_z})^2]} \qquad (2.19)$$

where the four parameters of amplitude, A, Gaussian full width at half maximum in the radial and axial direction, $FWHM_r$ and $FWHM_z$, as well as shift, s, were measured using point sources at a variety of positions within a water cylinder. For off center sources, the shift parameter accounts for the observed shift of the scatter peaks towards the periphery of the object, outside of the source peaks (see figure 7). The shift parameter increases as the radial position of the source from the center of the cylinder increases. The Gaussian FWHM is observed to decrease as the lower energy discriminator setting increases since small angle scattering at higher energies are the only scatter accepted.

Attempts to modify the amplitude of scatter point spread functions using the attenuation correction factors of transmission scans has been attempted for SPECT (Meikle et al, 1994). The method scales the calculated scatter profiles, obtained using iterative convolution subtraction, by the scatter fraction for each LOR estimated using the attenuation correction factor (ACF) for that LOR. This means of direct scaling from the ACF's is physically sound only for SPECT systems where scatter is constrained to the object and is proportional to the ACF for each LOR. Extension of this method to PET where scatter is not constrained to the object must be done with care.

Other Scatter Correction Methods

Two additional scatter correction techniques have been proposed for PET which are neither of the convolution type nor the energy based type. The first method called the extraction of trues method uses a mixture of the energy based correction as well as the convolution correction assumptions. A second approach uses measurements with and without septa in place for retractable septa tomographs.

Extraction of Trues

The extraction of trues method (Bendriem et al, 1994) requires the acquisition of data in two energy windows to perform scatter correction. A low energy window (LEW) extending from 250-350 keV measures both scatter and unscattered counts while a high energy window (HEW) from 550-850 keV contains predominantly unscattered events observed at energies above 511 keV because of the energy resolution of the BGO detectors. The HEW contains a noisy estimate of the unscattered distribution having about 6% scatter that is removed using either a convolution subtraction or a deconvolution technique. To estimate the scatter distribution in the LEW, the scatter corrected noisy distribution in the HEW is scaled up by a factor to account for efficiency differences between the two windows. This estimate of the unscattered distribution in the LEW is first smoothed using some filter. The smoothing is considered permissible because of the smooth nature of the scatter profiles. The estimate of scatter in the LEW is simply the difference between the LEW and the scaled, smoothed and scatter corrected distribution in the HEW.

The two major problems with the technique are that Compton scatter at low angles, which have the highest probability according to the Klein-Nishina equation, may exist up to 511 keV and so have the same probability of being mis-registered by the BGO detectors into the HEW. This explains the 6% scatter still observed in the HEW which requires correction. The second problem is the large amount of noise in the HEW since the count rate in this window can be nine times less than that for the LEW. Large acquisition times are required to obtain sufficient statistics, but even so, smoothing of the unscattered projections is still required. The method has produced some respectable estimates for scatter when tested on flood phantoms with low activity regions enclosed.

Retractable Septa Scatter Correction

Another means of performing 3D scatter correction for PET systems with retractable inter-plane septa is to first acquire a short 2D acquisition before a longer 3D acquisition (Cherry et al, 1993). The idea is that the difference in counts registered in sequential acquisitions of the LOR's common to both data sets will be due to increased efficiency (septa no longer block some unscattered events) and to increased detection of scattered events. If one can correct for the efficiency differences then the remaining difference will be due solely to scattered events, producing an estimate of scatter according to the equation:

$$S(r,\theta) = T_{3D}(r,\theta) - \epsilon(r,\theta)\, T_{2D}(r,\theta) \qquad (2.20)$$

where $\epsilon(r,\theta)$ is the LOR dependent efficiency factor obtained by taking the ratio of scatter free blank scans which used a rotating rod source.

The 2D acquisition with septa still contains some scatter which were removed by assuming the 2D scatter distribution has the same shape as for 3D. The estimate of scatter (eqn 2.20) could then be scaled by an axial position dependent factor, obtained from measurements on phantoms. The scatter for oblique LOR's present in the 3D dataset but absent for 2D acquisitions were estimated by using corresponding direct plane LOR's from the 2D data set whose axial position was the same as the 3D LOR's mean axial position. Such an approximation is reasonable considering the small axial acceptance angle of PET.

The main difficulty for retractable septa scatter correction is the requirement that the isotope distribution be time independent since the distribution must not differ greatly from when the initial 2D acquisition was made. The need to retract septa for each study is also rather inconvenient or impossible for many PET systems.

CHAPTER III

Analytic Scatter Correction Theory

The filtering scatter correction techniques described in Chapter II require the expense of much effort to obtain measurements of scatter point spread functions for a variety of imaging conditions. However, little effort has been made to utilize the well established physics of Compton scattering to deduce these PSF's. In this chapter, a means of estimating the PSF's for iterative 3D convolution subtraction is explored using the Klein-Nishina differential cross section to describe the angular distribution of scattered annihilation photons. The attenuation correction factors (ACF's) from transmission scans are included within the theory as inputs describing the distribution of matter in the object being imaged. Such analytic PSF's are hopefully more accurate for realistic imaging conditions than the measured PSF's of water cylinders. Some knowledge of the important factors governing the shape of scatter point spread functions may also be revealed to improve the choice of approximations used in various scatter correction schemes.

Scatter Analysis using the Klein-Nishina Equation

The Klein-Nishina differential cross section (eqn 1.9) describes the Compton scattering of a 511 keV annihilation photon through an angle β into the solid angle dΩ. The total Compton cross section for scattering through any angle can be found by numerically integrating the equation over all angles to give:

$$\sigma_c = \frac{Zr_o^2}{2}\int_0^{2\pi}\int_{-\pi/2}^{\pi/2}\left(\frac{3-3\cos\phi\cos\theta+3\cos^2\phi\cos^2\theta-\cos^3\phi\cos^3\theta)}{(2-\cos\phi\cos\theta)^3}\right)\cos\theta\, d\theta\, d\phi \qquad (3.1)$$

where $\cos\beta=\cos\phi\cos\theta$ gives the scattering angle β as a result of 2 orthogonal angles ϕ,θ with ϕ being the angle within a ring and θ being the angle from the transaxial plane. $d\Omega=\cos\theta d\theta d\phi$ is the element of solid angle. Numerical integration gives σ_c = $7.22 \bullet Zr_o^2/2$ = 2.87×10^{-24} cm^2 for water (Z=10). Since $\mu_c=\sigma_c n_T$ with n_T being the density of target molecules, the Compton interaction coefficient is theoretically estimated to be:

$$\mu_c = \sigma_c n_T = \sigma_c \frac{N_A \rho_w}{A_w}$$

$$\mu_c = \frac{(2.87x10^{-24}cm^2)(6.02x10^{23}molecules/mole)(1g/cm^3)}{18.02g/mole} \qquad (3.2)$$

$$\mu_c = 0.0957cm^{-1}$$

where N_A is Avogadro's number, ρ_w is the density of water and A_w is the atomic weight of water. This value for μ_c agrees very closely with the accepted narrow beam attenuation coefficient for 511 keV photons in water of 0.096cm^{-1}.

Based on this, the attenuation correction factors (ACF's) calculated from the ratio of blank over transmission scans can be assumed to be completely a result of Compton scattering of photons from the narrow beam. The ACF can be represented by the equation:

$$ACF = \frac{1}{e^{-[\mu_c(\beta \neq 0^\circ) + \mu_{PE}]d}} \approx \frac{1}{e^{-\mu_c d}} \qquad (3.3)$$

where $\mu_c(\beta \neq 0^\circ)$ is the Compton cross-section for scattering outside of a broad beam diverging at an angle β and the approximation is for negligible photoelectric effect and narrow beam ACF's. The negligible contribution of the photoelectric effect in water (human soft tissue equivalent) is not surprising considering that σ_{PE} is only comparable to σ_c for detectors with large Z materials (see page 15). The photoelectric cross section's Z^5 dependence (eqn 1.6) relative to the linear dependence of the Compton cross section on Z (eqn 1.9) is responsible for σ_{PE} being negligible for typical scanning conditions involving low Z materials. Greater than 99% of the interactions experienced by 511 keV photons in water will be Compton scattering.

The close agreement of the theoretical Compton interaction coefficient with the experimental narrow beam attenuation coefficient indicates the predominance of Compton scatter in attenuation correction and suggests a strong link between the scatter correction problem and the attenuation correction problem. In fact, attenuation correction with narrow beam ACF's is really just scatter correction by accounting for the photons which "out-scatter" from their initial path (fig 8). Unlike attenuation correction, scatter correction should also consider "in-scatter" by accounting for the fact that scattered photons sometimes scatter into a different projection bin instead of being removed as is

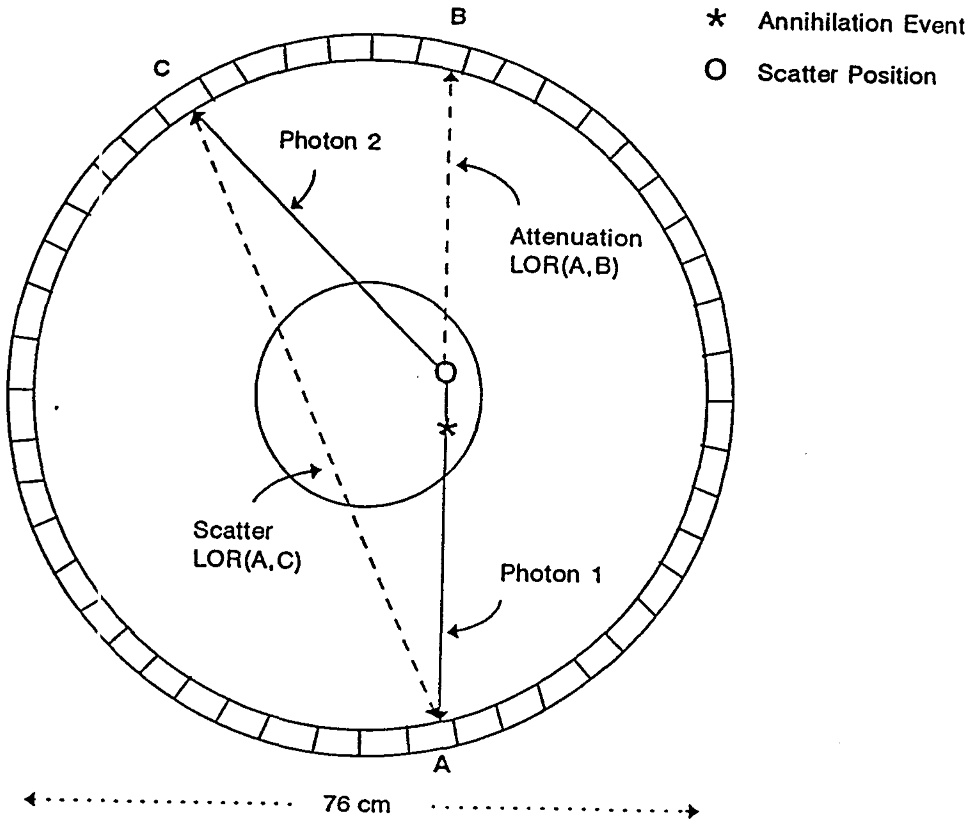

Figure 8: Comparison of attenuation and scatter correction. LOR(A,B) experiences attenuation as photon 2 fails to reach detector B. LOR(A,C) receives a scatter coincidence as photon 2 is received by detector C.

assumed by attenuation correction. These "in-scatters" must first be removed from the projection data through an accurate scatter correction technique before the projections are rescaled for "out-scatter" by the ACF's. Narrow beam ACF's are required for this purpose so that the "in-scatters" must be removed from the transmission scan as well as for the emission scan.

Scatter Amplitude

In order to predict the particular bins and projections (B,P) which scattered photons initially along a particular line of response (B_o,P_o) will scatter into, a single scatter approximation is adopted where only those scatter coincidences in which one of the annihilation photons single scatters are considered for in-scatter to (B,P). This can be visualized in the following figure:

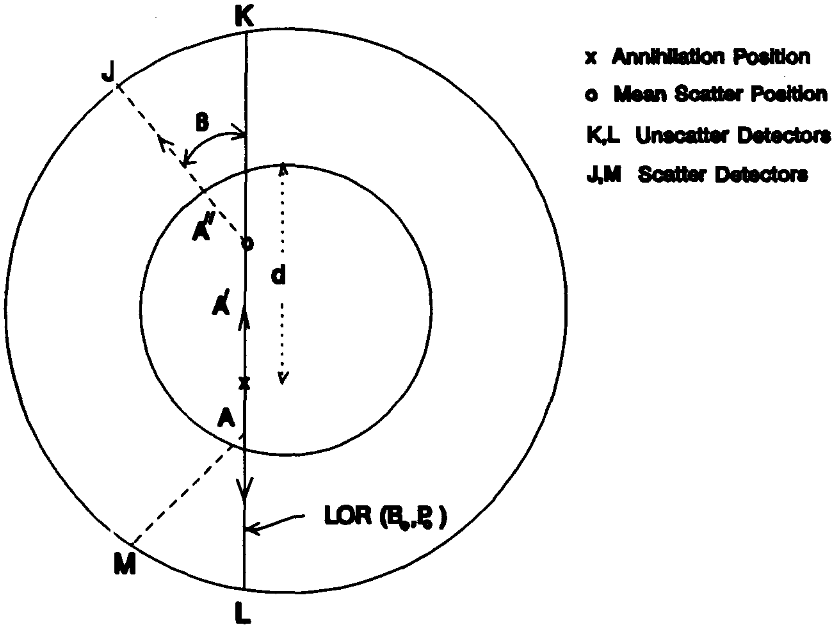

Figure 9: Description of scatter event.

where **x** indicates the annihilation position, **o** represents the location of scatter through an angle β and A, A′, A″ are the indicated escape routes of the 2 photons as they travel through the object for detection. A mean scatter position approximation is employed where scattering is only permitted to occur from a calculated mean scatter position (o) (see page 70). The probability of detecting a scattered photon at detector J from an annihilation whose photons initially travelled along LOR(B_o,P_o) is given by the equation:

$$P(J) = e^{-\mu A} e^{-\mu A'} e^{-\mu A''} (1 - e^{-\mu(\beta) d}) \qquad (3.4)$$

where the first three terms account for Compton scatter out of the indicated path (attenuation) and the fourth term is the probability of a Compton interaction through an angle β into the solid angle of detector J.

For $\beta = 0°$, the scatter which occurs within the same LOR, and hence the amplitude of the scatter point spread function, can be determined. In this case the first three terms combine into the term $e^{-\mu(A+A'+A'')}$ which is simply the inverse ACF through the LOR(B_o,P_o) or $[\mathrm{ACF}(B_o,P_o)]^{-1}$. The fourth term can be rewritten:

$$1 - e^{-\mu(\beta) d} = 1 - e^{-C(\beta) \mu d} \qquad (3.5)$$

where $C(\beta) = \mu(\beta)/\mu = \sigma(\beta)/\sigma$ is the ratio of the Compton cross section into the solid angle of detector K to the Compton cross section through all solid angles.

This function $C(\beta)$ can be evaluated using the value previously calculated by numerical integration for the K-N equation integrated over all solid angles to be $\sigma = 7.22 \bullet Z r_o^2/2$. The cross section for scatter through an angle β into the solid angle of a detector at a distance R from the scatter position (o) is given by:

$$\sigma(\beta) = \frac{d\sigma(\beta)}{d\Omega}\Omega_K = \frac{Zr_o^2}{2}\left(\frac{3-3\cos\beta+3\cos^2\beta-\cos^3\beta}{(2-\cos\beta)^3}\right)\left[\frac{A_D}{R^2}\right] \qquad (3.6)$$

where A_D is the area of a detector = (0.622cm•0.675cm) = 0.4197cm^2. This assumes a constant K-N cross section over the small solid angle of a detector. It also assumes that the response of the detector is not greatly affected by the angles of the incident photons (as for spherical detectors). F(β) is defined as the ratio of the K-N equation at an angle β over an angle of 0° given by:

$$F(\beta) = \frac{1}{2}\left(\frac{3-3\cos\beta+3\cos^2\beta-\cos^3\beta}{(2-\cos\beta)^3}\right) \qquad (3.7)$$

so that the function C(β) for a photon scattered through an angle β is:

$$C(\beta,R) = \frac{2\cdot F(\beta)\,A_D/R^2}{7.22} \qquad (3.8)$$

For β=0° and R=38cm (center of tomograph), C(0°,38)=8.0544x10^{-5}.

To determine the probability of a scatter through 0° of either photon as the sum of 2 separate cases, the probability P(0°) becomes:

$$\begin{aligned} P(0^\circ) &= P(K)+P(L) = ACF(B_o,P_o)^{-1}\left(1-e^{-C(0^\circ,R_K)\mu d}+1-e^{-C(0^\circ,R_L)\mu A}\right) \\ P(0^\circ) &\approx ACF(B_o,P_o)^{-1}\left[C(0^\circ,R_K)\mu d+C(0^\circ,R_L)\mu A\right] \end{aligned} \qquad (3.9)$$

using the approximation e^x=1+x for small x since $C\mu A \ll 1$ for all imaging conditions considering the sample C above. If an effective C(0°) is defined, weighted by the fractional mean free paths of A and d, we see:

$$C(0°) = C(0°, R_K)\frac{\mu d}{\mu A+\mu d} + C(0°, R_L)\frac{\mu A}{\mu A+\mu d} \qquad (3.10)$$

So substituting this C(0°) into equation 3.9 and once again using the small exponent approximation, the probability of 0° scatter becomes:

$$\begin{aligned} P(0°) &= ACF(B_o, P_o)^{-1}\,[C(0°)\,(\mu A+\mu d)] = ACF(B_o, P_o)^{-1}\,[1-e^{-C(0°)\,(\mu A+\mu d)}] \\ P(0°) &= ACF(B_o, P_o)^{-1}\,[1-(e^{-(\mu A+\mu d)})^{C(0°)}] \qquad (3.11) \\ P(0°) &= ACF(B_o, P_o)^{-1}\,[1-ACF(B_o, P_o)^{-C(0°)}] \end{aligned}$$

The number of photons initially travelling along LOR(B_o,P_o) is the number of true coincidence counts, T(B_o,P_o), in LOR(B_o,P_o) scaled up by the narrow beam scatter corrected ACF(B_o,P_o). The number of scatter counts in LOR(B_o,P_o) representing 0° scatter is thus:

$$\begin{aligned} S(0°) &= P(0°)\,ACF(B_o, P_o)\,T(B_o, P_o) \\ S(0°) &= [1-ACF(B_o, P_o)^{-C(0°)}]\,T(B_o, P_o) \end{aligned} \qquad (3.12)$$

where S(0°) is the amplitude of the scatter point spread function.

Scatter Profile

The shape of the scatter profile relative to the 0° scatter bin (B_o,P_o) can be determined using equation 3.4 which describes the probability of scatter into a detector J as:

$$\begin{aligned} P(J) &= e^{-\mu(A+A'+A'')}\,(1-e^{-\mu(\beta_J)d}) \\ P(J) &= e^{-\mu(A+A'+A'')}\,(C(\beta_J, R_J(\beta))\,\mu d) \end{aligned} \qquad (3.13)$$

using the small exponent approximation. The first term is no longer the inverse ACF of LOR(B_o,P_o) since the scattered photon travelling along A″ is no longer confined to the source LOR(B_o,P_o), however for the moment this will be assumed so and ACF$(B_o,P_o)^{-1}$ will be used to replace $e^{-u(A+A'+A'')}$. A suitable correction for this assumption involving the forward projection along A″ through an attenuation image to a mean scattering position (o) is discussed in greater detail in the analytic corrections section (page 78). Using equation 3.12, the scatter coincidences in P(J) will be:

$$\begin{aligned} S(J) &= [C(\beta_J, R_J(\beta))\,\mu d]\; T(B_o, P_o) \\ S(J) &= [F(\beta_J)\, R_J^2(0)/R_J^2(\beta_J) \cdot C(0^\circ, R_J(0))\,\mu d]\; T(B_o, P_o) \end{aligned} \qquad \mathbf{(3.14)}$$

when one examines the definition of C(β,R) in equation 3.8. Using the definition of C(0°) in equation 3.10 and the fact that equations 3.11 and 3.12 give S(0°) to be:

$$S(0^\circ) = [C(0^\circ)\,(\mu A + \mu d)]\; T(B_o, P_o) \qquad \mathbf{(3.15)}$$

The shape of the scatter profile into a detector J relative to 0° scatter is found to be:

$$\frac{S(J)}{S(0^\circ)} = \frac{\mu d}{\mu A + \mu d}\left[\frac{F(\beta_J)\, R_J^2(0)/R_J^2(\beta_J)}{\dfrac{\mu d}{\mu A + \mu d} + \dfrac{C(0^\circ, R_M(0))}{C(0^\circ, R_J(0))}\,\dfrac{\mu A}{\mu A + \mu d}}\right] \qquad \mathbf{(3.16)}$$

cancelling the (μA+μd) term and knowing that $C(0^\circ,R_M(0))/C(0^\circ,R_J(0)) = R_J^2(0^\circ)/R_M^2(0^\circ)$, the scatter profile simplifies to:

$$\frac{S(J)}{S(0^\circ)} = \frac{\mu d}{\mu d + [R_J^2(0)/R_M^2(0)]\,\mu A}\, R_J^2(0)/R_J^2(\beta_J) \cdot F(\beta_J) \qquad \mathbf{(3.17)}$$

Similarly, scatter of the photon travelling initially towards detector L in the diagram gives the scatter profile:

$$\frac{S(M)}{S(0^\circ)} = \frac{\mu A}{\mu A + [R_M^2(0)/R_J^2(0)]\,\mu d} R_M^2(0)/R_M^2(\beta_M) \cdot F(\beta_M) \qquad \textbf{(3.18)}$$

The above scatter profile equations reveal the predominant physics responsible for determining the shape of the scatter profile. The most important term in the above equations, which is largely responsible for determining the shape of the profiles, is the Klein-Nishina term, F(β), whose tendency towards forward scattering governs the overall shape. The other term, which slightly modifies the shape, is the $R^2(\beta)$ term since the distance from the mean scatter position to the detector which accepts the scattered photon affects the solid angle of the detector for the scattered photon and hence its chances of being detected. The remaining terms are angle independent however the first ratio is approximately $\mu d/(\mu d+\mu A)$ so that the mean free path fraction is largely responsible for determining which of the 2 photons will be single scattered. There are two other factors affecting the shape of the analytic PSF's which are described in more detail in the analytic corrections section below. The first involves correcting for the different attenuation along escape paths of scattered photons compared to along the escape paths of unscattered photons. Secondly, not all single scattered photons are recorded above the energy threshold setting of the tomograph and so correction for the discrimination of large angle, low energy photons must be performed.

Mean Scatter Position

To use the scatter profiles described in equations 3.17 and 3.18, the detector to mean scatter position constants (R_J and R_M) must first be evaluated, which implies the need to calculate the mean scatter position. For simplicity, it is assumed that all scatter for a photon travelling in a particular LOR occurs at the mean scatter position. The method proposed for doing this requires the creation of an attenuation image as well as an attenuation corrected emission image. The images need only be 2D reconstructed images and since only ratios of forward projected lines through the images will be used, the absolute pixel values are unimportant. Although the prospect of creating 2D images and forward projecting through them sounds time consuming at first glance, this may not be so when considering the typical 3D reconstruction times which are currently observed.

To obtain the mean scatter positions along the LOR(B_o,P_o) for both scatter into J and into M (y_J and y_M), forward projection along LOR(B_o,P_o) through the attenuation image is performed to give a value of A_{tot}. A similar line integral through the emission image is also done to normalize the source strength to S_{tot}. To obtain the mean free path fractions, a line integral beginning at detector L through the attenuation image is described as follows:

$$\frac{\mu A}{\mu A+\mu A'} = \sum_{i\,LORpix} \frac{(S_i \Delta y_i)}{S_{tot}} \frac{A_{tot\,i}}{A_{tot}} \qquad (3.19)$$

where S_i is the pixel value of pixel i and Δy_i is the length of the LOR through i. $A_{tot\,i}$ is the summed attenuation along LOR(B_o,P_o) up to pixel i. Similarly:

$$\frac{\mu d}{\mu A+\mu d} = 1-\frac{\mu A}{\mu A+\mu d} \qquad (3.20)$$

Since the scatter photon has an equal probability of scattering at any position along the escaping photons mean free path, the mean scatter position will be half of the escape mean free path, or $\mu d/2$ for scatter into detector J and $\mu A/2$ for scatter into detector M.

To obtain the actual position in cm for the mean scatter position, the following technique might be used. For each pixel i representing the location of a point source, integration back along the attenuation image LOR(B_o,P_o) from pixel i by an amount [$A_{tot\,i}/2$] is done until a distance $y=\Sigma\Delta y_i$ is found so that the mean position along the LOR for scatter into detector M will be $y_s \equiv y_i - y$. This position, y_s, represents the mean scatter position into detector M for a point source located at pixel i. Such a mean scatter position would be used for defining the point spread function for image to projection techniques described in Chapter II (see page 51). For projection space convolution subtraction, the mean scatter position must be weighted by the source strength for all pixels in the line of response according to the following equation:

$$y_M = \sum_{i\,LORpix} \frac{(S_i \Delta y_i)}{S_{tot}} \frac{A_{toti}}{A_{tot}} y_s \,/\, [\frac{\mu A}{\mu A+\mu d}] \qquad \textbf{(3.21)}$$

The mean position of scatter into detector J is similarly:

$$y_J = \sum_{i\,LORpix} \frac{(S_i \Delta y_i)}{S_{tot}} \frac{(A_{tot}-A_{toti})}{A_{tot}} y_s \,/\, [\frac{\mu d}{\mu A+\mu d}] \qquad \textbf{(3.22)}$$

except in this case, $y_s \equiv y_i + y$, as may be understood from figure 9. In each case, $y \equiv 0$ is located in the center of the LOR. These values of y_M and y_J can be used to calculate the detector to mean scatter position distances R_M and R_J.

Application of Technique to Sinograms

To apply the analytic scatter correction technique to sinogram data, a means of re-evaluating the scatter profile equations (eqns 3.17 and 3.18) in terms of bins and projection angles must be found. To achieve this, the distances $R_M^2(\beta_M)$ and $R_J^2(\beta_J)$ must first be calculated given a source bin, B_o, and a scatter bin, B, where detector J or M exists. This is attempted with the assistance of figure 10:

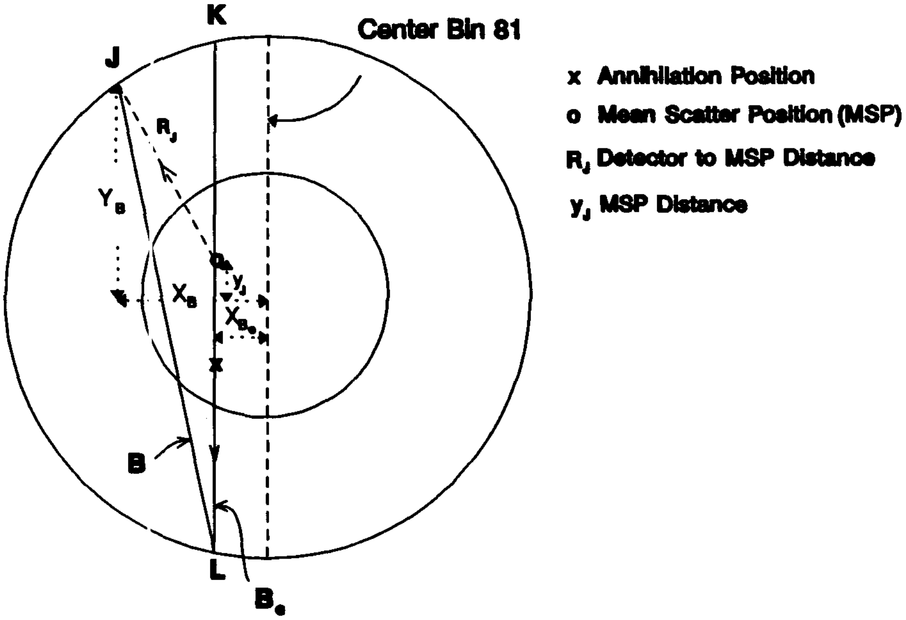

Figure 10: Scatter bin calculation.

where B_0 is the source bin, B is the scatter bin, and x_{B_0} and x_B are the perpendicular distances from the center bin (bin 81). The distance, R_J, from the scatter position (o) to the scatter detector (J) is:

$$R_J^2 = (x_B - x_{B_o})^2 + (y_B - y_J)^2 \qquad (3.23)$$

where y_J is the position along LOR(B_o,P_o) calculated to be the mean scatter position for detector J. Since there are 384 detectors per ring and the radius of the tomograph is

38cm, x_B, y_B and x_{B_o} are calculated to be:

$$\begin{aligned} x_B &= 38\,SIN\left(\frac{\pi(B-81+0.5(81-B_o))}{192}\right) \\ y_B &= 38\,COS\left(\frac{\pi(B-81+0.5(81-B_o))}{192}\right) \\ x_{B_o} &= 38\,SIN\left(\frac{\pi(B_o-81)}{384}\right) \end{aligned} \tag{3.24}$$

where $\pi/192$ is the angle in radians between adjacent detectors in a ring when viewed from the center of the FOV (bin 81). The equation for R_M^2 is similar to equation 3.23 except y_M replaces y_J, and y_M must be negated (likely to a positive value) since the cosine term is positive for scatter by either photon.

The values of $R^2(\beta)$ can now be calculated for any detector (J or M) for substitution into equations 3.17 and 3.18 to obtain the scatter profile shapes. For the first term of these equations involving the fractional mean free path for the escape of each photon from the object, unless the assumption is made that $R_M^2(0) \approx R_J^2(0)$, these fractions would have to be re-evaluated. This would be accomplished by using the newly calculated values of R_M and R_J, and a further line integral through the attenuation image. Such an assumption would require testing for non-symmetric source and object density distributions before use and is desirable since the simplification would economize computation time.

The last portion of the scatter profiles to be evaluated is the K-N function $F(\beta)$ for any source bin B_o and scatter bin B. This can be evaluated with the aid of figure 10, and the calculation of R for any (B_o,B) combination. The scatter angle β_J is computed as:

$$\beta_J = SIN^{-1}\left(\frac{x_B - x_{B_o}}{R_J}\right) \tag{3.25}$$

where x_B, x_{B_o} and R_J are calculated in equations 3.23 and 3.24. β_M is calculated in a similar way with y_M replacing y_J. The scatter profiles S(J)/S(0°) and S(M)/S(0°) can now be rewritten in the form $S(B)/S(B_o)$ for any source bin B_o and scatter bin B.

The projection which the scattered photon will "in-scatter" to is determined from knowledge of the sinogram construction (page 20). The source $LOR(B_o,P_o)$ scatters into LOR(B,P), where the probability of scattering into bin B is calculated using equations 3.17, 3.18 and 3.25. The scatter projection is governed by the following mappings, where case #1 exists when the top detector in the LOR of figure 10 has $J \epsilon (1,192)$ while case #2 occurs when $J \epsilon (193,384)$. The results are:

CASE #1: $J\epsilon(1,192)$

$B > B_o$: (B_o,P_o) => $(B , P + (B-B_o)/2 + PARITY(B_o))$
$B < B_o$: (B_o,P_o) => $(B , P - (B_o-B)/2 - PARITY(B_o+1))$

CASE #2: $J\epsilon(193,384)$ (3.26)

$B > B_o$: (B_o,P_o) => $(B , P - (B-B_o)/2 - PARITY(B_o+1))$
$B < B_o$: (B_o,P_o) => $(B , P + (B_o-B)/2 + PARITY(B_o))$

where the PARITY function is defined as being 1 for odd B_o and 0 for even B_o. The $(B-B_o)/2$ terms truncate the decimal place. The scatter counts occurring in LOR(B,P) as a result of the true unscattered count rate in the source $LOR(B_o,P_o)$ can thus be evaluated from the above equations.

Inter-Plane Scatter

In the previous sections, discussion of scatter has been restricted to scatter within the same plane (sinogram) for coincidences within the same ring. The analytic PSF theory must be extended to include scatter into other sinograms in the 3D data set not including the source. To scatter into non-source 3D projections, the photon must scatter through an angle ϕ_B, into a bin B of a sinogram, as well as through an orthogonal angle θ_{sl}, indicating the angle between 2 sinogram planes (see fig 4 on page 19). This angle θ_{sl} is calculated to be:

$$\theta_{sl}(B,B_o) = TAN^{-1}\left\{\frac{0.675\,\Delta SL}{R(B,B_o)}\right\} \tag{3.27}$$

where 0.675cm is the detector length in the axial direction, $R(B,B_o)$ is the distance from the mean scatter position to the scatter detector in bin B (eqn 3.23), and ΔSL is the slice offset between the sinogram containing the source $LOR(B_o,P_o)$ and the sinogram which the photon is scattered into given by:

$$\Delta SL = ABS\{K(SRC) + L(SRC) - K(SCAT) - L(SCAT)\} \tag{3.28}$$

K(SRC) and L(SRC) are the ring numbers (1 through 16) of the source $LOR(B_o,P_o)$, while K(SCAT) and L(SCAT) are the ring numbers of the scatter LOR(B,P). Scatter into any sinogram can thus be calculated by allowing $COS\beta$ in the K-N term, $F(\beta)$, given by equation 3.7, to be replaced by $COS\phi_B COS\theta_{SL}$ where ϕ_B is defined as β_J which was evaluated in equation 3.25. The K-N term can thus be re-written as:

$$F(\phi_B,\theta_{SL}) = \frac{1}{2}\left(\frac{3-3\cos\phi_B\cos\theta_{SL}+3\cos^2\phi_B\cos^2\theta_{SL}-\cos^3\phi_B\cos^3\theta_{SL}}{(2-\cos\phi_B\cos\theta_{SL})^3}\right) \quad (3.29)$$

For the single scatter approximation, each photon can only produce scatter in 16 of the 256 3D sinograms since the unscattered photon remains in the source ring so that for scatter to detector J, K(SCAT)=K(SRC) and scatter of the other photon to detector M causes L(SCAT)=L(SRC). Therefore, 32 sinograms must have their scatter profiles calculated for each source line of response in the 3D dataset.

To obtain the total scatter profile resulting from all source lines of response, the simplifying assumption introduced by Bailey for convolution subtraction proves useful (page 52). The assumption is that scatter distributions do not vary greatly with the angle of the sinogram plane from the axis of the tomograph and depend only on the mean axial position of the sinogram plane, z. For this reason, the 256 3D sinograms may be reformatted into the 31 axial slices characteristic of a 2D dataset. The scatter distributions need only be calculated for 31 axial slices using these 31 source planes since the scatter profiles in the 256 3D sinograms can be obtained by comparison with the slice at the axial position equivalent to its mean axial position. Each photon in each line of response produces scatter in all 31 axial scatter slices which are calculated as formulated in the previous section. Any scatter coincidences caused by radioactivity outside the axial field of view fails to be considered by this method since such decays never produce true unscattered counts within the dataset.

Analytic Corrections

Two additional corrections to the scatter profiles indicated in equations 3.17 and 3.18 are required. A first correction to account for energy discrimination of single scattered photons recorded below the tomograph's discrimination energy threshold is needed since the analytic theory assumes all single scattered photons striking detectors are recorded. A second correction is required to account for the difference in attenuation experienced by scattered photons along their escape path relative to that of unscattered photons.

Energy Discrimination Correction

Scattered photons exist at energies below the 511 keV photopeak energy as described by the Compton equation (eqn 1.9) to be:

$$E = \frac{511}{2 - \cos\phi_B \cos\theta_{SL}} \tag{3.30}$$

Photons scattered at larger angles will be shifted to lower energies and so will experience a greater probability of being recorded below the energy discrimination setting, E_o, of the tomograph. The BGO detectors record energy spectra as a Gaussian shape for mono-energetic photons where the FWHM of the Gaussian curve defines the energy resolution of the detectors and is represented as a certain percentage, R, of the photopeak energy (see page 16). The spread of a Gaussian function is normally described by its standard deviation, σ, where the calculation of σ is given by the equation:

$$\sigma = \left(\frac{R}{100}\right)\left(\frac{E}{2.34}\right) = \frac{R \cdot E}{234} \qquad (3.31)$$

since a FWHM is 2.34 standard deviations wide.

To calculate the probability of a photon being recorded above the discrimination energy, E_o, the statistical t value of the photon energy relative to E_o is required as follows:

$$t = \frac{E - E_o}{\sigma} \qquad (3.32)$$

The probability of this t value producing a recorded energy above E_o is calculated with the help of the error function, erf(x), whose series expansion is given as:

$$erf(x) = \frac{2}{\sqrt{\pi}}\left(x - x^3/3 + \frac{1}{2!}x^5/5 - \frac{1}{3!}x^7/7 + \ldots\right) \qquad (3.33)$$

where $x \equiv \sqrt{2}\, t$ and the function gives the area under a normalized Gaussian curve from the origin to t (Weast, 1989). The probability of detecting a photon of energy, E, for a tomograph with an energy discrimination setting of E_o thus becomes:

$$P(t) = 0.5 + erf(\sqrt{2}\, t) \qquad (3.34)$$

The series expansion used (equation 33) contained terms up to the 23rd power at which point the function was observed to be sufficiently close to erf(x) over the range of energies found in PET. The probability calculated in equation 3.34 modifies the scatter profile equations (3.17 and 3.18) simply by pre-multiplying these equations as an extra term.

Escape Path Length Attenuation

Another correction is required to correct for the assumption used in equation 3.14 that scattered photons experience the same attenuation along their escape paths as would have occurred had the photons remained unscattered. A means of correcting for this might be to forward project through the attenuation image from the scatter detector, J, to the mean scatter position (o) for each scatter detector. The correction for attenuation difference could then be calculated as:

$$ESC(J) = \frac{e^{-\mu J}}{e^{-\mu K}} = e^{-(\mu J - \mu K)} \qquad (3.35)$$

where μJ is the line integral from the mean scatter position (o) to J, and μK is the line integral from (o) to K, the unscattered detector.

The above procedure is somewhat slow as line integrals for 160 detectors would have to be calculated. The line integrals to out-of-plane detectors could safely be assumed to be equivalent to those calculated for the source plane since the relatively restricted axial field of view of the tomograph does not allow for significant variation along paths with different axial components.

The approximation of a mean scatter position suffers most for the escape path length attenuation correction since the assumption that all scatter events occur at the mean scatter position might produce greatly different line integrals to the scatter detector than had the photon been allowed to scatter at any position along the LOR. This assumption could be improved by averaging a series of line integrals to each scatter detector at various positions along the LOR, weighted by the attenuation coefficient for each pixel on the LOR. However, such an integral escape path length attenuation correction scheme would likely be rather time consuming. The assumption of a mean scatter position is tested in Chapter V in the section on non-uniform attenuation objects.

Summary of Analytic Scatter Correction

A recap of the protocol for performing analytic scatter correction is provided below for the general case of a non-uniform source distribution within a non-uniform attenuation medium. The technique's function is illustrated through its application to two simple test cases: a positron point source in the center of, and off-center in a uniform water-filled cylinder. These test cases are used in Chapter V to verify the accuracy of the technique when compared with experimental and Monte Carlo simulation data.

Protocol for Performing Scatter Correction

To perform analytic scatter correction, a 3D emission scan must be acquired within some suitable energy range and then normalized for detector efficiency differences according to the method described on page 28. To minimize the size of the data set required for scatter estimation, Bailey's assumption, concerning the minimal variation of scatter distributions with the angle of the sinogram plane from the axis of the tomograph (page 52), is adopted (Bailey and Meikle, 1994). This is accomplished by summing all sinogram planes with the same mean axial position, z, to produce the 31 axial slice sinograms characteristic of a 2D data set. To preserve the correct number of counts per sinogram, each of the 31 sinograms is divided by the number of 3D sinograms summed to construct it.

An additional simplification to further reduce the size of the data set within each sinogram can be made by summing the 160 projection bins and the 192 projection angles into a course grid sinogram of only 40 bins and 48 projection angles. The use of a course grid sinogram as employed by Wienhard (Wienhard and Lercher, 1994) is permissible considering the broad profiles exhibited by scattered photons. Collapsing the 3D data set according to the assumptions of Bailey and Wienhard reduces the data set size by a factor of 132, decreasing the convolution time required for scatter profile computation by a ratio of 528.

Scatter estimation proceeds by looping over all bins in the reduced data set and, at each step in the loop, calculating the quantity of scatter in all other affected bins resulting from this source bin. The scatter amplitude, $S(0^\circ)$, for the source bin is first calculated according to equation 3.12. $T(B_o,P_o)$ is the number of counts in the source bin after random, dead time and detector efficiency corrections have been made. $ACF(B_o,P_o)$ is determined from the ratio of counts in a blank and a transmission scan for the source bin. $C(0^\circ)$ is calculated using equation 3.10, where the parameters of this equation are determined from the evaluation of the mean scatter position outlined on pages 70-72. Consideration of multiple scatter events may be made by scaling the single scatter amplitude, $S(0^\circ)$, by some appropriate factor. This problem is further discussed in Chapter V on page 110.

The scatter is computed for the 40 reduced data set bins in each of the 31 planes which may receive scatter from photons initially travelling in the source bin LOR. The magnitude of the scatter in bin B resulting from the source bin, B_o, is computed using the scatter profile equations, 3.17 and 3.18, which describe scatter for each photon.

Corrections for energy discrimination and for differences in attenuation experienced by scattered photons escaping the object are applied at this stage by pre-multiplying the scatter profile equations according to the factors calculated in the respective sections (page 78 and page 80). The projection angle of each bin receiving the scattered photon is calculated using equation 3.26. Either photon may scatter so that 40 different bins in each of the 31 planes must have their scatter magnitude computed using a separate loop for each photon of each line of response.

After cycling through each bin in this way, an estimate of the scatter profile for the reduced data set has been achieved. Since the value of the true unscattered counts, $T(B_o,P_o)$, used to calculate the scatter amplitude is unknown, iterative scatter subtraction according to equation 2.15 may be employed. This is done by using the scatter profile calculated from the first convolution loop to correct the measured data set for use in a second convolution loop. If the theory used to derive scatter profiles is sound, only one or two such iterations may be required.

Finally, the reduced data set estimate of the scatter profiles must be re-expanded to estimate scatter in the 3D data set having 256 sinograms. Each of 31 scatter sinograms act as estimates of scatter for 3D sinograms having the same mean axial position. Individual sinograms may be re-expanded using interpolation between the course grid points of the reduced data set. Scatter correction is implemented simply by subtracting these scatter profiles from the measured data set. Attenuation correction and image reconstruction may then be performed following scatter correction.

Application of Technique to Two Test Cases

To test the validity of analytic scatter correction, and to illustrate its function, the technique is applied to the case of a point source located in the middle of a water-filled cylinder, centered in the field of view of the tomograph, as well as to the case of a point source located off-center in the transaxial direction. For the centered point source, an angular symmetry exists within each plane so that sinograms may be individually summed over all 192 projection angles to produce a single profile of 160 bins for each sinogram. This symmetry greatly simplifies the calculation of scatter profiles since one need only calculate a single, 160 bin, scatter profile to represent all 192 projection angles.

The scatter amplitude given by equation 3.12 reduces to:

$$S(81) = \{1 - [e^{0.0957d}]^{-C(0^\circ)}\}T \tag{3.36}$$

where d is the diameter, in centimeters, of the water filled cylinder, T is the number of true counts in the sinogram and C(0°) is calculated according to the equation:

$$C(0^\circ) = 8.0544x10^{-5}\left[\frac{38^2}{(38-d/4)^2}\right] \tag{3.37}$$

when one considers equations 3.8 and 3.10, as well as the fact that the mean scatter position is d/4, giving the distance from the mean scatter position to the unscattered photon detector as (38 - d/4) cm.

The scatter profile (equations 3.17 and 3.18) are identical in this situation so that their summation produces the scatter profile equation:

$$\frac{S(B)}{S(81)} = \frac{(38-d/4)^2}{R^2(B)} F(B)\, ESC(B)\, P(B,E_o) \qquad \textbf{(3.38)}$$

The detector to mean scatter position value, R(B), is calculated using equation 3.23 to be:

$$R(B) = 38\{SIN^2(\frac{\pi(B-81)}{192}) + [COS(\frac{\pi(B-81)}{192}) - 0.25d/38]^2\}^{1/2} \qquad \textbf{(3.39)}$$

The Klein-Nishina term, F(B), is calculated using equation 3.29, where the transaxial and axial angles, ϕ_B and ϑ_{SL}, are calculated using equations 3.25 and 3.27 respectively. The escape path length attenuation correction term, ESC(B), is determined using equation 3.35 to give:

$$ESC(B) = \frac{e^{-0.0957 R_{BSC}(B)}}{e^{-0.0957 \cdot d/4}} \qquad \textbf{(3.40)}$$

where the distance from the mean scatter position to the edge of the cylinder along the path of the scattered photon, $R_{BSC}(B)$, is computed through a numerical technique. Finally, the energy discrimination term, $P(B,E_o)$, is calculated using equation 3.34 according to the technique described in the energy discrimination correction section on pages 78-79. The above scatter profiles can be evaluated for cylinders of any diameter and for any of the 31 axial sinograms, through the use of the slice offset parameter, Δsl, given by equation 3.28. Each profile may be evaluated through the use of a single loop over all 160 bins.

For the case of the point source positioned off-center in the transaxial direction, calculation of the projection whose lines of response are perpendicular to the radial displacement direction of the point source can be achieved in a similar manner but with somewhat greater effort. The angular symmetry offered by the centered point source is no longer available, necessitating the calculation of the mean scatter position for each projection angle. The ACF used to estimate the scatter amplitude at each projection angle is calculated using the object chord length for the line of response passing through the point source position. Calculation of the energy discrimination term, the escaping photon attenuation term, the Klein-Nishina term and the detector to mean scatter position term of the scatter profile equations (eqns 3.17 and 3.18) is accomplished using methods similar to those described for the centered point source. The scatter profiles can be evaluated for any diameter cylinder for any source displacement distance with any energy discrimination setting of interest. The accuracy of the profiles generated by the analytic scatter correction theory is revealed through comparison with experimental and Monte Carlo scatter profiles in Chapter V.

CHAPTER IV

Monte Carlo Simulation

Since it is impossible to distinguish scattered coincidences from unscattered coincidences in actual experiments, estimation of scatter profiles for testing scatter correction techniques must be made using Monte Carlo simulation. In Monte Carlo simulation, photon histories are traced from the annihilation event location, through the object, to the detector array. The scatter history of each photon, as well as the energy deposited in each detector, are recorded so that profiles of scattered events may be separated from those of unscattered events. The principles of the Monte Carlo simulation used in this work are described in the following section. To verify the accuracy of the simulation, experimental measurements involving point sources of positron isotopes centered in water filled cylinders are compared with results obtained from Monte Carlo simulation.

Description of Monte Carlo Simulation

The development of the *Geant* Monte Carlo simulation program (Geant User's Guide, 1992), used in this work, was first begun in 1974 as a bare framework which initially emphasized tracking of a few particles per event through relatively simple detectors. *Geant* evolved over the years through the efforts of several hundred man-years of development; however the responsibility for its upgrade now rests with members of CERN laboratory. The program was initially developed to track the types of particles found in high energy physics, however its modification for use in PET was accomplished by C. Michel and others at CERN in the late 1980's (Michel et al, 1991).

The *Geant* program modified for use in PET consists of three distinct stages: geometry definition; photon tracking and data extraction. Each stage utilizes a different fortran program to perform its function. An overview of each stage is provided in the following sections.

Geometry Definition

The geometry definition stage requires the creation and positioning of mathematical shapes representing BGO detectors, tungsten septa, lead shielding and the object or phantom being scanned (see fig 2 on page 14). A variety of mathematical shapes are available to accomplish this including boxes, cones, cylinders, tubes, spheres and several other polygonal shapes. Definition of the geometry is accomplished by positioning and orienting "daughter" shapes within larger "mother" shapes according to the mother coordinate system where each shape possesses a code identifying the type of material within it. The material type may either be an element or compound where all cross-sections for all relevant physical processes are contained within the material code. The material code for the daughter shape supersedes the material code for the larger mother shape in the region within the mother shape where the daughter shape exists. As many as 15 "generations" of "grand-daughter" shapes may be placed within "daughter" shapes so that a "geometry tree" evolves where each subsequent generation of shapes provides greater detail for the device being described.

In the case of describing the tomograph geometry, the mother shape is defined as a large cylinder containing a vacuum inside of which a number of tubes, boxes and cylinders with material types of BGO, tungsten, lead, water and plexiglass are placed to describe the BGO detectors, septa, lead shield and object phantom. The "geometry tree" style of defining the tomograph structure is useful since the 96 BGO blocks, each containing 64 crystal elements, need only be defined once, and the structure can be positioned and oriented in the mother shape as many times as is needed.

The description of the geometry of the ECAT-953 PET scanner by the *Geant* Monte Carlo geometry definition package is complete save one simplification (Michel et al, 1991). In PET, the BGO blocks are sliced into an 8 x 8 crystal detector matrix with variable length slots (see fig 2(b) on page 14) to enhance crystal identification through a better light distribution scheme. However, in Monte Carlo simulation, the energy deposited in each crystal is directly recorded without simulating the scintillation photon collection process so that the added complexity of describing variable depth grooves is unnecessary. The BGO block slots in Monte Carlo simulation are considered to have the full radial depth (3 cm) thus slicing completely through the block. The volume of these slots does affect the detector packing fraction however, causing the theoretical packing fraction to be slightly lower than the real one.

In practice, all that is required to create a PET geometry unique to a particular experiment is to define the shape and material type of the object within the scanner. Construction of the scanner geometry either with or without interplane tungsten septa is performed automatically as requested.

Photon Tracking

The first step of the photon tracking stage is to define the positron isotope distribution to be simulated. This may be any distribution that can be described by a mathematical equation. From this distribution, a positron emission position is randomly selected and two back to back (180° apart), 511 keV photons are emitted in a random direction constrained within some stratification angle of the in-plane, trans-axial direction. This restricted solid angle of release eliminates simulation of photons initially travelling along the axial direction beyond the scanner detector rings thus having little chance of detection. A stratification angle of 30° has been reported to produce stable results (Michel et al, 1991). This is reasonable considering the axial acceptance angle of the ECAT-953 detector rings is ±8.1° from the center of the field of view. The choice of a 30° stratification angle limits the solid angle possible for photon release to 50 % of 4π hence doubling the effective activity concentration. Two approximations regarding annihilation photon release are used to simplify Monte Carlo simulation. First, the positron range is neglected and second, the photons are assumed to be perfectly collinear travelling at 180° from each other. These assumptions are tested in the Monte Carlo verification section on page 99.

Having released two annihilation photons, tracking of the photons through the materials defined in the geometry definition program must be accomplished. The *Geant* program does this using cross sections for the photoelectric effect, as well as for Compton and Rayleigh scattering, determined from fits to experimental data measured over a range of energies and Z values (material nuclear charges). The angle of Compton scattering is determined by sampling the Klein-Nishina differential cross section (eqn 1.7), while the scattered photon energy is calculated using the scattering angle (eqn 1.8). The electrons ejected during the photoelectric effect and Compton scattering are also tracked to ensure an accurate measurement of energy deposition in the BGO detectors. Charged particles passing through matter undergo countless collisions with atomic electrons (page 8) so that electron transport is a continuous rather than a discrete process. It is governed by the energy loss stopping power, dE/dx, determined from fits to experimental data measured over a variety of energies and material nuclear charges.

Geant tracks photons by moving them in steps of size Δs. The probability of a photon traversing this distance without undergoing a particular discrete interaction, the photoelectric effect for instance, is given by the survival probability:

$$P_{PE}(\Delta s) = e^{-\mu_{PE}\Delta s} \tag{4.1}$$

where μ_{PE} is the photoelectric effect interaction coefficient given by the equation:

$$\mu_{PE} = \left(\frac{N_A\rho}{A}\right)\sigma_{PE} \tag{4.2}$$

with N_A being Avogadro's number, ρ and A being the material's density and atomic mass, and σ_{PE} being the photoelectric cross section for the material being traversed. Photon tracking works by first selecting randomly the number of interaction lengths, N_λ, that a particle is going to travel before undergoing each of the three interactions it may be subject to. These three interaction lengths are selected according to the equation:

$$\begin{aligned} N_\lambda(PE) &= -\ln[R_1] \\ N_\lambda(Compton) &= -\ln[R_2] \\ N_\lambda(Rayleigh) &= -\ln[R_3] \end{aligned} \tag{4.3}$$

where R_1, R_2 and R_3 are random numbers distributed equally between zero and one. The corresponding step sizes for each interaction to occur are calculated using equation 4.1 to be:

$$\begin{aligned} \Delta s(PE) &= R_1/\mu_{PE} \\ \Delta s(Compton) &= R_2/\mu_C \\ \Delta s(Rayleigh) &= R_3/\mu_R \end{aligned} \tag{4.4}$$

The minimum step size of the above three is selected, the photon is transported this distance and the interaction selected is forced to occur. The photons position, energy and direction is updated after each step according to the interaction occurring. If the photon energy changes or a new material is entered, μ is re-calculated using the σ, ρ and A of the new material at the new photon energy. If a new material is entered before either of the three interactions occurs, the photon is transported to the boundary and the interaction lengths remaining, N_λ, are recalculated for the new material. The photon tracking process continues until a terminating photoelectric effect interaction occurs, until the photon energy drops below some cutoff energy, typically 50 keV, or until the photon exits the "mother" geometry. A photon falling below the cutoff energy has its energy deposited in the material at the position where this occurs.

After each annihilation photon has been tracked until termination, three types of information are recorded in a "dump" file. First, the detectors in which energy was deposited are recorded using numbers between 1 - 6144 to represent each of the 384 detectors in each of the 16 detector rings. Next, the exact energy in keV that is deposited in each of the indicated detectors is recorded and finally, a "Compton number" indicating the scattering history of the two photons is recorded. The Compton number, CN, is calculated using the equation:

$$CN = [Septa]*100 + [Object]*10 + [Detector] \tag{4.5}$$

where the values in brackets indicate the number of Compton interactions by either photon inside of the septa, object and detectors respectively. For instance, a Compton number of 123 indicates one scatter event in septa, two in the object and three in the BGO detectors. The photon history is thus recorded for the pair of annihilation photons rather than each individually. The simulation continues by tracking as many photon pairs as are requested until sufficient statistics are achieved. Typically, as many as 10 million annihilation events can be simulated in a 10 hour period (overnight) on a SPARC 10 Sun workstation.

Data Extraction

The data extraction program is the final, analysis stage of the Monte Carlo simulation where the specific information sought can be calculated. The program functions by first reading the "dump" file from the tracking program, which contains an entry for each annihilation event where energy was deposited in at least one detector. The data is then organized into sinogram format (page 20) which may be grouped for coincidences between any of the 16 detector rings desired. Sinograms may be constructed for detected events within any particular energy range requested. The exact energy recorded for each detector in the dump file may be blurred using a Gaussian distribution with a FWHM equal to some percentage of the recorded energy in order to simulate the energy resolution of the BGO detectors. Typically a 25 % FWHM Gaussian function is used to blur the recorded detector energies.

Using the recorded energies, Compton numbers and projection data formed into sinograms, energy spectra information or projection data specific to photons having a particular scattering history can be calculated. This allows for separation of scattered from unscattered events. Dead time and random coincidence difficulties are not demonstrated by Monte Carlo simulation since photons are tracked sequentially with no chance of interference effects occurring between separate annihilation events. This corresponds to the case of very low activity sources in the PET scanner.

Verification of Monte Carlo Simulation Accuracy

Before conclusions obtained from Monte Carlo simulation can be applied to PET, the results from Monte Carlo simulations must match those from PET experiments. This was done by comparing profiles of point sources and line sources in water cylinders acquired for energy ranges of 250 - 850 keV and 380 - 850 keV. The Monte Carlo simulation assumptions of negligible positron range, perfect γ-ray collinearity and 25 % detector energy resolution, as well as the use of a limiting, axial, stratification angle are also directly tested.

Comparison with Experimental Data

The accuracy of Monte Carlo simulation was tested by comparison of profiles obtained through Monte Carlo simulation with those obtained from PET experiments. Figure 11(a) shows a profile of a line source of ^{18}F, 5 mm in diameter, which was located in the center of a 20 cm diameter water filled cylinder. The cylindrical phantom was positioned at the center of the tomograph's field of view so that projection angle symmetry existed. This permitted the summation of profiles over all 192 projection angles in order to reduce Poisson count rate noise. The experiment and simulation were performed with the tungsten septa in place and using 2D acquisition (see fig 6 on page 22) from 250 - 850 keV where summation over all 31 axial slices was employed to improve statistics. This is permissible considering the axial symmetry of a rod source

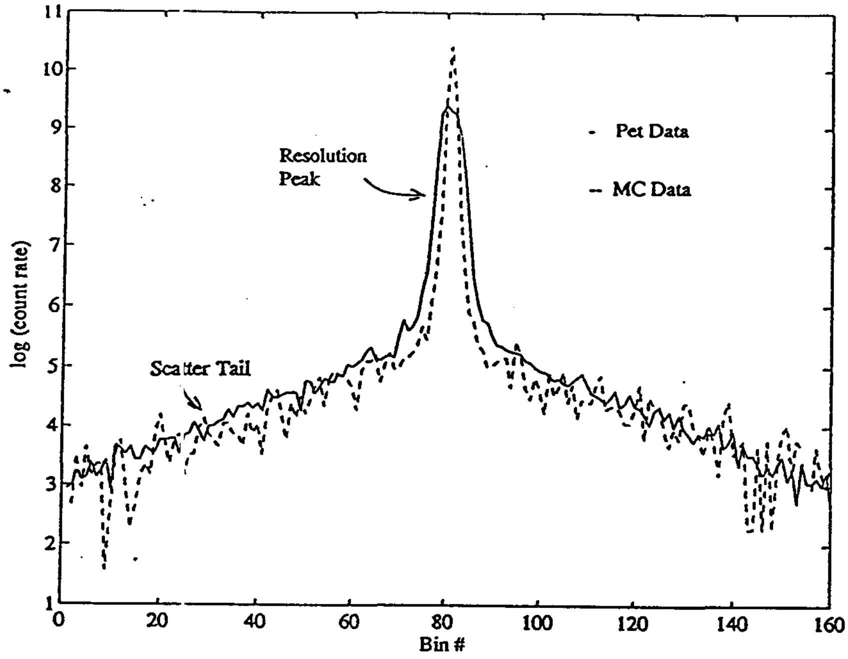

Figure 11(a): PET and MC profiles of a 5 mm diameter line source of ^{18}F centered in a 20 cm diameter water-filled cylinder. 2D acquisition from 250 - 850 keV using septa with summation over all 192 projection angles and all 31 axial slices.

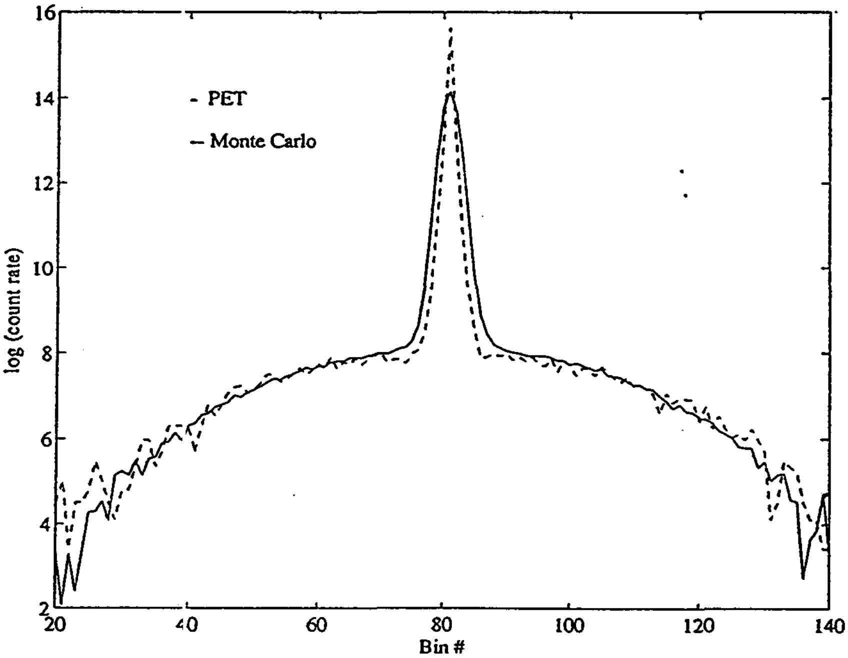

Figure 11(b): PET and MC profiles of a point source of ^{18}F centered in a 20 cm diameter water-filled cylinder. Source plane shown with summation over all 192 projection angles. Acquisition from 380 - 850 keV without septa.

centered in a cylinder of water.

Two predominant regions appear in the semi-log plot: the resolution peak and the scatter tails. The resolution peak results from unscattered photon coincidences while the scatter tails occur because of coincidences involving scattered photons. The experimental (PET) resolution peak appears somewhat broader than the Monte Carlo (MC) resolution peak predominantly because of the summation over all angles and planes which was employed. Although precise positioning of activity is possible for MC simulation, slight off-center mis-positioning of the ^{18}F rod in the tomograph causes a precession of the projected position of the rod about the central bin (Bin #81) for different projection angles, creating a broadened peak after summation. The scatter tails show reasonable agreement within the statistical uncertainty observed. The two curves were normalized to have the same total number of counts so that the agreement of the amplitude of the scatter tails indicates a comparable scatter fraction being measured in each case.

A similar profile is plotted in figure 11(b). However, in this case, a point source was centered in the 20 cm diameter water filled cylinder and the acquisition was made without septa and using an acquisition window of 380 - 850 keV. Axial summation could not be employed to enhance count statistics since the point source only has a resolution peak in the plane containing the source. Resolution peak broadening was again observed, however the scatter tails once again showed reasonable agreement. The projection was only displayed from bin 20 to bin 140 rather than using the full range from 1 - 160 because of the presence of negative values in the experimental data set in the regions of low count rate at the extreme edges of the projection. The negative values occurred because of an over-correction for random count rate in the low count rate regions. The random correction was overburdened by the high activity point source needed, since axial summation to improve count rate statistics could no longer be employed.

The similarity of the PET and Monte Carlo derived scatter tails illustrated in figures 11(a) and 11(b) are sufficient for this work since the Monte Carlo simulation was primarily used for measurement of scatter profiles. The two figures examine scatter profiles both with and without septa and using two different acquisition energy ranges. The only tests possible are those involving centered sources, which have symmetry to permit angular summation of projections, since the simulation is too slow to obtain sufficient count statistics to measure projections at specific angles.

Testing Assumptions

The assumption of negligible positron range and perfect γ-ray collinearity was tested by performing two separate simulations involving a line source in air centered in the tomograph. The first simulation assumed negligible positron range and perfect γ-ray collinearity while the second simulation accounted for the positron range and non-collinearity of an ^{18}F source. The positron range was simulated by using a range distribution histogram calculated for ^{18}F in water which is available within the *Geant* program (Geant User's Guide, 1992). The positron annihilation position was displaced in a random direction by a value selected from this histogram to simulate the effects of positron range. γ-ray non-collinearity was simulated by allowing one of the annihilation photons to deviate from its initially calculated direction by an angle selected from a Gaussian distribution with a standard deviation of 0.5° (page 9).

Figure 12 shows the resolution peaks from the MC simulations under each condition where the peaks have been normalized to have equivalent counts. Very little broadening of the resolution peak due to the effects of positron range and non-collinearity is observed. This is perhaps not surprising considering the mean range for ^{18}F positrons in water is only 0.6 mm (Table 1), while the detector size is over 6 mm across. The 384 detectors in a ring are separated by just under 1° (360/384 deg) as viewed from the center of the field of view, so the 0.5° difference in the photon's initial direction is not terribly significant.

The validity of using a limiting, axial, stratification angle to increase the effective source activity is examined in figure 13. The plot shows a distribution of the axial angle of emission for photon pairs striking detectors where at least one photon experienced Compton scattering in the object. The plot was made for a rod source located in the center of a 20 cm cylindrical water-filled phantom, with septa removed, using a 250 - 850 keV acquisition window. The distribution involving Compton scattered lines of response was plotted since scattered photon coincidences have a broader distribution than unscattered coincidences whose photons cannot be re-directed back into the scanner's field of view after exiting. The plot clearly shows that the choice of a 30° stratification angle, as suggested by Michel et al (1991), is permissible. This is so because photon pairs initially travelling in a direction with an angle from the trans-axis greater than 20° (axial angle outside the 70° - 110° range) have a negligible probability of producing a

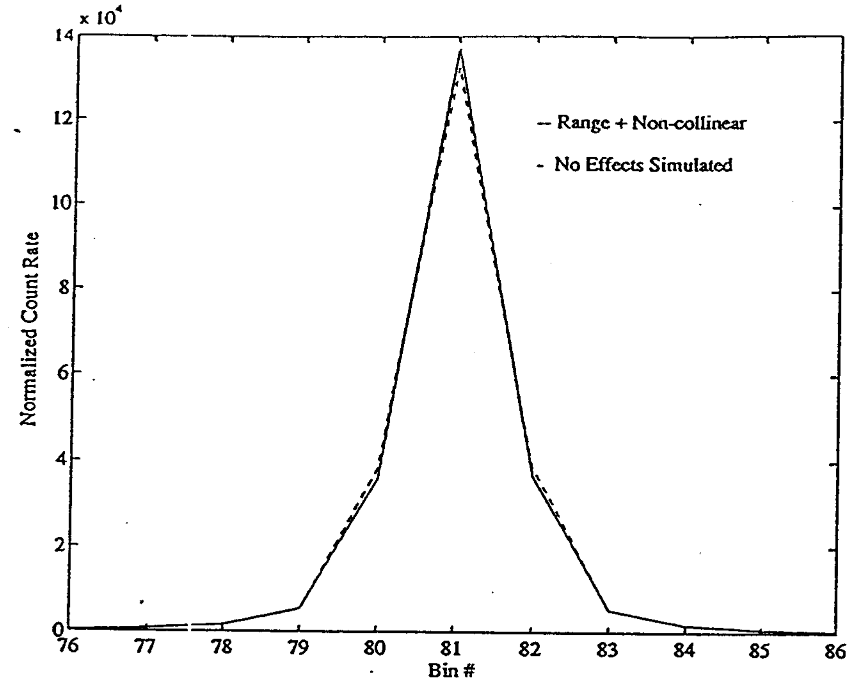

Figure 12: Resolution peak profiles for MC simulations of a line source of ^{18}F in air positioned at the center of the field of view. Simulations are with and without positron range and γ-ray non-collinearity effects included.

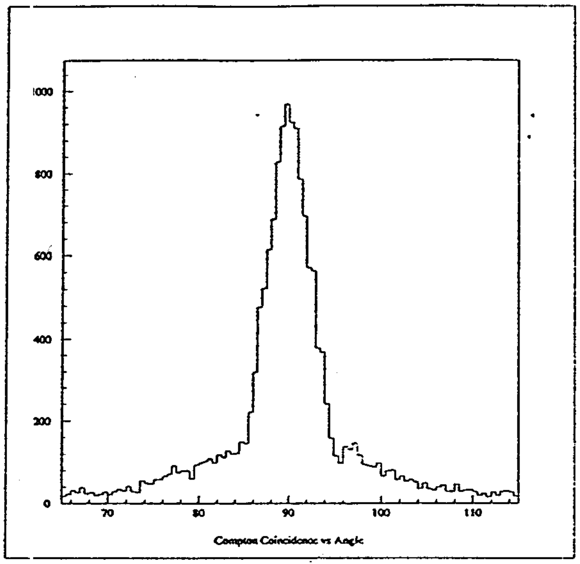

Figure 13: Distribution of initial axial angles of annihilation photon pairs which produce scatter coincidence lines of response. Plot is for a line source of positrons centered in a 20 cm water-filled cylinder.

coincidence count.

The final assumption used in Monte Carlo simulation involves the blurring of recorded detector energies by a Gaussian distribution with a FWHM equal to 25 % of the recorded energy. This was done in an effort to model the energy resolution of the BGO block detectors. The energy spectra of the BGO blocks were measured using a point source in the transmission rod holder located 28 cm radially off-center. Block detector count rates were then acquired for energy bands 40 keV wide, measured every 10 keV. No object was present in the scanner for this measurement. The spectra in figure 14 shows a peak at 435 keV with a FWHM of 110 keV, indicating an energy resolution of 110/435 = 25.3 %. A Gaussian fit with these parameters shows suitable agreement with the measured spectra indicating support for the use of a 25 % FWHM Gaussian blurring function on the recorded detector energies of Monte Carlo simulation. The observation of the peak at 435 keV rather than at 511 keV for annihilation photons reveals the poor energy calibration of the PET's detectors. This point is further explored in the next chapter.

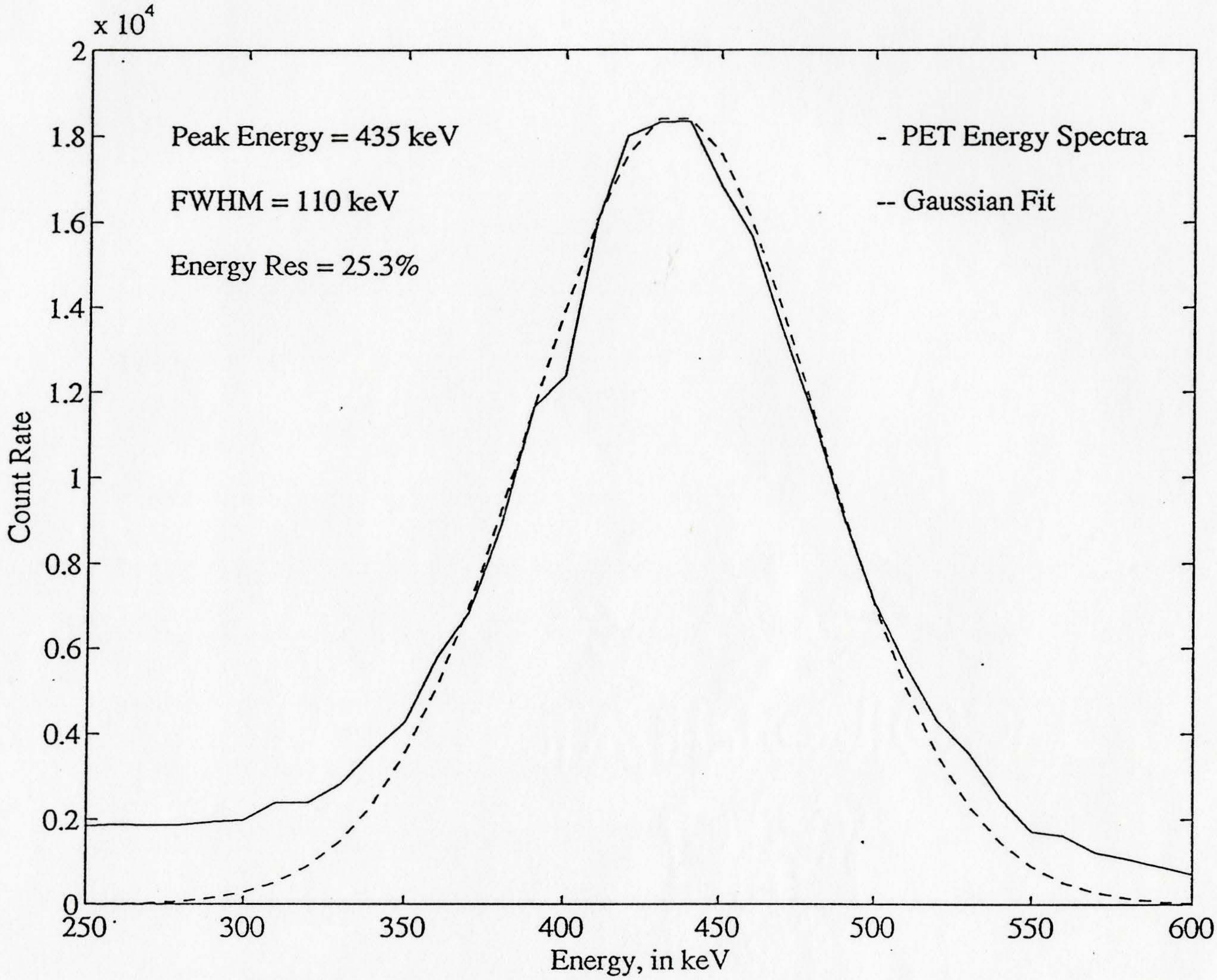

Figure 14: PET block energy spectra of a ^{18}F point source with no object in the scanner. Gaussian fit with listed parameters included.

CHAPTER V

Analytic Scatter Correction Results

To verify the accuracy of analytic scatter correction theory, scatter profiles from PET experiments are compared with those predicted by the analytic technique. Point sources of ^{18}F are located in the center, as well as 5 cm transaxially off-center of 15 cm and 20 cm diameter, water-filled cylinders to perform this comparison. Monte Carlo simulation is employed to verify the fundamental assumptions of analytic correction theory, as well as to determine the operating conditions most suited to accurate implementation of the technique. The choice of a detector energy discrimination setting which produces the most accurate scatter estimate while maximizing signal acceptance is accomplished with the assistance of Monte Carlo simulation. The physical effects most responsible for determining the shape of scatter point spread functions are examined using the analytic scatter correction theory. The inclination of 511 keV photons to exhibit forward scattering, as evident from examination of the Klein-Nishina differential cross section equation (eqn 1.9), is the main factor governing the shape of the observed scatter point spread function. Finally, an evaluation of the assumptions for some of the scatter correction proposals currently being explored is achieved using calculated profiles of the analytic correction technique.

Optimal Detector Energy Threshold Setting

Analytic scatter correction employs a single scatter approximation as its fundamental assumption. To operate the scanner under conditions most suited to this assumption, analysis of unscattered, single scattered and multiple scattered spectra, obtained through Monte Carlo simulation of a point source centered in a 20 cm diameter, water-filled cylinder, is performed. The detector energy threshold setting, E_o, which would minimize acceptance of multiple scattered events while avoiding the loss of a significant fraction of unscattered events is determined. Monte Carlo derived scatter profiles are compared with the predictions of analytic theory at threshold settings of 250 keV and 380 keV. In all cases, the energy resolution of the detectors was simulated at 25%.

Spectral Analysis

A plot of the unscattered, scattered and total spectra calculated by Monte Carlo simulation for a point source of a positron emitter centered in a 20 cm diameter, water-filled cylinder is shown in figure 15(a). The spectrum plotted is a coincidence spectrum, recording only the lower of the two energies measured by the detectors of a coincident event. The unscattered spectrum peaks at 485 keV rather than at the photopeak energy of 511 keV for this reason. This is the appropriate spectrum for evaluating coincident events since both photons must be above the detector energy threshold setting to be

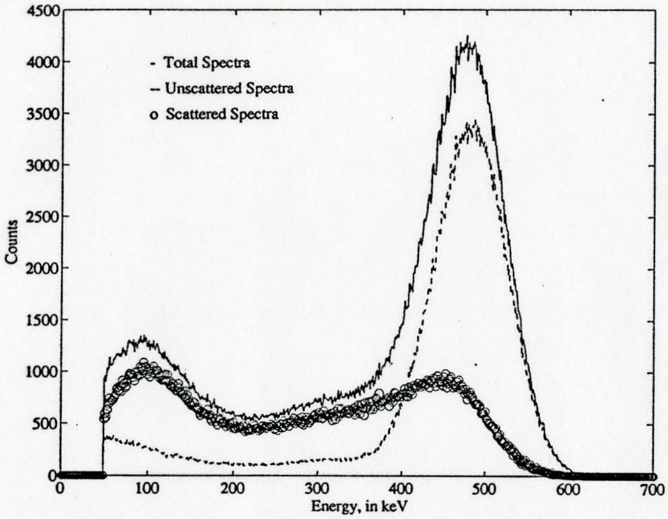

Figure 15(a): Monte Carlo derived total, scattered and unscattered spectra for a point source centered in a 20 cm diameter, water-filled cylinder.

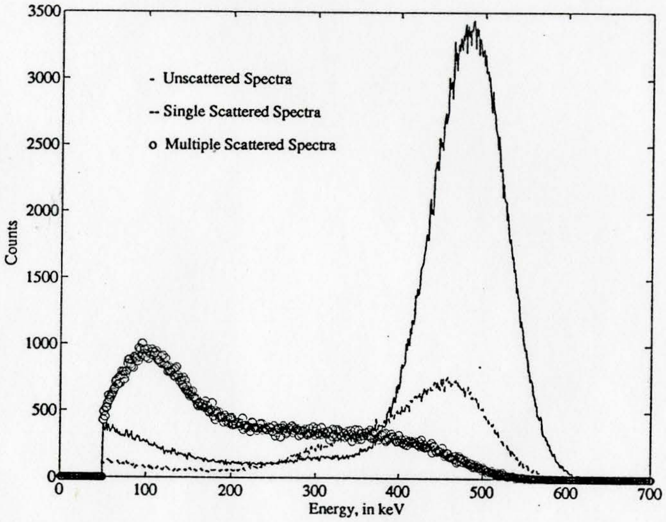

Figure 15(b): Monte Carlo derived single, multiple and unscattered spectra for a point source centered in a 20 cm diameter, water filled cylinder.

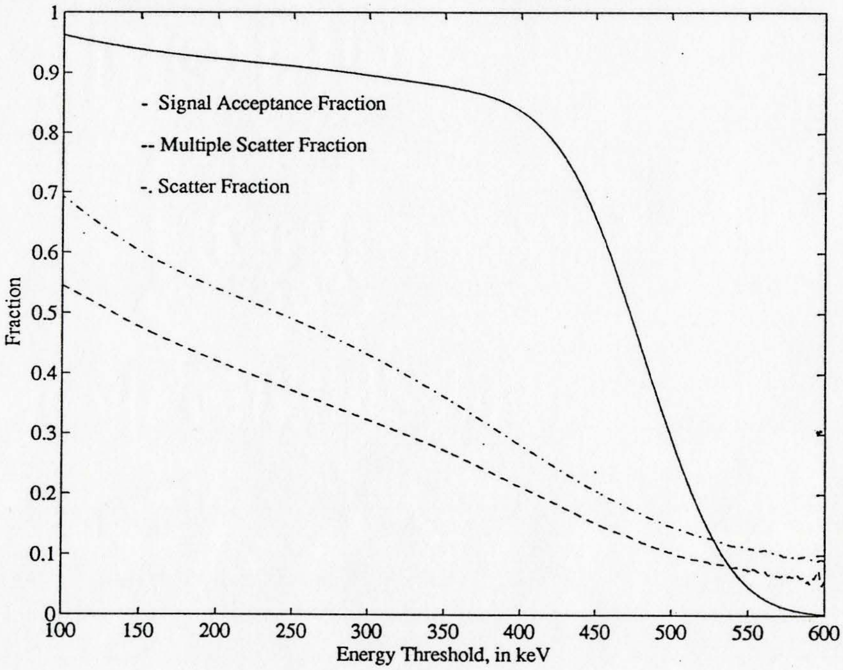

Figure 16: Monte Carlo derived signal acceptance fraction, multiple scatter fraction and scatter fraction for a point source centered in a 20 cm diameter, water-filled cylinder.

recorded. The scattered spectrum is observed to extend well into the photopeak region causing the exclusion of scattered events using only energy discrimination techniques to be rather inadequate. This is not surprising considering that scattered photons may exist at continuous energies extending up to 511 keV. In fact, the Klein-Nishina equation predicts the greatest probability for 0° scattered, 511 keV photons. It is evident that the choice of 250 keV as an energy threshold setting, currently used in practice, is considerably lower than appropriate.

Figure 15(b) separates the scattered spectrum into single scattered and multiple scattered events. The multiple scattered spectrum is observed to peak at low energies, as is expected since each occurrence of scattering diminishes the photon energy. The predominant type of scatter overlapping with the photopeak appears to be single scattered events. This is convenient since analytic scatter correction is a single scatter correction theory.

The choice of an energy threshold setting which maximizes the acceptance of unscattered events while minimizing the acceptance of multiply scattered events is desired. Figure 16 aids in this selection by plotting the signal acceptance fraction, the scatter fraction and the multiple scatter fraction calculated by integration of each spectrum over energies above each energy threshold. The scatter fraction is defined as the ratio of scatter counts over total counts, while the multiple scatter fraction is defined as the ratio of multiple scattered photon counts over all scattered photon counts. The plot shows a sharp decline in the signal acceptance fraction beginning near 380 keV. The scatter fraction declines with an increasing energy threshold setting as the scattered photons having energies below 511 keV are excluded. The multiple scatter fraction declines as well since multiple scattered photons exhibit greater energy loss than single scattered photons. At 380 keV, 86% of the signal is still accepted while the multiple scatter fraction has been reduced to 23.7%. This would be the recommended choice of energy threshold setting rather than the current setting of 250 keV where the multiple scatter fraction jumps to 37.1% with an increase to only 91% for the signal acceptance fraction.

Monte Carlo Scatter Profiles

To evaluate the accuracy of analytic scatter correction theory assumptions, Monte Carlo simulation profiles of single, multiple and total scatter events are calculated for a point source centered in a 20 cm diameter, water-filled cylinder. Figures 17(a) and 17(b) illustrate the single, multiple and total scatter profiles for detector energy threshold settings of 250 keV and 380 keV respectively. The 380 keV profiles are observed to be much narrower than the 250 keV profiles since the large angle scattered photons furthest from the peak have the lowest energy and hence the least chance of being recorded above the detector energy discrimination threshold. The magnitude of the multiple scatter profiles is greatest for the 250 keV setting as discussed in the previous section with figure 16.

Figures 18(a) and 18(b) plot the single scatter profile with the multiple scatter profile at energy discrimination settings of 250 keV and 380 keV respectively. In each

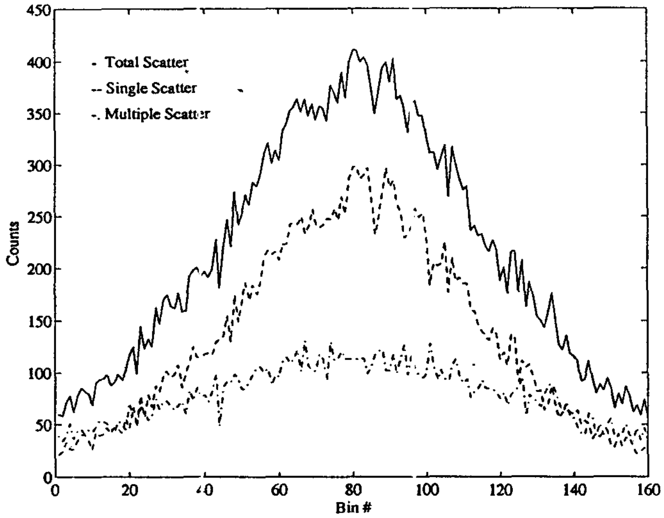

Figure 17(a): MC profiles for E_o=250 keV.

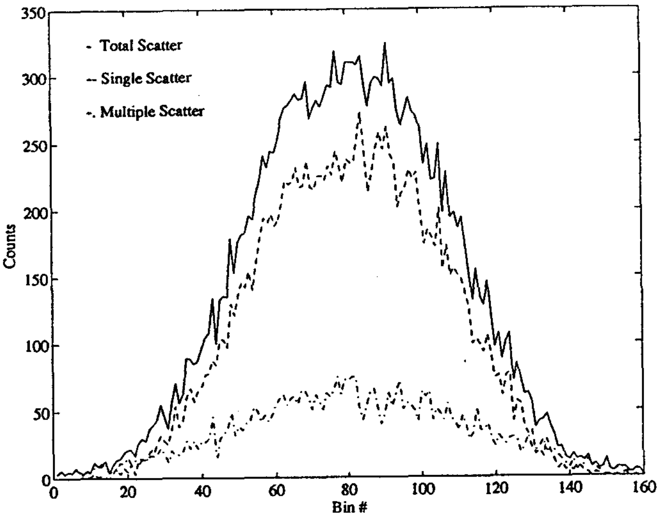

Figure 17(b): MC profiles for E_o=380 keV.

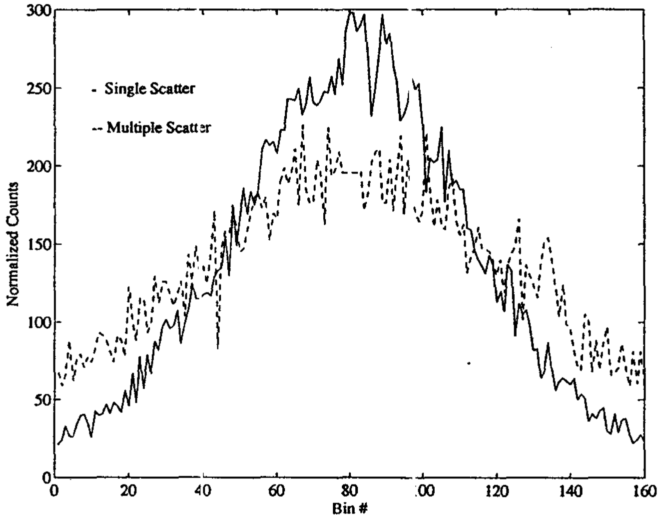

Figure 18(a): MC profiles for E_o=250 keV.

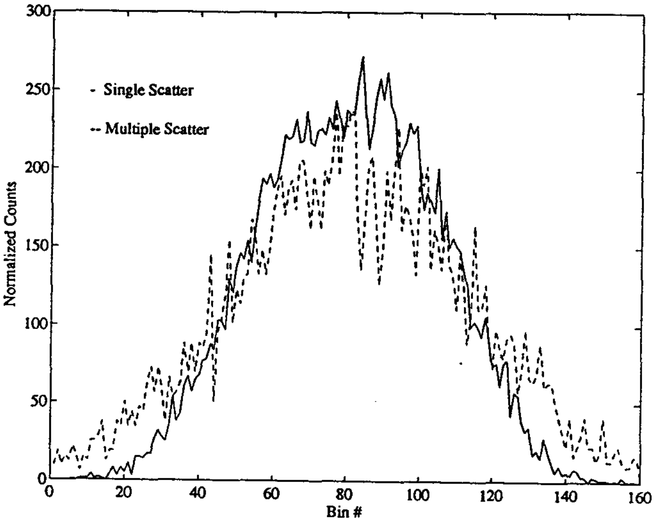

Figure 18(b): MC profiles for E_o=380 keV.

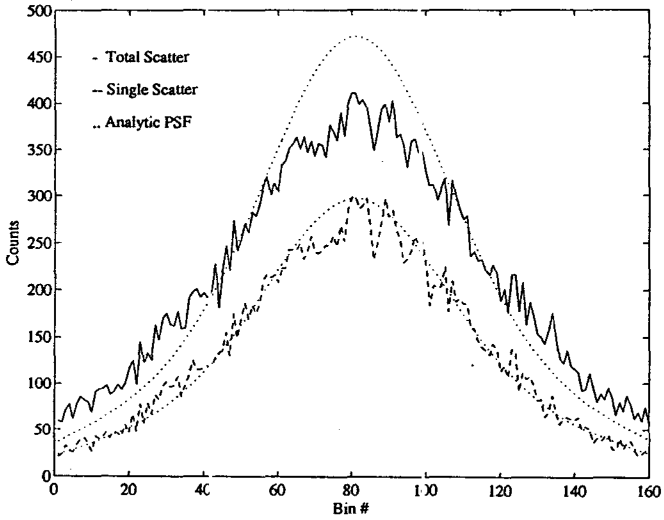

Figure 19(a): MC profiles for E_o=250 keV.

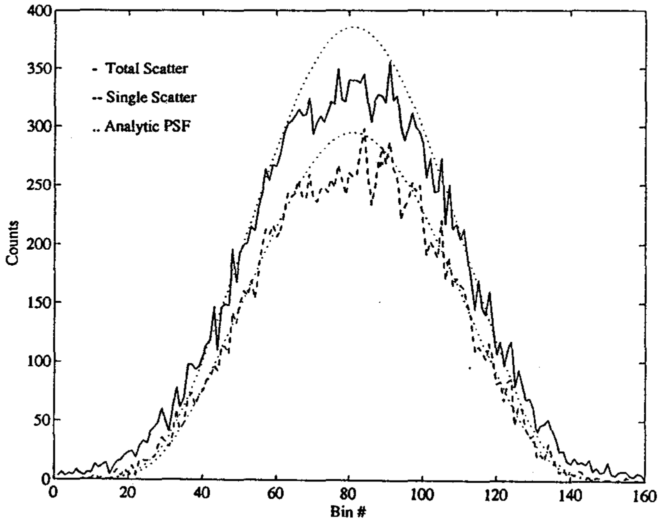

Figure 19(b): MC profiles for E_o=380 keV.

case, the multiple scatter profiles have been normalized to have the same number of counts as the single scatter profiles to allow comparison of the profile shapes. The multiple scatter profiles exhibit a shape much closer to the single scatter profiles at 380 keV than at 250 keV since the lower energy setting permits the acceptance of larger angle multiple scattered events which are displaced further from the peak. The similarity of the two profiles at 380 keV allows multiple scattered events to be accounted for within the analytic theory simply by scaling the single scatter profiles by some appropriate amount. For these Monte Carlo simulations, the appropriate scaling factor is calculated using the multiple scatter fraction curve of figure 16 according to the equation:

$$M(E_o) = \frac{1}{1 - MSF(E_o)} \qquad \textbf{(5.1)}$$

where MSF is the multiple scatter fraction and M is the scaling factor at a detector energy threshold setting of E_o.

Figures 19(a) and 19(b) plot the single and total scatter profiles for E_o = 250 keV and E_o = 380 keV respectively. Predictions of the analytic scatter correction theory for single scatter profiles as well as for total scatter profiles are also plotted for comparison. The total scatter profile estimates were made by scaling the single scatter estimate of analytic theory by the factor shown in equation 5.1, where the multiple scatter fractions have been extracted from figure 16 and are stated on page 108. The amplitude of the single scatter point spread function was determined to be 297, using equation 3.36, where the number of true counts was measured to be 1.452×10^6. In each case, the single scatter profiles appear to agree quite well with the predictions of analytic theory for both magnitude of the peak and shape of the tails, thus lending support to the single scatter theory's accuracy. Scaling to account for multiple scattering was more successful for the 380 keV acquisition [fig 19(b)] than for 250 keV [fig 19(a)] due to the closer agreement of multiple and single scatter profile shapes at higher energies, as observed in figure 18. However, an over-estimate in the amplitude and an excessively narrow PSF shape is still noticeable at 380 keV, indicating slight difficulties resulting from multiple scattering. A still higher detector energy threshold setting may be desirable.

The multiple scatter fraction scaling term represents the only term which may not be directly calculated from the single scatter theory. The results in figure 16 are only valid for the center of a 20 cm phantom. The multiple scatter fraction term is expected to increase with object size and to decrease as the point source is displaced from the center of the object. Although it is unfortunate that empirical measurements are still required to scale the single scatter function amplitude, this is certainly a far better case than having to determine the amplitude of the point spread function based entirely on empirical measurements, as has been done in the past.

Verification of Analytic Theory

The accuracy of analytic scatter correction theory is best evaluated through a comparison of experimental scatter profiles with analytically calculated scatter profiles. This is done for detector energy threshold settings of 250 keV and 380 keV. Point sources which are either centered or off-center in water-filled cylinders are used to compare the profiles. For the centered point source, scatter profiles in all 31 planes are examined to ensure the accuracy of the theory for planes not containing the source. The accuracy of the mean scatter position approximation is also tested through comparison of analytically determined plots which allow scattering either from the mean scatter position alone, or from all points along the escaping photon path within the object.

Experimental Scatter Profiles

To verify analytic scatter correction theory, scatter profiles measured with the tomograph must be compared with profiles predicted by the theory. Figure 20(a) shows a scatter profile for a point source centered in a 15 cm diameter, water-filled cylinder for the plane containing the point source (plane #7). The data was obtained with the tomograph detector energy threshold, E_o, set at 380 keV. Also plotted with the tomograph scatter profile are analytic point spread functions (PSF's) calculated for E_o = 380 keV and for E_o = 415 keV, where the amplitudes have been adjusted for multiple scattering according to equation 5.1. The multiple scatter fractions (MSF's) used in this

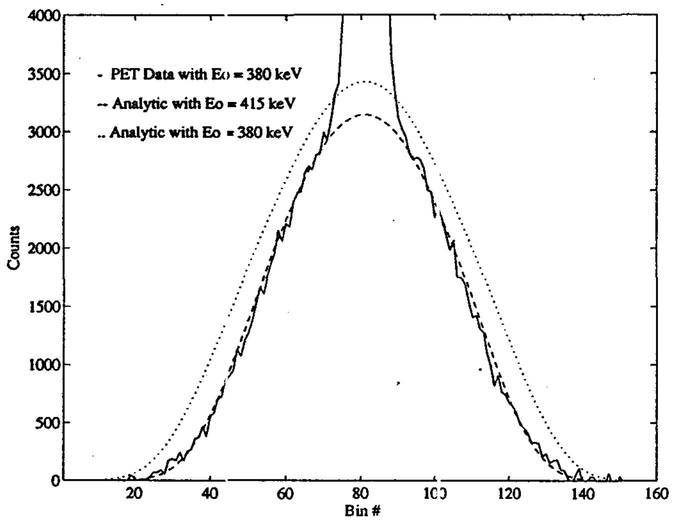

Figure 20(a): Source plane scatter profile for a point source centered in a 15 cm diameter, water-filled cylinder.

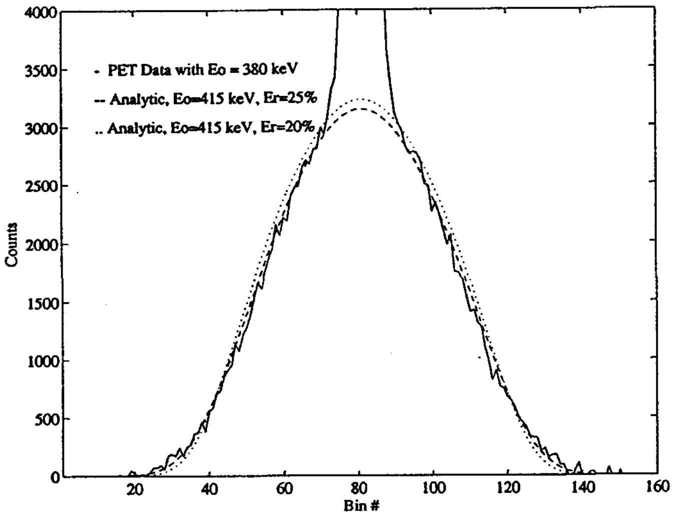

Figure 20(b): Source plane scatter profile for a point source centered in a 15 cm diameter, water-filled cylinder.

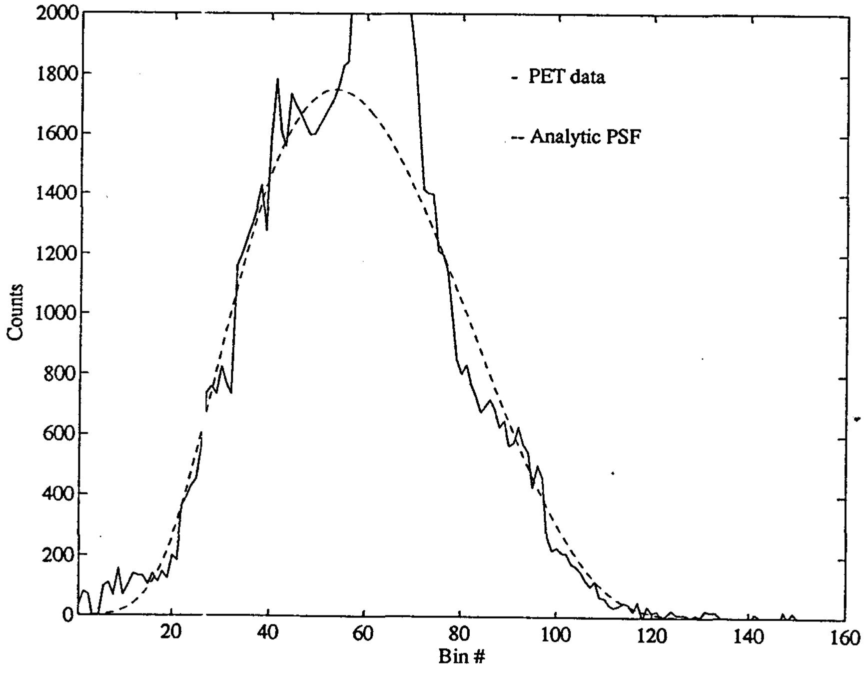

Figure 21: Source plane scatter profile for a point source of ^{18}F offset 5.6 cm from the center of a 20 cm diameter, water-filled cylinder.

calculation were extracted from the results of Monte Carlo simulation (figure 16) where the MSF's found at 380 keV and 415 keV are 0.2371 and 0.1945 respectively. The single scatter amplitude was obtained using equation 3.36, where the number of true counts, T, was measured to be 1.868×10^7 counts. The number of true counts was obtained by performing a least squares fit to the scatter tails in each of the 31 planes so that the true counts could be determined by subtracting these scatter counts from the data set.

One can see from figure 20(a) that the analytic PSF calculated for $E_o = 380$ keV is inconsistent with the scatter profile measured using the tomograph with a detector energy threshold of the same value. The analytic PSF for $E_o = 415$ keV was chosen by obtaining measurements of least square error to produce the best fit with the PET data. It is perhaps not surprising that a higher energy than 380 keV produced the best fit, considering the tomograph's poor energy calibration observed from the spectra plotted in figure 14. The 511 keV photopeak was measured at an energy of 435 keV indicating the need for the tomograph to be re-calibrated to higher energies.

The choice of energy resolution producing the most accurate agreement with experimental data was explored in figure 20(b). The analytic PSF's for $E_o = 415$ keV were plotted with energy resolutions, E_r, of 20% and 25%. The PSF with $E_r = 25\%$ showed the best agreement for amplitude and shape with the measured profile. This result is in agreement with the 25.3% detector energy resolution obtained from direct energy spectra measurements in figure 14.

The analytic scatter estimation theory was tested for off-center sources using a point source of ^{18}F offset 5.6 cm from the center of a 20 cm diameter water-filled cylinder. The acquisition was performed using a detector energy threshold of 380 keV, where the profile in the direction perpendicular to the source offset direction was plotted in figure 21. An analytic estimate, using the method described in Chapter III on page 87, was plotted with the experimental data for comparison. The analytic fit was for a source located in bin 63 with an amplitude selected to be 1750 by a least squares fit. Unfortunately, the amplitude had to be fitted rather than calculated because the extremely high count rates required to obtain sufficient data for a profile at a particular angle caused the bins near the source to be corrupted, as their values exceeded the 15 bit maximum of 32768. The profile was somewhat noisier than would have been expected from Poisson statistics (3% at 1000 counts) because of difficulties in normalizing the profile. The blank scan required for normalizing the data was acquired several months after the point source acquisition when problems associated with normalization were identified. Some of the noise observed in the experimental data can be attributed to changes in the calibration of the tomograph over this period. However, despite the normalization difficulties, reasonable agreement between the two curves is demonstrated.

Non-Source Planes

To ensure the analytic scatter correction theory accurately predicts scatter profiles in planes which do not contain the source, several profiles in off-source planes were observed for the case of a point source of ^{18}F centered in the 15 cm diameter, water-

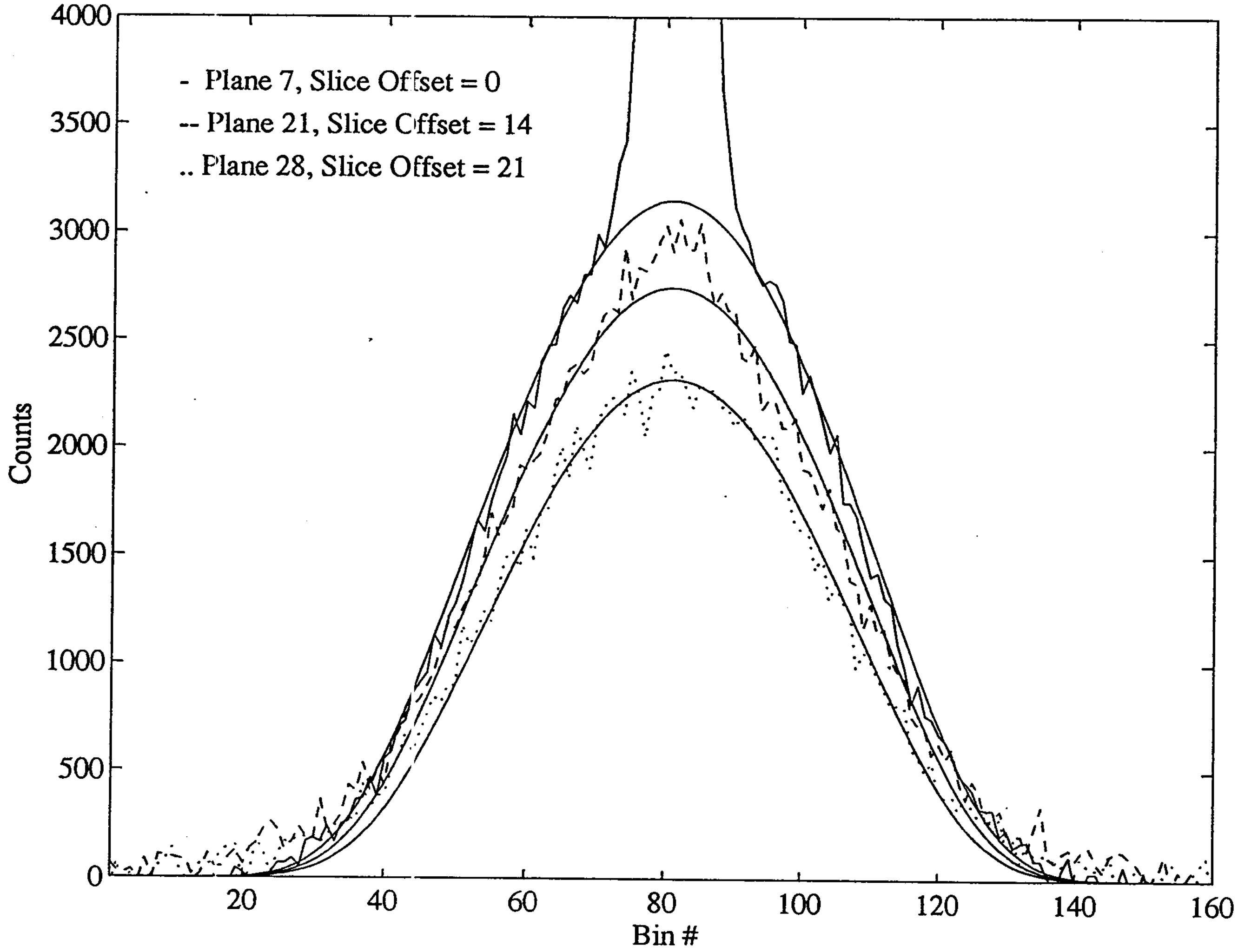

Figure 22: Non-source planes for a point source centered in a 15 cm diameter, water-filled cylinder as compared with analytic profiles.

filled cylinder. Figure 22 shows the scatter profiles measured by the tomograph for E_o = 380 keV in three different planes. The source plane (#7), with a slice offset of zero, as well as off-source planes #21 and #28, with slice offsets of 14 and 21, are plotted together with the corresponding estimates from analytic theory. Agreement between the analytic estimates and the experimental profiles is suitable for each of the three planes shown. The profiles are observed to have a lower amplitude for planes away from the source because of the scatter angle required to reach the off-source planes.

The value of the peak predicted by analytic correction theory, as well as that observed by fitting the profile with a least squares fitting routine, is tabulated in Table 2 for each of the 31 planes. The experimental profiles in each plane were normalized for plane sensitivity by measuring the number of counts in each plane which were recorded when a 20 cm diameter cylinder filled with ^{68}Ga positron emitter was placed in the center of the field of view. The table shows a reasonable agreement for most of the planes with many planes having a percentage difference between the observed and estimated amplitudes of less than 2%. Two percent is the Poisson statistical error expected for count totals of about 3000.

Several planes, particularly planes #1, #16 and #31, show greater deviations from that estimated using analytic means. This is likely because these planes are located near the edge of BGO blocks where the sensitivity is lowest and requires the greatest correction. Plane #16 is the cross plane from the inner edges of the BGO blocks in each of the two rings (see figure 2(a) on page 14). The plane sensitivity scan was also performed several months after the point source acquisition when the difficulties

TABLE 2

Non-Source Plane Scatter Amplitudes

PL #	Ring Coin	ΔSL	Theoretical Amplitude	Observed Amplitude	Percent Difference
1	1-1	6	3047	3431	12.6
2	1-2	5	3070	3307	7.7
3	2-2	4	3090	3271	5.9
4	2-3	3	3105	3230	4.0
5	3-3	2	3116	3107	-0.3
6	3-4	1	3123	3094	-0.9
7	4-4	0	3125	3096	-0.9
8	4-5	1	3123	3133	0.3
9	5-5	2	3116	3088	-0.9
10	5-6	3	3105	3058	-1.9
11	6-6	4	3090	3042	-1.6
12	6-7	5	3070	3023	-1.5
13	7-7	6	3047	3018	-1.0
14	7-8	7	3019	2861	-5.2
15	8-8	8	2987	2739	-8.3
16	8-9	9	2952	3560	20.6
17	9-9	10	2913	2850	-2.2
18	9-10	11	2871	2915	1.5
19	10-10	12	2825	2903	2.8
20	10-11	13	2777	2751	-0.9
21	11-11	14	2725	2683	-1.5
22	11-12	15	2671	2630	-1.5
23	12-12	16	2615	2559	-2.1
24	12-13	17	2556	2517	-1.5
25	13-13	18	2496	2334	-6.5
26	13-14	19	2433	2321	-4.6
27	14-14	20	2339	2260	-3.4
28	14-15	21	2303	2324	0.9
29	15-15	22	2236	2298	2.8
30	15-16	23	2168	2401	10.7
31	16-16	24	2098	2583	23.1

associated with normalization became apparent. Variation in the measurements of observed and expected amplitudes for these planes are therefore likely a reflection of changes in the plane sensitivity over this time, for those planes which rely more heavily on an accurate re-scaling for decreased sensitivity.

Non-Uniform Attenuation Objects

To test the performance of the mean scatter approximation, an analytic calculation was performed for a point source centered in a 20 cm diameter, water-filled cylinder which had a 5 cm diameter, cylindrical air pocket positioned 5 cm from the center of the cylinder. The air pocket was positioned at the coordinates x = -2.5 cm, y = +4.33 cm as viewed in figure 23(a).

The scatter profile occurring as a result of the scattering of photon 2 from the mean scatter position is plotted in figure 23(b). The only analytic correction term effected by this non-uniform attenuation situation, relative to the case of a uniform water-filled cylinder, was the escaping photon attenuation correction term. This is a sufficient test since the term expected to be most affected by the approximation of a mean scatter position is the escape path length attenuation correction term (see page 80). The effect of this modification is noticed near bin 50 when photon 2 has scattered through an angle large enough to allow its passage through the air pocket. The reduced attenuation along this escape path causes a "kink" in the profile as the probability of a scattered photon escaping attenuation increases. The right side of the profile exhibits no such "kink" since

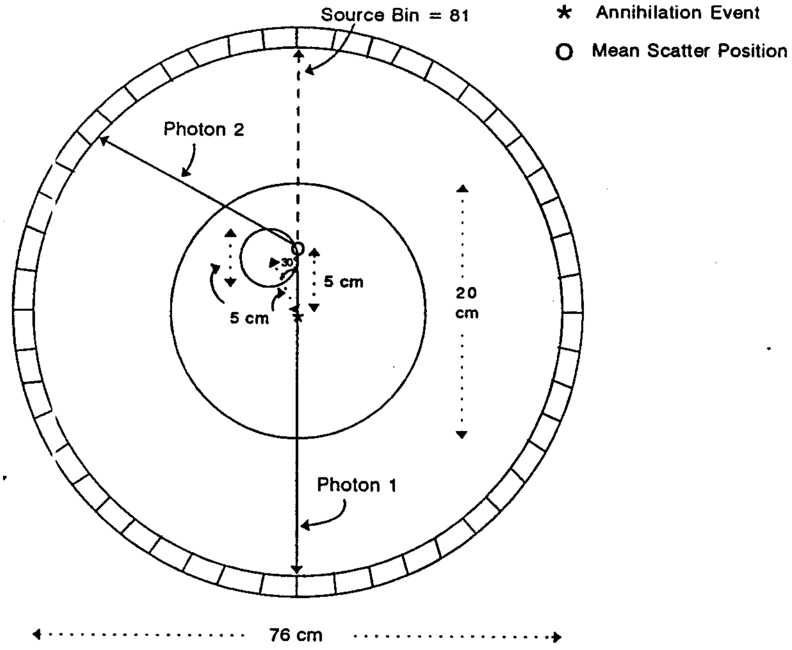

Figure 23(a): Non-uniform attenuation object having a 5 cm diameter, air-filled cylinder located within a 20 cm diameter, water-filled cylinder at the position shown.

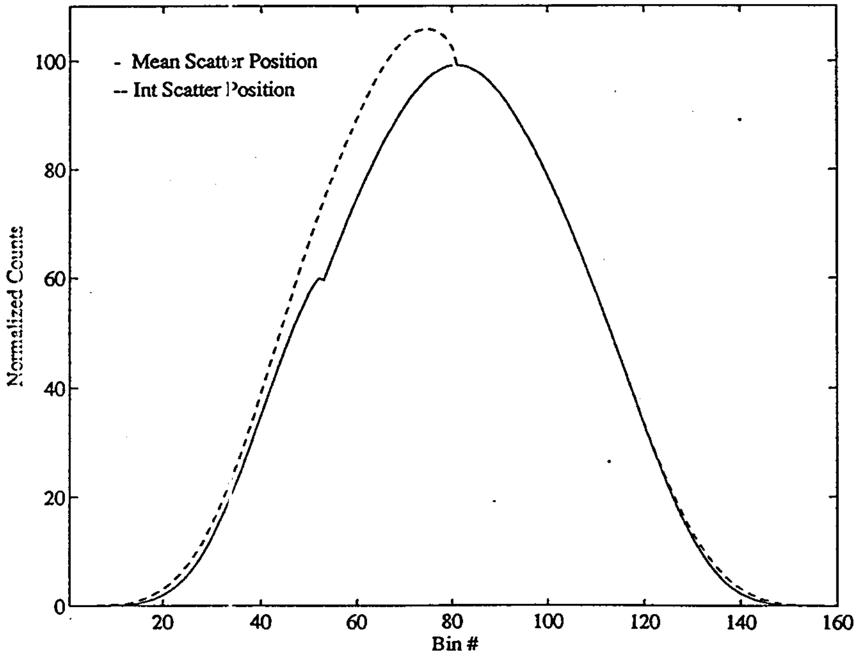

Figure 23(b): Analytically calculated scatter profile for scattering of photon 2 in the geometry diagrammed in figure 23(a).

the cylinder is uniform for photons scattered in that direction.

To test the validity of the mean scatter position assumption, the scatter profile was also calculated at 100 scatter positions spaced 1 mm apart and extending from the center of the large cylinder to its top edge as drawn in figure 23(a). The integrated scatter profile was obtained by averaging the profiles calculated at each of the 100 scatter positions. The right side of the profile in figure 23(b) shows a very good agreement between the integrated and mean scatter position calculations, giving support to the mean scatter position approximation under uniform attenuation conditions. However, the left side of the profile, which is affected by the air pocket, shows a considerable difference between the two curves. The integrated scatter position profile is much broader than the mean scatter position profile owing to the inability of any photons scattering from the mean scatter position to pass through the low attenuation air pocket for small scattering angles. The mean scatter position appears to be inappropriate for some non-uniform attenuation conditions.

Predominant Factors Responsible for PSF Determination

The factors most responsible for determining the shape of single scatter point spread functions are explored through plots of analytic profiles for centered and off-center point sources in 20 cm diameter, water-filled cylinders. To discover the dominant corrections, the analytic profiles are plotted with and without the corrections for energy discrimination, differences in escaping photon attenuation and variation of detector to mean scatter position distance. The effects of detector energy threshold setting, E_o, and detector energy resolution, E_r, are also explored through plots at a variety of values for the centered point source.

Detector Effects

The effects of varying the detector energy threshold setting, E_o, are displayed in figure 24(a) for a centered point source in a 20 cm diameter, water-filled cylinder with $E_r = 25\%$. There is very little difference in the single scatter profile observed for no energy discrimination ($E_o = 0$ keV) versus the energy discrimination setting most often used ($E_o = 250$ keV). The main benefit of employing a 250 keV discrimination setting is to remove the multiple scatter peak observed at approximately 100 keV in figure 15(b) [page 106]. As the energy discrimination setting increases from 250 keV to 400 keV, very little discrimination is observed for the 511 keV scattered photons at the peak, however the lower energy scattered photons in the tails are effectively excluded.

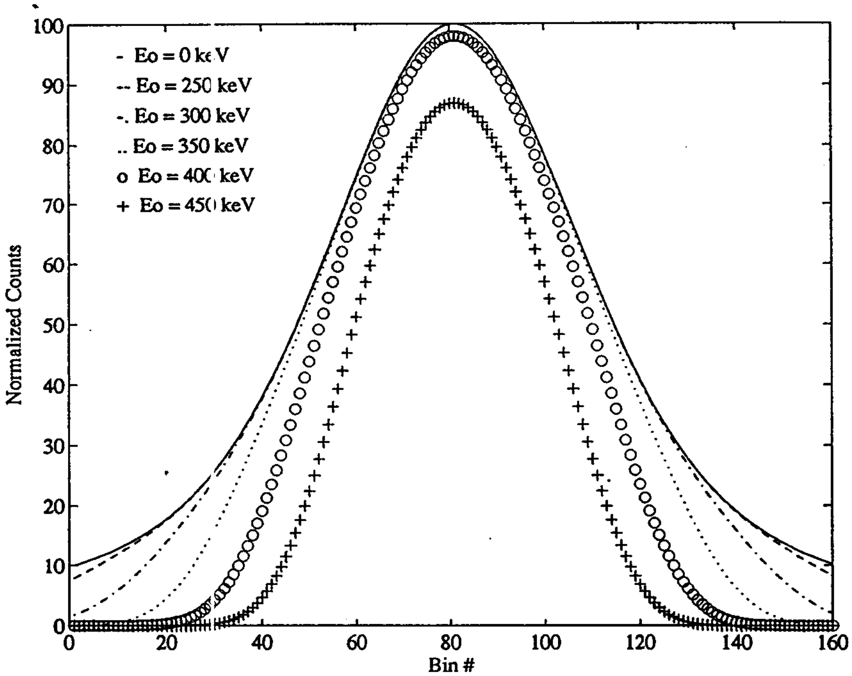

Figure 24(a): Analytic profiles for a centered point source in a 20 cm diameter, water-filled cylinder for E_r=25%.

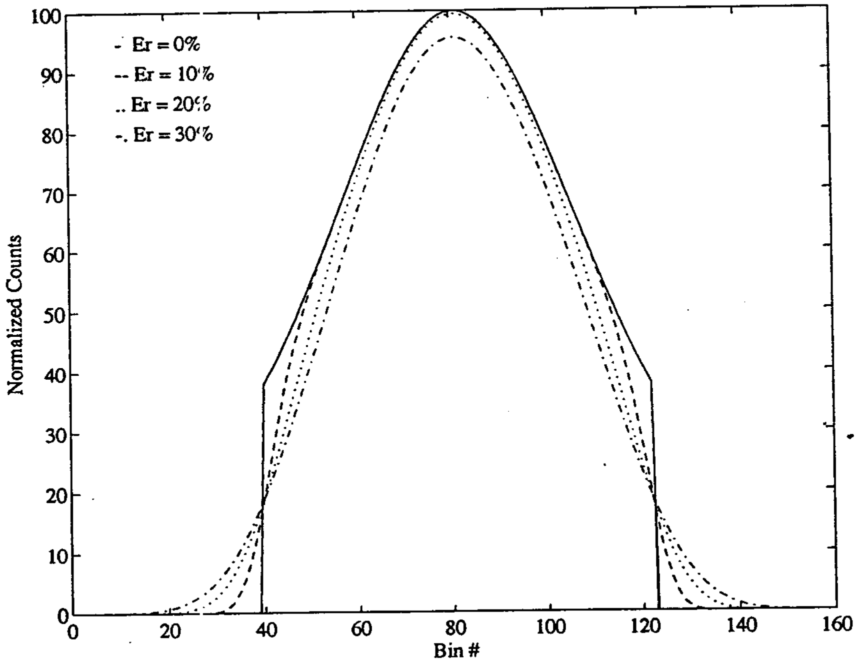

Figure 24(b): Analytic profiles for a centered point source in a 20 cm diameter, water-filled cylinder for E_o=400 keV.

The effects of varying the energy resolution setting used in the analytic calculation are revealed in figure 24(b) for the same centered point source case with a detector energy threshold setting of 400 keV. E_r = 0%, perfect energy resolution detectors, would produce a distinct cutoff in the profiles below bin 38 and above bin 124 corresponding to scattered photons whose energy is below 400 keV. If high energy resolution detectors which could efficiently detect 511 keV photons were available, the detector energy threshold could be raised closer to 511 keV producing a cutoff in the scatter profile very near the resolution peak [see figure 11(a) on page 97]. The effect of reduced energy resolution (higher E_r) is to broaden the scatter profiles.

Significance of Various Analytic Corrections

The impact of the various terms correcting the Klein-Nishina term, F(B), in the scatter profile equations (eqns 3.17 and 3.18) are explored through plots of scatter profiles for centered and off-center point sources in 20 cm diameter, water-filled cylinders. Profiles in each case are plotted with and without the correction for detector to mean scatter position distance [$R^2(0)/R^2(B)$ of equations 3.17 and 3.18], correction for differences in the escaping photon's attenuation and finally correction for energy discrimination. The detector energy threshold has been set to 380 keV in each case with the detector energy resolution set at 25%.

In figure 25(a), plotting the single scatter profiles for the centered point source reveals that the main factors responsible for determining the observed shape of scatter

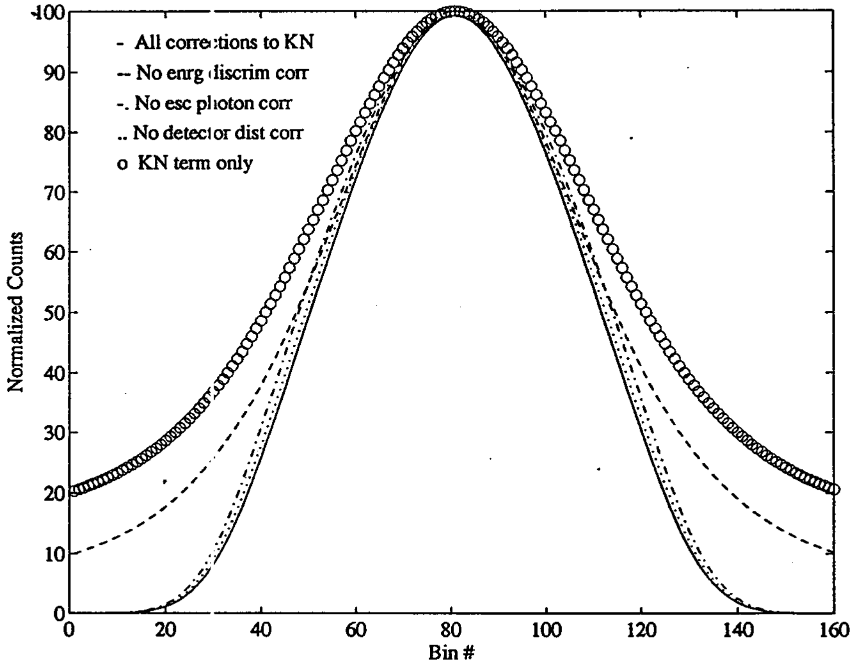

Figure 25(a): Analytic profiles for a centered point source in a 20 cm diameter, water-filled cylinder with E_o=380 keV for various analytic corrections removed.

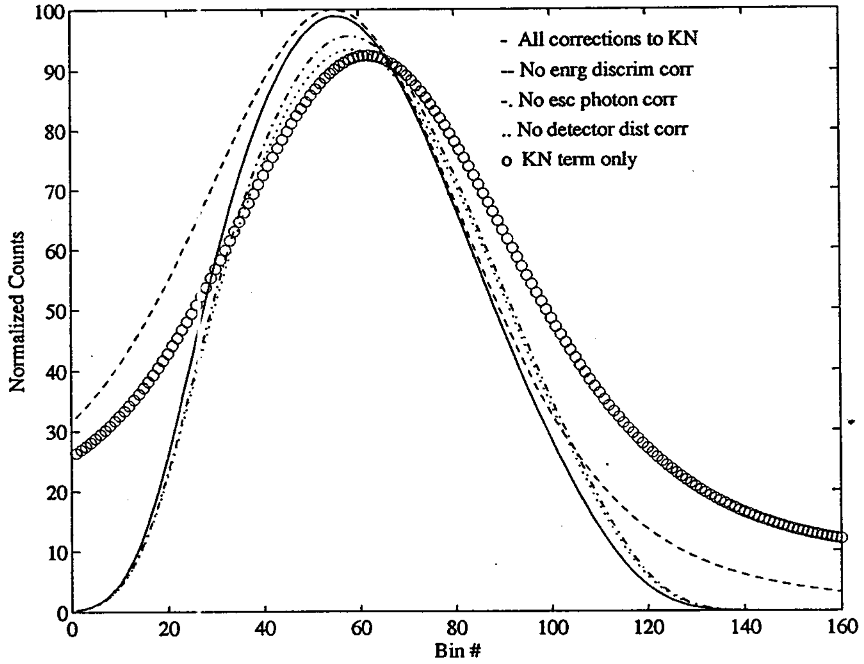

Figure 25(b): Analytic profiles for a point source offset 5 cm (source bin = 65) in a 20 cm diameter, water-filled cylinder with E_o=380 keV for various analytic corrections removed.

PSF's are the Klein-Nishina term and the energy resolution term. The escaping photon attenuation correction and the detector to mean scatter position distance correction are observed to have a more subtle impact in determining profile shape.

A similar plot for a point source offset 5 cm to the left of center of a calculated projection is shown in figure 25(b). The source is located in bin 65 for a 5 cm offset, however the peak of the scatter profile is observed to be in bin 55 exhibiting a shift towards the periphery of the object. This effect has been discussed previously by Wienhard, however the reason for the shift was left unclear (Wienhard and Lercher, 1994). The Klein-Nishina term plotted alone has its profile peak in bin 62 indicating its partial responsibility for causing a shift. Individual removal of both the escaping photon attenuation correction and the detector to mean scatter position distance correction reveal significant profile shifts to the right of the fully corrected PSF. The Klein-Nishina term, the escaping photon attenuation term and the detector to mean scatter position distance term are therefore all significant contributors to producing the observed shift in the scatter peak. However, as for the centered point source case in figure 25(a), the Klein-Nishina term and the energy discrimination term are still the dominant factors governing the overall scatter profile shape.

Evaluation of Common Scatter Correction Assumptions

The assumptions employed by many common scatter correction methods currently being explored are evaluated in this section with the aid of both Monte Carlo simulation and analytically calculated scatter profiles. The assumptions used for energy based scatter correction techniques, such as dual energy window subtraction (DEW) and the extraction of trues method (ETM), are evaluated with the aid of Monte Carlo simulation. The effectiveness of Gaussian fits to scatter profiles employed by Wienhard are also evaluated with the assistance of the analytic scatter estimation procedure.

Dual Energy Windows

The dual energy window method of scatter correction, developed by Jaszczak for SPECT (Jaszczak, 1985) and later by Grootoonk for PET (Grootoonk et al, 1993) [see page 44], requires the acquisition of a low energy window (LEW) data set, representing the scatter profile, which is then subtracted from a high energy window (HEW) data set to remove scatter from the photopeak. The fundamental assumption for this technique is the second assumption discussed on page 45 concerning the need for similar shape profiles of scattered events in the low and high energy window.

Monte Carlo simulation was employed to test this assumption using a point source centered in a 20 cm diameter, water-filled cylinder. Scatter profiles in a LEW, from 200-380 keV, as well as in a HEW, from 380-850 keV (suggested by Grootoonk), are

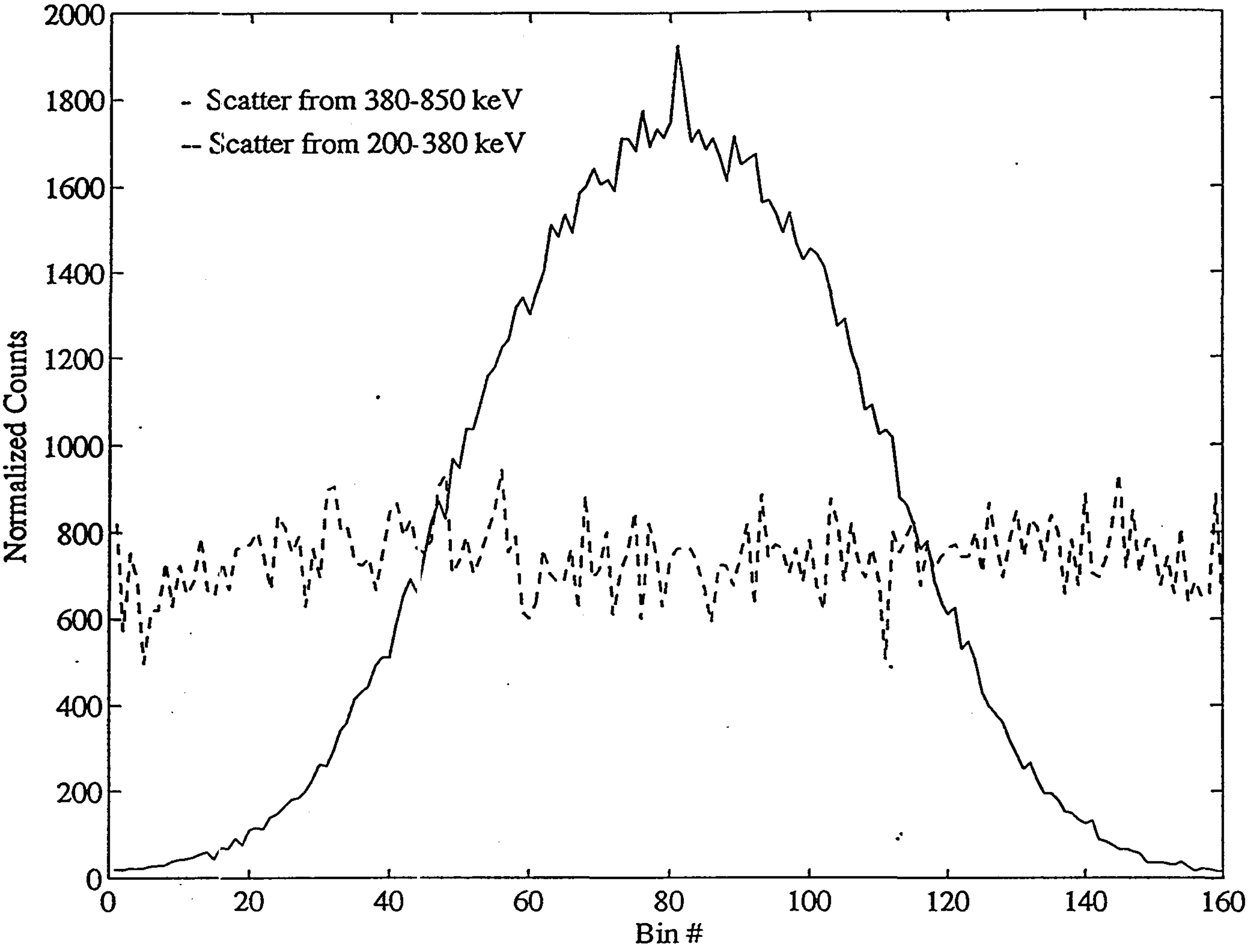

Figure 26: DEW evaluation by examining HEW and LEW scatter profiles calculated from a MC calculation for a centered point source in a 20 cm diameter, water-filled cylinder.

plotted in figure 26 where the number of counts for each profile have been normalized for comparison of shape. It is evident that the low energy window profile, assembled from broadly scattered photons, is much flatter than the high energy window profile, which contains only forward scattered photons. Attempts to scale the low energy window Compton scatter profile to represent the scatter in the high energy window are evidently dubious. This result has been previously documented by Thompson, 1993. The result is not surprising when one considers that single scattered annihilation photons at 380 keV have been scattered through an angle of 49° according to equation 1.9. All scattered photons in the LEW will thus be broadly distributed having little semblance to the forward scattered photon events recorded in the HEW.

Extraction of Trues

The extraction of trues method, developed by Bendriem (Bendriem et al, 1994), requires the acquisition of an additional high energy window from 550-850 keV to give a noisy estimate of the scatter free distribution (see page 58). This estimate may be smoothed and subtracted from a photopeak acquisition (250-850 keV) to produce an estimate of the scatter distribution. The method relies on the assumption that the high energy window is scatter free. Also, a sufficiently high count rate is required in this window to reduce the degree of noise observed in the scatter free profile estimate.

Monte Carlo simulation of a centered point source in a 20 cm diameter, water-filled cylinder again provides information to test these assumptions. The scatter fraction for the 550-850 keV window is calculated to be 11% for this case as extracted from figure 16 (page 106). This scatter fraction is considerably lower than the 49% scatter fraction observed for the 250-850 keV window, however it is still significant enough to require correction by some means. The noise in the window is expected to be rather large since the percentage of signal accepted for a detector threshold setting of 550 keV is only 5% (figure 16). Based on the ratio of signal acceptance fractions at 250 keV versus 550 keV, as extracted from figure 16, the acquisition time would have to be extended by a factor of 19 to produce an unscattered estimate with statistics similar to those typically observed for photopeak acquisition. Although smoothing applied to the high energy window data set reduces the need to produce equivalent quality statistics, a factor of 19 difference would still require a considerably extended acquisition time.

Gaussian Fits to Point Spread Functions

Attempts have been made to perform Gaussian fits (see page 56) to point sources located in various positions throughout water-filled cylinders in the hope of using these fits to perform convolution subtraction (Wienhard and Lercher, 1994). The validity of this assumption was tested using analytic calculation of centered and off-center point sources in 20 cm diameter, water-filled cylinders for a detector energy threshold of 380 keV.

The profile calculated for the centered point source is plotted in figure 27(a) together with a Gaussian curve fitted with the same amplitude and FWHM (62 bins).

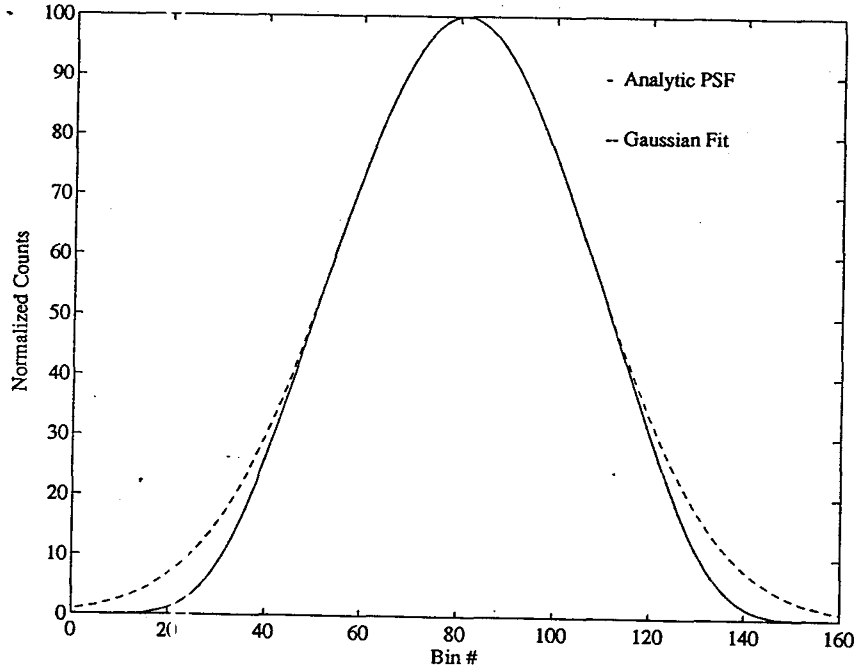

Figure 27(a): Gaussian fit to analytic scatter profile derived for a centered point source in a 20 cm diameter, water-filled cylinder with E_o=380 keV.

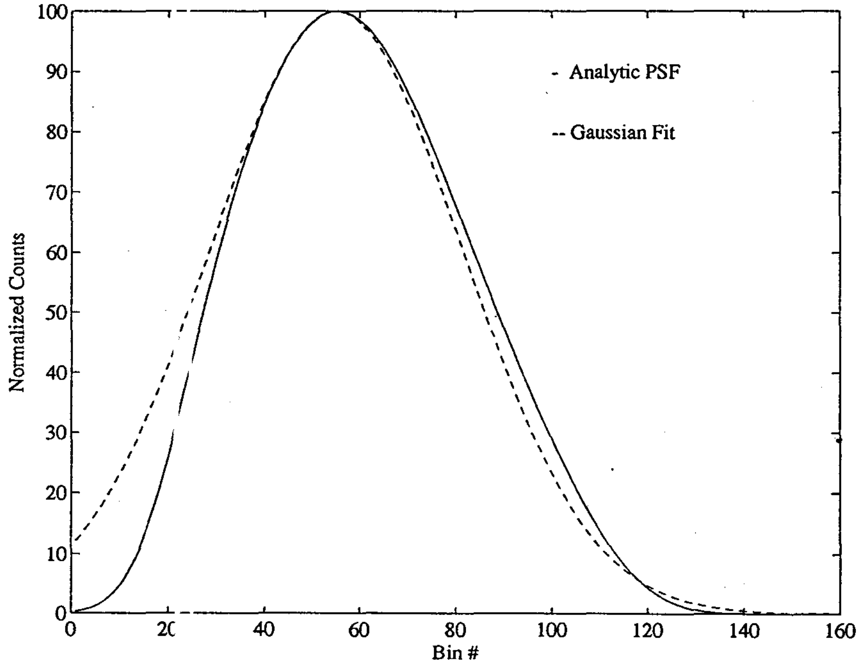

Figure 27(b): Gaussian fit to analytic scatter profile derived for a point source offset 5 cm (source bin = 65) in a 20 cm diameter, water-filled cylinder with E_o=380 keV.

The curves agree very well for much of the profile near the peak but begin to degrade in the extreme regions of the tails. Perhaps the choice of a lower detector threshold setting other than 380 keV would elevate the scatter profile in the tails producing a better fit [see figure 24(a) on page 123].

The profile for an off-center point source displaced 5 cm left of the center of the projection, into bin 65, is shown in figure 27(b). The peak of the scatter distribution is located in bin 55 demonstrating the scatter profile peak shift documented by Wienhard and discussed on page 126. Included in the plot is a Gaussian fit with a matched amplitude at the peak in bin 55, and using the same FWHM as observed (62 bins). In this case, the Gaussian fit performs less admirably, failing to fit the analytic PSF which is skewed rather than symmetric.

In reality, the main difficulty with employing Gaussian fits to PSF's is that the parameters required for the Gaussian fits are only known for point sources in uniform, water-filled cylinders. Extrapolation of the technique for use in general imaging situations involving non-uniform attenuation conditions may prove to be the greatest difficulty.

CONCLUSIONS

The validity of the 3D analytic scatter estimation technique has been assessed based on results comparing analytically calculated scatter point spread functions with profiles measured using the tomograph. The analytic theory was only tested for uniform attenuation conditions, however the mean scatter position assumption was evaluated for non-uniform attenuation conditions as well. The difficulties exhibited by the theory, as well as the steps which would be required for its ultimate application in clinical situations are also discussed.

Validity of the Analytic Method

The validity of the analytic method was evaluated through a comparison of analytically generated profiles with those measured from experiments of centered and off-center point sources in water-filled cylinders. Agreement was demonstrated for both the source planes and non-source planes in both amplitude and shape for the centered point source. The shape of the off-center point source was also shown to be in agreement with the analytically derived profiles.

The effectiveness of the mean scatter position assumption was examined through analytic calculations of a non-uniform attenuation object. The photons were allowed to scatter at several positions along the escape route for the integrated scatter position calculation, while the mean scatter position technique only permitted scattering from one location, the mean scatter position. Although the mean scatter position assumption was accurate for uniform attenuation objects, the significant differences between the two cases in the attenuation of the escaping scattered photon created difficulties for non-uniform attenuation objects. Evidently, more than one representative scatter position is needed for accurate scatter estimation in non-uniform attenuation objects.

Future Work

Having tested the analytic scatter estimation technique to ensure its validity, application of the technique to emission data to create a scatter correction algorithm is required. The most noticeable impediment to this effort stems from the considerable computational resources which would be required to visit each source line of response in the reduced data set to calculate the complete scatter profile in all 31 sinograms. The difficulties experienced by the mean scatter position approximation under non-uniform attenuation conditions exacerbates this difficulty since the computation time is extended by a factor dependent upon how many positions which photons will be permitted to scatter from as they escape the object. The need to evaluate line integrals through 2D emission and attenuation images is a considerable task, further increasing the computational time required. The only aspect of the scatter correction problem which enhances the ability to implement a practical analytic scatter correction technique is the broad profiles exhibited by scattered photons. The compression of the data set, described on page 52, may be further extended to even smaller matrices if additional computation time conservation is still required. The degree of compression required can only be evaluated after the scatter correction algorithm has been developed and the mean time for computation has been assessed.

REFERENCES

Ache HJ (1979) *Positronium and Muon Chemistry*. Washington D.C.: American Chemical Society.

Axelsson B, Msaki P, Israelsson A (1994) Subtraction of Compton-Scattered Photons in Single-Photon Emission Computerized Tomography. *J Nucl Med* **25**(4): 490-494.

Bailey DL, Meikle SR (1994) A Convolution-Subtraction Scatter Correction Method for 3D PET. *Phys Med Biol* **39**: 411-424.

Barney JS, Harrop R, Dykstra CJ (1993) Source Distribution Dependent Scatter Correction for PVI. *IEEE Trans Nucl Sci* **40**(4): 1001-1007.

Bendriem B, Trebossen R, Frouin V, Syrota A (1994) A PET Scatter Correction Using Simultaneous Acquisitions with Low and High Lower Energy Thresholds. preprint: 1-5.

Bergstrom M, Eriksson L, Bohm C, Blomqvist G, Litton J (1983) Correction for Scattered Radiation in a Ring Detector Positron Camera by Integral Transformation of the Projections. *J Compt Assist Tomogr* **7**(1): 42-50.

Bransden BH, Joachain CJ (1983) *Physics of Atoms and Molecules*. New York: John Wiley & Sons.

Brooks RA, DiChiro G (1976) Principles of Computer Assisted Tomography (CAT) in Radiographic and Radioisotopic Imaging. *Phys Med Biol* **21**(5): 689-732.

Cherry S, Meikle SR, Hoffman EJ (1993) Correction and Characterization of Scattered Events in 3D PET Using Scanners with Retractable Septa. *J Nucl Med* **34**(4): 671-678.

deKemp R (1992) *Attenuation Correction in Positron Emission Tomography using Single Photon Transmission Measurement*. McMaster University: M.Sc. Thesis.

DeVito RP, Hamill JJ, Treffert JD, Stoub EW (1989) Energy Weighted Acquisition of Scintigraphic Images Using Finite Spatial Filters. *J Nucl Med* **30**(12): 2029-2035.

Floyd CE, Jaszczak RJ, Greer KL, Coleman RE (1985) Deconvolution of Compton Scatter in SPECT. *J Nucl Med* **26**(4): 403-408.

Floyd CE, Jaszczak RJ, Harris CC, Greer KL, Coleman RE (1985) Monte Carlo evaluation of Compton Scatter Subtraction in SPECT. *Med Phys* **12**(6): 776-778.

Gagnon D, Todd-Pokropek A, Arsenault A, Dupras G (1989) Introduction to Holospectral Imaging in Nuclear Medicine for Scatter Subtraction. *IEEE Trans Med Imag* **8**(3): 245-250.

Galt J, Cullom SJ, Garcia EV (1992) SPECT Quantification: A Simplified Method of Attenuation and Scatter Correction for Cardiac Imaging. *J Nucl Med* **33**(12): 2232-2237.

Geant Team (1992) *Geant User's Guide*. Geneva, Switzerland: Cern Laboratory.

Grootoonk S, Spinks T, Kennedy A, Bloomfield P, Sashin D, Jones T (1993) The Practical Implementation and Accuracy of a Dual-Window Scatter Correction in a Neuro-PET Scanner with the Septa Retracted. *ECAT Tech User's Meeting*: 31.

Herman GT (1979) *Image Reconstruction from Projections*. New York: Springer Verlag.

Hoverath H, Kuebler WK, Ostertag HJ, Doll J, Ziegler SI, Knopp MV, Lorenz WJ (1993) Scatter Correction in the Transaxial Slices of a Whole-Body PET. *Phys Med Biol* **38**: 717-728.

Jaszczak RJ, Greer KL, Floyd CE, Harris CC, Coleman RE (1984) Improved SPECT Quantification Using Compensation for Scattered Photons. *J Nucl Med* **25**(8): 893-900.

Jaszczak RJ (1985) Scatter Compensation Techniques for SPECT. *IEEE Trans Nucl Sci* **32**(1): 786-793.

Jaszczak RJ, Coleman RE, Lim CB (1980) SPECT: Single Photon Emission Computed Tomography. *IEEE Trans Nucl Sci* **27**(3): 1137-1153.

King MA, Hademenos GJ, Glick SJ (1992) A Dual-Photopeak Window Method for Scatter Correction. *J Nucl Med* **33**(4): 605-612.

Knoll GF (1989) *Radiation Detection and Measurement*. New York: John Wiley & Sons.

Koral K, Clinthorne N, Rogers WL (1986) Improving Emission Computed Tomography Quantification by Compton Scatter Rejection through Offset Windows. *Nucl Instrum Meth Phys Res* **A242**: 610-614.

Koral K, Wang X, Rogers WL, Clinthorne N (1988) SPECT Compton-Scattering Correction by Analysis of Energy Spectra. *J Nucl Med* **29**(2): 195-202.

Lederer CM, Hollander JM, Perlman I (1968) *Table of Isotopes*. New York: John Wiley & Sons.

McKee BTA, Gurvey AT, Harvey PJ, Howse DC (1992) A Deconvolution Scatter Correction for a 3D PET System. *IEEE Trans Med Imag* **11**(4): 560-569.

Meikle S, Hutton BF, Bailey DL (1994) A Transmission-Dependent Method for Scatter Correction in SPECT. *J Nucl Med* **35**(2): 360-367.

Michel C, Bol A, Spinks T, Townsend D, Bailey D, Grootoonk S and Jones T (1991) Assessment of Response Function in Two PET Scanners with and without Interplane Septa. *IEEE Trans Med Imag* **10**(3): 240-248.

Msaki P, Axelsson B, Dahl CM, Larsson SA (1987) Generalized Scatter Correction Method in SPECT Using Point Scatter Distribution Functions. *J Nucl Med* **28**(12): 1861-1869.

Msaki P, Erlandsson K, Svensson L, Nolstedt L (1993) The Convolution Scatter Subtraction Hypothesis and its Validity in Radioisotope Imaging. *Phys Med Biol* **38**: 1359-1370.

Pretorius PH, vanRensburg AJ, vanAswegen A, Lotter MG, Serfontein DE, Herbst CP (1993) The Channel Ratio Method of Scatter Correction for Radioinuclide Image Quantitation. *J Nucl Med* **34**(2): 330-335.

Siemens Gammasonics, Inc., (1991) *Operating Instructions ECAT Scanner Hardware*. Knoxville, TN: Siemens Gammasonics, Inc.

Shao L, Karp JS (1991) Cross-Plane Scattering Correction - Point Source Deconvolution in PET. *IEEE Trans Med Imag* **10**(3): 234-239.

Smith MF, Jaszczak RJ (1994) Generalized Dual-Energy-Window Scatter Compensation in Spatially Varying Media for SPECT. *Phys Med Biol* **39**: 531-546.

Sorenson JA, Phelps ME (1980) *Physics in Nuclear Medicine*. Philadelphia: W.B. Saunders Company.

Stewart AT, Roellig LO (1967) *Positron Annihilation*. New York: Academic Press.

Thompson CJ (1993) The Problem of Scatter Correction in Positron Volume Imaging. *IEEE Trans Med Imag* **12**(1): 124-132.

Tomitani T (1987) An Edge Detection Algorithm for Attenuation Correction in Emission CT. *IEEE Trans Nucl Sci* **34**: 309-315.

Weast R, ed (1989) *CRC Handbook of Chemistry and Physics*. Florida: CRC Press Inc.

Webb S (1988) *The Physics of Medical Imaging*. Philadelphia: Hilger.

Wienhard K, Lercher MJ (1994) Scatter Correction in 3D PET. preprint: 1-28.

Yanch JC, Flower MA, Webb S (1990) Improved Quantification of Radionuclide Uptake using Deconvolution and Windowed Subtraction Techniques for Scatter Compensation in SPECT. *Med Phys* 17(6): 1011-1022.